

Sulfide Textures, Geochemistry, and Genesis of the Komatiite-Associated Eagle's Nest Ni-Cu-
(PGE) Deposit, McFaulds Lake Greenstone Belt, Superior Province, Ontario, Canada

by

Natascia Zuccarelli

A thesis submitted in partial fulfillment
of the requirements for the degree of
Master of Science (MSc) in Geology

The Faculty of Graduate Studies
Laurentian University
Sudbury, Ontario, Canada

© Natascia Zuccarelli, 2020

THESIS DEFENCE COMMITTEE/COMITÉ DE SOUTENANCE DE THÈSE
Laurentian Université/Université Laurentienne
Faculty of Graduate Studies/Faculté des études supérieures

Title of Thesis Titre de la thèse	Sulfide Textures, Geochemistry, and Genesis of the Komatiite-Associated Eagle's Nest Ni-Cu-(PGE) Deposit, McFaulds Lake Greenstone Belt, Superior Province, Ontario, Canada		
Name of Candidate Nom du candidat	Zuccarelli, Natascia		
Degree Diplôme	Master of Science		
Department/Program Département/Programme	Geology	Date of Defence Date de la soutenance	September 28, 2020

APPROVED/APPROUVÉ

Thesis Examiners/Examineurs de thèse:

Dr. Michael Leshner
(Co-Supervisor/Co-directeur(trice) de thèse)

Dr. Michel Houle
(Co-Supervisor/Co-directeur(trice) de thèse)

Dr. Pedro Jugo
(Committee member/Membre du comité)

Dr. David Good
(External Examiner/Examineur externe)

Approved for the Faculty of Graduate Studies
Approuvé pour la Faculté des études supérieures
Dr. Serge Demers
Monsieur Serge Demers
Acting Dean, Faculty of Graduate Studies
Doyen intérimaire, Faculté des études supérieures

ACCESSIBILITY CLAUSE AND PERMISSION TO USE

I, **Natascia Zuccarelli**, hereby grant to Laurentian University and/or its agents the non-exclusive license to archive and make accessible my thesis, dissertation, or project report in whole or in part in all forms of media, now or for the duration of my copyright ownership. I retain all other ownership rights to the copyright of the thesis, dissertation or project report. I also reserve the right to use in future works (such as articles or books) all or part of this thesis, dissertation, or project report. I further agree that permission for copying of this thesis in any manner, in whole or in part, for scholarly purposes may be granted by the professor or professors who supervised my thesis work or, in their absence, by the Head of the Department in which my thesis work was done. It is understood that any copying or publication or use of this thesis or parts thereof for financial gain shall not be allowed without my written permission. It is also understood that this copy is being made available in this form by the authority of the copyright owner solely for the purpose of private study and research and may not be copied or reproduced except as permitted by the copyright laws without written authority from the copyright owner.

Abstract

The Eagle's Nest nickel-copper-(platinum-group element) deposit occurs within the 2.73 billion-year-old Double Eagle intrusive complex of the Ring of Fire intrusive suite, in the McFaulds Lake greenstone belt in northern Ontario. It contains 11 million tonnes of proven and probable mineralization grading 1.68 wt.% nickel, 0.87 wt.% copper, 0.89 g/t Pt, 3.1 g/t Pd, and 0.18 g/t Au, and 9 million tonnes of inferred mineralization grading 1.0 wt.% nickel, 1.14 wt.% copper, 1.16 g/t Pt, and 3.49 g/t Pd. Mineralization occurs along the northern margin of a subvertical blade-shaped dike ~500 m wide (N-S) x ~85 m thick (E-W) x >1500 m deep composed of harzburgite, lherzolite, and wehrlite. It is interpreted to have been emplaced as a subhorizontal blade-shaped intrusive body into tonalitic rocks below the Double Eagle intrusion and rotated into its present subvertical orientation. Four sulfide textural facies have been defined spatially and geochemically through detailed core logging, petrography, and whole-rock and mineral geochemical analyses: 1) disseminated (fine-grained olivine and pyroxene with <15 wt % uniformly distributed interstitial sulfide), 2) net (fine-grained olivine and minor pyroxene with 15-35 wt% semi-continuously to continuously distributed interstitial sulfide), 3) semi-massive (50-80 wt% sulfide with 20-40% anteliths and gabbroic xenoliths), and 4) massive (>80 wt% sulfide with <20% xenoliths). There are relatively few areas containing 35-50 wt% sulfide mineralization. Five subfacies of net texture have been identified: 1) bimodal olivine bearing leopard-net texture (most common), 2) fine-grained patchy-net texture with irregular patches of sulfide (uncommon), 3) orthopyroxene-bearing pinto-net texture (coarse altered orthopyroxene similar to white spots on pinto-coloured horse), 4) inclusion-net texture, each characterized by different peridotite inclusion populations, and 5) localized zones of 'disrupted-net texture' containing 3-5 cm thick zones of amoeboid cross-cutting barren pyroxenite. All textural facies are characterized by a typical magmatic sulfide assemblage of pyrrhotite – pentlandite – chalcopyrite with minor platinum-group minerals.

Massive sulfides are localized in two embayments along the basal contact that are separated by a topographical high, grading upwards to rare semi-massive, laterally more continuous net texture, and disseminated sulfides, with gradational contacts between textures except with massive sulfide. The similar mean ore tenors of the different sulfide textural facies, Ni₁₀₀ ~7.5 and Cu₁₀₀ ~4.8, suggest that the majority of the mineralization formed from similar magma compositions at similar magma:sulfide ratios, but the presence of different inclusion populations (peridotite, gabbro, chromitite) and the presence of disrupted-net texture indicates that the olivine, inclusions, and sulfide melts accumulated from multiple pulses in a dynamic system. The smaller, blade-shaped, sulfide-rich, chromite-poor Eagle's Nest body does not appear to be the feeder to the overlying larger, oblate, sulfide-poor, chromite-rich Double Eagle body. This highlights the need to understand the fluid dynamics of entire plumbing systems when exploring for these deposit types and the significance of smaller, more dynamic magmatic conduits as environments favourable for nickel-copper-(platinum-group element) mineralization and of larger, less dynamic chonoliths/sills, as environments favourable to chromite mineralization.

Key Words: Ni-Cu-PGE sulfide, net texture, komatiite, blade-shaped dike, Ring of Fire, McFaulds Lake greenstone belt, magmatic ore deposits, Superior Province

Co-Authorship Statement

The thesis is written as a journal manuscript with four co-authors. The candidate did all of the research, prepared all of the samples for analysis, performed all of the petrographic analyses, interpreted all of the geochemical data, and wrote the first draft of the thesis. Drs. Michael Lesher (LU) and Michel Houlé (GSC-Québec) assisted in designing the project, aided in core logging, provided advice during the research, and edited the final version of the manuscript. Ryan Weston (Noront Resources) provided insightful discussion and valuable input during all stages of the project. Dr. Stephen Barnes (CSIRO-Perth) analyzed selected samples by microbeam scanning energy-dispersive X-ray fluorescence spectrometry. He also provided important discussion and feedback on the thesis draft.

Acknowledgements

This project would not have been possible without the scientific and personal support of Drs. Michael Lesher and Michel Houlé. Dr. Pedro Jugo is thanked for his guidance during project execution and review of the thesis, and Dr. Stephen Barnes is thanked for many insightful discussions. I am also very grateful to the entire Noront Resources exploration team: Alan Coutts and Ryan Weston for logistical support; Ryan Weston, Matt Deller, and Geoff Heggie for insights and discussions during core logging; Cory Exell, Rob Lyght, Tristan Megan, and Roydon Spence for assistance during core pulling and core layout, and the rest of the Esker Camp crew for their hospitality. Dave Crabtree and Sandra Clarke assisted with the SEM and EPMA analysis and Willard Desjardins provided guidance on sample preparation. The project was supported by the Targeted Geoscience Initiative program of the Geological Survey of Canada (GSC), a NSERC-Cliffs/Noront CRD grant (446109-12) and a NSERC-Discovery grant (203171-2012) to C.M. Lesher, and a Geological Survey of Canada Research Affiliate Program award to the author. I am also grateful to my family, specifically my mother who always encouraged me to follow my academic pursuits and passions, my loving partner Jordan who has been an amazing support, and friends from the Harquail School of Earth Sciences (HSES) at Laurentian University and the Canadian Armed Forces Reserve for their support throughout the project.

Table of Contents

Thesis Defence Committee	ii
Abstract	iii
Co-Authorship Statement.....	iv
Acknowledgements.....	iv
Table of Contents	v
List of Tables	vii
List of Figures.....	vii
List of Appendices	x
Chapter 1: Preface.....	1
1.1 Summary	1
1.2 Research Objectives.....	1
1.3 Research Methods.....	1
1.4 Structure of Thesis	2
Chapter 2: Journal Manuscript.....	3
1 Introduction.....	4
2 Geologic Setting	5
3 Research Methods.....	6
3.1 Core Logging and Sampling	6
3.2 Sample Preparation	6
3.3 Petrography	6
3.4 SEM and EMPA Analyses.....	7
3.5 Whole-Rock Geochemical Analyses	7
4 Geology of the Eagle’s Nest Dike	8
4.1 Geometry and Composition	8
4.2 Sulfide Distribution.....	9
5 Country Rocks	10
6 Host Rocks.....	10
6.1 Lithologies	10
6.2 Mineralogy.....	11
6.2.1 Olivine.....	11
6.2.2 Pyroxene	11
7 Mineralized Rocks	12
7.1 Lithologies	12
7.1.1 Disseminated Sulfides.....	12

7.1.2	Net-Textured Sulfides	13
7.1.3	Semi-Massive Sulfides.....	15
7.1.4	Massive Sulfides	16
7.1.5	Contacts between Sulfide Textures.....	17
7.2	Sulfide Mineralogy	17
8	Whole-Rock Geochemistry.....	18
8.1	Host Rocks	18
8.2	Ores	18
8.2.1	Sulfur Content	18
8.2.2	Metals versus S	19
8.2.3	Elemental Variations.....	19
8.2.4	Metal Tenors	20
8.2.5	Mantle-Normalized Metal Variations	20
8.2.6	Magma to Sulfide Ratios.....	21
8.2.7	S Isotopes	21
9	Discussion	21
9.1	Geometry of the Eagle’s Nest Dike	21
9.2	Genesis of Silicate Rocks.....	22
9.2.1	Connection to Other Deposits in Esker Intrusive Complex	22
9.2.2	Parental Magma and Contamination.....	23
9.2.3	Minerals and Alteration	23
9.2.4	Late Pyroxenite	24
9.3	Sulfide-Silicate Contacts.....	24
9.4	Sulfur Source	25
9.5	Sulfide Geochemical Variations	25
9.6	Net-Textured Sulfide Genesis	26
9.7	Evolution and Genesis of the Eagle’s Nest Deposit.....	28
9.8	Implications for Exploration, Mining, and Beneficiation	29
10	Conclusions.....	30
11	Acknowledgements.....	31
12	References.....	31
13	Figure Captions.....	39
14	Figures	47
15	Tables.....	94
16	Appendices.....	98

List of Tables

Table 1: Sulfide textures and their attributes.....	94
Table 2: Representative EMPA Data (Sulfide Mineral Chemistry).....	95
Table 3: Representative Whole-Rock XRF Data (Mineralized Rocks).....	96
Table 4: Representative Whole-Rock ICP-MS Data (Minor Elements and PGEs).....	97
Table 5: Sulfur Isotope Data.....	98

List of Figures

	Page
Figure 1. Geological map of the McFaulds Lake greenstone belt (modified from Metsaranta and Houlé 2020) showing the main mineral deposits/occurrences, including the Eagle’s Nest Ni-Cu-(PGE) deposit within the Esker intrusive complex (dashed rectangle in the middle of the figure). Dashed box indicates the location of Figure 2. MLGB = McFaulds Lake greenstone belt.	47
Figure 2. Geological map of the Esker intrusive complex showing the location of the main mineral deposits and occurrences (after Houlé et al., 2020).	48
Figure 3. A: Ore shell of the entire Eagle’s Nest deposit (3D model) with Ni (wt %) grades superimposed (Noront Resources, 2020) B: Schematic of a northwest-southeast section (NAD 83, Zone 16, UTM 547219 mE) section through the Eagle’s Nest dike showing the sulfide facies and subfacies distributions.	49
Figure 4. Histogram of sulfide contents in the Eagle’s Nest deposit based on Noront Resources assays. Sulfide content have been calculated on S wt % content assuming 39% S in 100% sulfides. See Table 1 for the detailed break-up of the various textural facies.	50
Figure 5. Scanned images of country rocks below the Esker Intrusive Complex (HEC Carson, in prep.).	51
Figure 6. Ternary IUGS classification diagram for ultramafic intrusive rocks showing non-mineralized and mineralized rocks within Eagle’s Nest dike.	52
Figure 7. Scanned images of barren ultramafic host rocks (NQ half core, 4.5 cm wide) and photomicrographs from thin sections (2.5x magnification) of the Eagle’s Nest dike.	53
Figure 8. Scanned images of disseminated sulfide (NQ half core, 4.5 cm wide) and photomicrographs from thin sections (2.5x magnification).	55
Figure 9. Disseminated sulfide facies at the Eagle’s Nest deposit (drillcore NOT-09-053W3 at 828.17 m, NQ core size).	57
Figure 10. Scanned images of leopard-net-textured sulfide (NQ half core, 4.5 cm wide) and photomicrographs from thin sections (2.5x magnification).	58

Figure 11. Leopard net-textured sulfide subfacies at Eagle’s Nest deposit with μ XRF maps (drillcore NOT-07-017 at 138.01 m, NQ core size).	59
Figure 12. Scanned images of inclusion-net-textured sulfide (NQ half core, 4.5 cm wide) and photomicrographs from thin sections (2.5x magnification).	60
Figure 13. Inclusion net-textured sulfide subfacies at the Eagle’s Nest deposit with μ XRF maps (drillcore NOT-07-028 at 208.97 m, NQ core size).	61
Figure 14. Scanned images of pinto-net-textured sulfide (NQ half core, 4.5 cm wide) and photomicrographs from thin sections (2.5x magnification).	62
Figure 15. Pinto net-textured sulfide subfacies at the Eagle’s Nest deposit with μ XRF maps (sample NOT-10-076-W1/557.1 m, NQ core size)	63
Figure 16. Scanned image of a 1.30 meter interval of disrupted-net texture and invading pyroxenite (NQ half core, 4.5 cm wide) (NOT-09-053/857.1).	64
Figure 17. Scanned images of disrupted-net-textured sulfide (NQ half core, 4.5 cm wide) and photomicrographs from thin sections (2.5x magnification).	65
Figure 18. Disrupted net-textured sulfide subfacies from the Eagle’s Nest deposit with μ XRF maps (drillcore NOT-09-053 at 857.26 m, NQ core size).	67
Figure 19. Scanned images of patchy-net-textured sulfide (NQ half core, 4.5 cm wide) and photomicrographs from thin sections (2.5x magnification).	68
Figure 20. Scanned images of semi-massive sulfide (NQ half core, 4.5 cm wide) and photomicrographs of semi-massive sulfide (2.5x magnification).	69
Figure 21. Scanned images of massive sulfide (NQ half core, 4.5 cm wide) and photomicrographs from thin sections of massive sulfide (2.5x and 1x magnification).	70
Figure 22. Massive and semi-massive sulfide facies at the Eagle’s Nest deposit with μ XRF maps (drillcore NOT-10-087A at 608 m, NQ core size).	72
Figure 23. Semi-massive sulfide facies at the Eagle’s Nest deposit with μ XRF maps (drillcore NOT-09-057 at 584.4 m, NQ core size).	73
Figure 24. Ternary diagrams showing compositions of pyrrhotite, pentlandite and chalcopyrite.	74
Figure 25. Backscattered electron microscope images of platinum-group minerals (PGM) in the Eagle’s Nest deposit.	75

Figure 26: Bivariate diagrams of selected whole rock oxides against MgO showing barren and mineralized samples from this study with sulfides subtracted, barren samples from other studies, analyzed olivines from this and other studies.	76
Figure 27. Primitive mantle-normalized abundances (Sun and McDonough, 1989) of highly-incompatible elements in barren ultramafic rocks in the Eagle's Nest dike, showing enrichment in highly incompatible lithophile elements (Cs, U, Th, LREE) relative to Nb-Ta and moderately incompatible lithophile elements (Y, Zr-Hf, MREE).	78
Figure 28. Th/Yb vs Nb/Yb plots (Pearce, 2008).	79
Figure 29. Histograms showing the distribution of whole rock sulfur content by subfacies of net-textured sulfides.	80
Figure 30. Metals versus S plots showing samples from this study (colours) and from Noront assay database (grey).	81
Figure 31. Tukey box plot diagrams showing S and major metal compositions at Eagle's Nest.	84
Figure 32. Tukey box plot diagrams showing Ca, Pt and Pd at Eagle's Nest.	85
Figure 33. Tukey box plot diagrams showing amount of Au and Ag at Eagle's Nest, in ppm.	86
Figure 34. Tukey box plot diagrams showing ore tenors (metals in 100% sulfides) at Eagle's Nest.	87
Figure 35. Bivariate diagram showing A: Ni ₁₀₀ (Ni tenor) versus Cu ₁₀₀ , B: Pt ₁₀₀ versus Cu ₁₀₀ and C: Pd ₁₀₀ versus Cu ₁₀₀	88
Figure 36. Precious and base metals normalized to primitive mantle in mineralized samples from Eagle's Nest compared to Raglan and Kambalda (Naldrett 2004, black). Normalization values from McDonough and Sun (1995).	89
Figure 37. Calculated metal abundances in sulfide melts (A) and derivative magmas (B) versus sulfide:magma ratio (R factor) for a parental Eagle's Nest magma.	90
Figure 38. $\delta^{34}\text{S}$ values of mineralized rocks in the Eagle's Nest dike (EN, this study), Black Thor intrusion (Farhangi, MSc Thesis, 2020), and footwall magnetite-silicate-sulfide iron formation (Carson et al., in prep.)	91
Figure 39: Reconstructed evolution of the Eagle's Nest dike.	92

List of Appendices

Electronic Appendix A: Electron probe microanalyses of olivine, pentlandite, chalcopyrite, and pyrrhotite)

Electronic Appendix B: Whole-rock geochemical data

Electronic Appendix C: Drill core logs (this study)

Chapter 1: Preface

1.1 Summary

The textures of the mineralization in magmatic nickel-copper-platinum group element deposits provide information that is important not only in constraining how they formed, but also how to design mining and mineral processing systems to maximize mineral liberation and metal recoveries. The wide range of well-preserved textures at the Eagle's Nest deposit in the "Ring of Fire" region of northern Ontario, and the abundance of core available, make it one of the best deposits of its type in which to study magmatic ore textures. This study shows that the sulfide textures in the Eagle's Nest deposit range from uniformly finely dispersed through fine continuous networks to massive sulfides, with few semi-massive sulfides. The different ore textures are most commonly gradational, characterized by different types of foreign rock fragments, and in some cases have been locally disrupted by later pulses of magma. These textures provide evidence for a sustained dynamic system in which sulfide melts, olivine, and sparse foreign and local rock fragments were transported to their present location, accumulated during subhorizontal flow, partially segregated under the influence of gravity, underwent variable degrees of modification during injection of later magmas, and solidified into the currently preserved intrusions that was later structurally rotated to its current geometry.

1.2 Research Objectives

The main objective of this project was to understand the processes responsible for generating the Eagle's Nest Ni-Cu-(PGE) deposit in the McFauld's Lake greenstone belt of northern Ontario. The specific goals included: 1) characterizing the textural and sulfide mineralogical variations in the deposit, 2) determining if whole-rock geochemical data can be used to distinguish between the various sulfide textures, and 3) using the textural variations to constrain the genesis of the Ni-Cu-(PGE) mineralization, including potential S sources (S isotopes) and mechanisms of emplacement and modification.

1.3 Research Methods

This study focussed on diamond drill cores because the Eagle's Nest deposit is not exposed at surface. 59 mineralized drill cores were examined and the mineralized parts of 40 representative cores through all accessible parts of the system were logged in detail in two field visits at the Noront Esker camp in February and August 2017. 226 samples including 182 mineralized samples comprising of 20-30 cm segments of half-sawn NQ core (4.5 cm diameter) and 44 unmineralized samples comprising of ~20 cm segments of whole or half-sawn core were taken for detailed macroscopic, microscopic, and geochemical study. Core samples were cut in the Harquail School of Earth Sciences rock preparation facility at Laurentian University (LU). Crushing for geochemical analysis was done at the Ontario Geoscience Laboratories (Geo Labs) in the Willet Green Miller Centre on the LU campus.

197 representative samples, including 3 tonalite country rocks, 39 barren ultramafic rocks, 20 ultramafic rocks containing disseminated sulfides, 90 net-textured sulfide ores (including all sub-varieties), 15 semi-massive ores, 19 massive sulfide ores, and 11 sulfide-host rock contacts were prepared as 24x46 mm polished thin sections, and examined in reflected and transmitted light. 11

samples were analyzed on a Bruker M4 Tornado energy-dispersive micro X-ray fluorescence 2D elemental scanner by Drs. S.J. Barnes and M. Le Vaillant at CSIRO in Perth, Western Australia.

Within 1 disseminated sulfide, 3 net-textured sulfide, and 6 massive sulfide samples, 30 sulfides (pentlandite, chalcopyrite, pyrrhotite), 5 platinum group minerals (PGM), 5 chromites, and 10 silicate phases (olivine, clinopyroxene) were analyzed by energy-dispersive X-ray emission spectrometry using the Geo Labs Zeiss EVO-50 scanning electron microscope (SEM). Within 4 peridotite/pyroxenite, 4 disseminated sulfide, 19 net-textured sulfide, 2 semi-massive sulfide, and 10 massive samples, 86 pentlandite, 88 chalcopyrite, 110 pyrrhotite, 10 pyrite, 50 olivine, and 4 clinopyroxene grains were analysed by wavelength-dispersive X-ray emission spectrometry using the Geo Labs Cameca SX-100 5-spectrometer electron probe microanalyzer (EPMA).

83 representative samples, including 16 barren peridotites and pyroxenites, 16 disseminated sulfide samples, 36 net-textured sulfide ores, 9 semi-massive sulfide ores, and 6 massive sulfide ores, were analyzed for lithophile and chalcophile elements at the Ontario Geoscience Laboratories (Geo Labs) in the Willet Green Miller Centre on the Laurentian University campus in Sudbury.

25 mineralized samples, including 5 disseminated, 10 leopard-net, 5 disrupted-net, and 5 massive sulfide, were analyzed for $^{32}\text{S}/^{34}\text{S}$ by stable isotope ratio mass spectrometry at Indiana University in Bloomington under the supervision of Dr. Edward M. Ripley.

1.4 Structure of Thesis

This thesis is written in the form of a manuscript to be submitted for publication in a peer-reviewed, internationally-circulated geoscience journal (*Economic Geology*). It includes a Preface (this chapter), the journal manuscript (Chapter 2), mineral data (Appendix A), whole rock geochemical data (Appendix B), and core logs (Appendix C).

Chapter 2: Journal Manuscript

Sulfide Textures, Geochemistry, and Genesis of the Komatiite-Associated Eagle's Nest Ni-Cu-(PGE) Deposit, McFaulds Lake Greenstone Belt, Superior Province, Ontario, Canada

N. Zuccarelli¹, C.M. Lesher¹, M.G. Houle^{2,1}, R. Weston³, and S.J. Barnes⁴

¹ Mineral Exploration Research Centre, Harquail School of Earth Sciences, Goodman School of Mines, Laurentian University, Sudbury, ON P3E 2C6 Canada

² Geological Survey of Canada, Québec, QC G1K 9A9 Canada

³ Noront Resources Ltd., Thunder Bay, ON P7B 6E6 Canada

⁴ Commonwealth Scientific and Industrial Research Organization, Perth WA 6155, Australia

Corresponding Author: nzuccarellipegoraro@laurentian.ca

Abstract

The Eagle's Nest nickel-copper-(platinum-group element) deposit occurs within the 2.73 billion-year-old Double Eagle intrusive complex of the Ring of Fire intrusive suite, in the McFaulds Lake greenstone belt in northern Ontario. It contains 11 million tonnes of proven and probable mineralization grading 1.68 wt% nickel, 0.87 wt% copper, 0.89 g/t Pt, 3.1 g/t Pd, and 0.18 g/t Au, and 9 million tonnes of inferred mineralization grading 1.0 wt% nickel, 1.14 wt% copper, 1.16 g/t Pt, and 3.49 g/t Pd. Mineralization occurs along the northern margin of a subvertical blade-shaped dike ~500 m wide (N-S) x ~85 m thick (E-W) x >1500 m deep composed of harzburgite, lherzolite, and wehrlite. It is interpreted to have been emplaced as a subhorizontal blade-shaped intrusive body into tonalitic rocks below the Double Eagle intrusion and rotated into its present subvertical orientation. Four sulfide textural facies have been defined spatially and geochemically through detailed core logging, petrography, and whole-rock and mineral geochemical analyses: 1) disseminated (fine-grained olivine and pyroxene with <15 wt% uniformly distributed interstitial sulfide), 2) net (fine-grained olivine and minor pyroxene with 15-35 wt% semi-continuously to continuously distributed interstitial sulfide), 3) semi-massive (50-80 wt% sulfide with 20-40% anorthites and gabbroic xenoliths), and 4) massive (>80 wt% sulfide with <20% xenoliths). There are relatively few areas containing 35-50 wt% sulfide mineralization. Five subfacies of net texture have been identified: 1) bimodal olivine bearing leopard-net texture (most common), 2) fine-grained patchy-net texture with irregular patches of sulfide (uncommon), 3) orthopyroxene-bearing pinto-net texture (coarse altered orthopyroxene similar to white spots on pinto-coloured horse), 4) inclusion-net texture, each characterized by different peridotite inclusion populations, and 5) localized zones of 'disrupted-net texture' containing 3-5 cm thick zones of amoeboid cross-cutting barren pyroxenite. All textural facies are characterized by a typical magmatic sulfide assemblage of pyrrhotite – pentlandite – chalcopyrite with minor platinum-group minerals. Massive sulfides are localized in two embayments along the basal contact that are separated by a topographical high, grading upwards to rare semi-massive, laterally more continuous net texture, and disseminated sulfides, with gradational contacts between textures except with massive sulfide. The similar mean ore tenors of the different sulfide textural facies, Ni₁₀₀ ~7.5 and Cu₁₀₀ ~4.8, suggest that the majority of the mineralization formed from similar magma compositions at similar magma:sulfide ratios, but the presence of different inclusion populations (peridotite, gabbro, chromitite) and the presence of disrupted-net texture indicates that the olivine, inclusions, and sulfide melts accumulated from multiple pulses in a dynamic system. The smaller, blade-shaped,

sulfide-rich, chromite-poor Eagle's Nest body does not appear to be the feeder to the overlying larger, oblate, sulfide-poor, chromite-rich Double Eagle body. This highlights the need to understand the fluid dynamics of entire plumbing systems when exploring for these deposit types and the significance of smaller, more dynamic magmatic conduits as environments favourable for nickel-copper-(platinum-group element) mineralization and of larger, less dynamic chonoliths/sills, as environments favourable chromite mineralization.

1 Introduction

Understanding the textures of the sulfides in magmatic Ni-Cu-(PGE) deposits is important in understanding how they formed, for determining variations in tonnages and grades for mining, and for designing beneficiation strategies. Although the textures in some deposits are relatively homogeneous (e.g., Dumont: Eckstrand, 1975; Jinchuan: Tang, 1993; Mt Keith: Barnes, 2007), others are commonly zoned (e.g., Kambalda: Ewers et al., 1972; Gresham and Loftus-Hills, 1981) or exhibit complex variations indicating multi-stage ore emplacement (e.g., Raglan: Leshner, 2007; Alexo: Houlé et al., 2011).

The textures of sulfide assemblages vary with abundance of sulfide and the nature and form of the sulfide and gangue components (**Table 1**). Disseminated mineralization typically comprises of <15 wt% sulfide dispersed between silicate phases and may be fine or coarse (blebby or globular), lightly to heavily distributed, and uniformly or non-uniformly (patchy) dispersed. Net-textured mineralization comprises of 15-60 wt% sulfide that forms a more-or-less continuous film between silicate phases (most commonly fine-grained olivine) and may also be uniformly or non-uniformly (patchy) distributed and may contain orthopyroxene or clinopyroxene oikocrysts. Semi-massive ores contain 50-80 wt% sulfide and may contain blebs of former silicate melt (emulsion texture); cumulus silicates; anteliths (fragments derived from earlier crystallization products in the system) local/exotic xenoliths; and/or veins. Massive sulfides contain >80 wt% sulfide consisting of various minerals (commonly pyrrhotite, chalcopyrite, and pentlandite) and similar gangue phases.

The origins of many of these textures have been reviewed by Barnes et al. (2017; 2018) and of these, the formation of net texture is the most complicated and the least understood. Several hypotheses have been proposed, none of which are mutually exclusive: 1) dynamic flow segregation of silicate melt, olivine, and sulfide liquid (e.g., Hudson, 1972); 2) static density segregation of silicate melt, olivine, and sulfide liquid ("Billiard-Ball Model": Naldrett, 1973; Usselman et al., 1979); 3) physical transport/deposition of olivine and sulfide liquid in more-or-less existing proportions (Tang, 1993; de Waal et al., 2004), 4) downward (gravitational) percolation of sulfide liquid into a network of cumulus olivine (e.g., Mungall, 2005; Barnes et al., 2018) during or subsequent to mechanisms 1-2, and more rarely 5) surface-tension driven infiltration of sulfide (Huminicki, 2004).

Most studies have focussed on relatively homogeneous net-textured mineralization. The Eagle's Nest deposit in the McFaulds Lake greenstone belt of northern Ontario (**Fig. 1**) contains a wide range of subfacies of net-textured mineralization. Many parts are texturally and mineralogically well preserved and some contacts between the different net textures are gradational. These textural variations are exposed in thousands of metres of diamond drill core, making Eagle's Nest an excellent place to study the origin of the various subfacies of net texture and their constraints on ore emplacement and localization. The specific goals of this project included: 1) characterizing the textural and sulfide mineralogical variations in the deposit, 2) determining if whole-rock

geochemical data can be used to distinguish between the various sulfide textures, and 3) using the textural variations to constrain the genesis of the Ni-Cu-(PGE) mineralization, including potential S sources (S isotopes) and mechanisms of emplacement and modification.

2 Geologic Setting

The 2.83-2.66 Ga McFaulds Lake greenstone belt is located at the edge of the Hudson Bay Lowlands within the northwestern Archean Superior Province (**Fig. 1**). The McFaulds Lake greenstone belt contains metasedimentary rocks, mafic-felsic metavolcanic rocks, and ultramafic, mafic, and felsic plutonic rocks (Tuchscherer et al., 2010; Mungall et al., 2010; Metsaranta et al., 2015; Metsaranta and Houlé, 2020). A 2736 to 2732 Ma mafic-ultramafic suite, the Ring of Fire Intrusive Suite (RoFIS: **Fig. 1**), has been defined by geophysical surveys, diamond drilling, geochemistry, and U-Pb single zircon geochronology (Metsaranta et al., 2015; Metsaranta and Houlé, 2020).

Houlé et al. (2019, 2020) subdivided the RoFIS into: 1) an areally more extensive Ekwan River subsuite composed of (ferro)gabbro and pyroxenite containing magmatic Fe-Ti-V-P mineralization (e.g., Butler, Thunderbird), and 2) an areally more restricted Koper Lake subsuite composed of dunite, peridotite, chromitite, pyroxenite, and gabbro containing Cr (e.g., Black Thor, Black Label, Black Creek, Big Daddy, Blackbird, Black Horse) and Ni-Cu-(PGE) (e.g., Eagle's Nest, Eagle Two, Blue Jay) mineralization (**Fig. 2**).

The 50-1500 m thick unit of ultramafic rocks hosting the Cr and Ni-Cu-(PGE) mineralization in the RoFIS appears to be contiguous over at least 16 km and has been defined as the Esker intrusive complex (Houlé et al., 2019, 2020), which includes the Black Thor intrusion, the Double Eagle intrusion, and the Eagle's Nest dike (**Fig. 2**). The apparent NE-SW orientation of the Eagle's Nest deposit projected to surface in Figure 2 reflects variations in dip along the steep plunge of the dike, while on surface the dike is oriented N-S. The contacts and layering in the Esker intrusive complex, including the stratiform Cr mineralization in the Black Thor intrusion and Double Eagle intrusion, are subvertical and the lithologies fractionate toward the SSE (e.g., Tuchscherer et al., 2010; Carson et al., 2015; Houlé et al., 2020; Carson, Ph.D. in prep.), so the Esker intrusive complex has previously been interpreted to young to the SSE and to have been structurally rotated toward that direction from an originally subhorizontal orientation.

The Black Thor intrusion is underlain by a trough-shaped feeder that extends up to ~1 km to the north and hosts the Blue Jay (formerly AT-12) and Blue Jay Extension (formerly AT-12 Extension) Ni-Cu-(PGE) occurrences (Farhangi et al., 2013; Farhangi, 2020). It contains a Late Websterite Phase that invaded the lower units of the Black Thor intrusion, including the Black Label Chromite Horizon (Spath et al., 2015; Spath, 2017). The Double Eagle intrusion is underlain by the Eagle's Nest dike, which hosts the Eagle's Nest Ni-Cu-(PGE) deposit. It has not been physically linked to the Double Eagle intrusion, and there is a significant structural break between Eagle's Nest and the Double Eagle intrusion.

All of the rocks in the Esker intrusive complex, including the Eagle's Nest area, have been metamorphosed to lower to middle greenschist facies (Metsaranta and Houlé, 2020). Relict igneous chromite is often preserved and relict igneous olivine and pyroxene are locally preserved, but all sulfides have re-equilibrated to low-temperature assemblages (see review by Naldrett, 2004). Because relict igneous textures are well preserved, for simplicity rocks will be referred to by their igneous names.

3 Research Methods

3.1 Core Logging and Sampling

The rocks in the McFaulds Lake greenstone belt are very poorly exposed, so all of the work in this study focussed on diamond drill cores. All 59 mineralized drill cores were examined and the mineralized parts of 40 representative cores through all accessible parts of the system were logged in detail in February 2017 and August 2017 at the Noront Resources Esker exploration camp. 182 mineralized samples comprising of 20-30 cm segments of half-sawn NQ (4.5 cm diameter) core and 44 unmineralized samples comprising of ~20 cm segments of whole core or half-sawn core were taken for detailed macroscopic, microscopic, and geochemical study.

3.2 Sample Preparation

Core samples were cut in the Harquail School of Earth Sciences rock preparation facility at Laurentian University using a water-cooled rock saw with a 12" diamond-embedded brass blade that was cleaned between samples with a standard kiln-fired clay-sand building brick. Rather than cutting half-core samples through the centre to produce quarter-core filets, the samples were cut parallel to the face of the sample to produce a ~46 mm wide x ~10 mm thick slab (which was ground flat for stereo microscope examination and scanning) and a ~13 mm thick half-round filet (which was used for polished thin sections and whole-rock geochemistry). 150-350 g samples were cleaned with tap water to remove slimes and samples for whole-rock geochemistry were rinsed with deionized water, dried in air on a clean paper towel, and placed into individual zip-lock plastic bags.

Crushing for geochemical analysis was done by staff at the Ontario Geoscience Laboratories (Geo Labs) in the Willet Green Miller Centre on the Laurentian University campus using a low-Cr steel roll crusher that was opened, brushed, and vacuumed between samples, cleaned by grinding Killarney quartzite between samples, and reopened, rebrushed, and revacuumed between samples (Method Code: MERC1). Pulverization was done in agate ball mills, cleaned with Killarney quartzite, a brush, and compressed air between samples (Method Code: SAM-AGM).

3.3 Petrography

197 representative samples, including 3 tonalite country rocks, 39 barren ultramafic rocks, 20 ultramafic rocks containing disseminated sulfides, 90 net-textured sulfide ores (including all sub-varieties), 15 semi-massive ores, 19 massive sulfide ores, and 11 sulfide-host rock contacts were prepared as 24x46 mm polished thin sections, examined in reflected and transmitted light using a Nikon Eclipse E6000 POL polarizing microscope, and photographed using a Leica DFC480 digital camera. The mineralogical and textural information in the samples was used to guide textural classification, petrogenetic interpretation, and sampling for whole-rock geochemistry.

11 samples were analyzed on a Bruker M4 Tornado energy-dispersive micro X-ray fluorescence 2D elemental scanner by Drs. S.J. Barnes and M. Le Vaillant at CSIRO in Perth, Western Australia. This instrument uses a ~40 µm diameter collimated X-ray beam generated from a Rh target tube operating at 50 kV and 500 nA without filters and an XFlash VR silicon drift detector. The sample is rastered under the beam with dwell times typically 5 to 10 ms per pixel, at a spatial resolution of 40 µm. Eleven 1-cm thick slabs of representative textures (1 massive, 1 semi-massive, 3

leopard-net textured, 2 disrupted-net-textured, 1 inclusion-net textured, 2 pinto-net textured, and 1 patchy/blebby disseminated) were mapped to determine chemical/mineralogical variations within the various textural facies and subfacies. Each map is presented as a composite red-green-blue (RGB) image showing the distributions of combinations of three elements (Cr-Fe-Ca, Ni-Cu-S, and S-Fe-Ca). Minerals containing none of the elements appear black, minerals containing one of the three elements appear in the corresponding colour, and minerals containing equal amounts of two or three of the elements appear in composite colours (e.g., 1 green + 1 blue = cyan, 1 red + 1 green = yellow, 1 red + 1 blue = magenta, 1 red + 1 green + 1 blue = white), and minerals containing unequal amounts of two or three of the elements appear in intermediate colours (e.g., 2 red + 1 green = orange). Each channel is normalized to the minimum and maximum count rate per pixel over the entire map; hence where concentrations of a particular element are low, this normalization process will exaggerate backgrounds and can produce artefacts. Diffraction artefacts can also arise at low element concentrations, arising from geometry whereby a particular crystal is aligned with a lattice plane making a Bragg angle with the input beam and the detector, although these are usually only evident in unaltered well-crystalline rocks.

3.4 SEM and EMPA Analyses

30 sulfide grains (pentlandite, chalcopyrite and pyrrhotite), 5 platinum group minerals (PGM), 5 chromite grains, and 2 silicate phases (olivine and clinopyroxene) from within 1 disseminated sulfide, 3 net-textured sulfide, and 6 massive sulfide samples were analyzed by energy-dispersive X-ray emission spectrometry using the Geo Labs Zeiss EVO-50 scanning electron microscope (SEM) equipped with an Oxford 50 mm² solid state silicon-drift detector. Analytical conditions were 15 kV accelerating potential and 15 nA beam current for all analyses.

86 pentlandite, 88 chalcopyrite, 110 pyrrhotite, 10 pyrite, 50 olivine, and 3 clinopyroxene grains in 4 peridotite/pyroxenite, 4 disseminated sulfide, 19 net-textured sulfide, 2 semi-massive sulfide, and 10 massive samples were analysed by wavelength-dispersive X-ray emission spectrometry using the Geo Labs Cameca SX-100 5-spectrometer electron probe microanalyzer (EPMA). Analytical conditions were 20 keV accelerating potential and a 35 nA beam current for major elements, and 20 keV accelerating potential and a 20 nA beam current for minor elements. Counting times ranged from 10-40 seconds on both peaks and backgrounds, depending on count rates. Natural and synthetic standards were used to monitor accuracy and precision, as reported in **Electronic Appendix A**.

3.5 Whole-Rock Geochemical Analyses

83 representative samples, including 16 barren peridotites and pyroxenites, 16 disseminated sulfide samples, 36 net-textured sulfide ores, 9 semi-massive sulfide ores, and 6 massive sulfide ores, were analyzed for lithophile and chalcophile elements at the Ontario Geoscience Laboratories (Geo Labs) in the Willet Green Miller Centre on the Laurentian University campus in Sudbury. To minimize sampling errors and nugget effects, all analyzed samples were as texturally uniform as possible and weighed between 70 and 300 g, with the majority between 100 and 250 g. All whole-rock data is available in **Electronic Appendix B**.

Major and minor elements in unmineralized and weakly mineralized samples were analyzed by wavelength-dispersive X-ray fluorescence spectrometry (Method Code XRF-M01: Keating and Burnham, 2013) using a XRF-PANalytical Axios Advanced spectrometer after fusion with a flux

containing 49.5:49.5:0.5 LiBO₂:Li₂B₄O₇:LiI. Mineralized samples with high S ± Cr ± Fe contents were analyzed by WD-XRFS using a lower than normal sample:flux ratio (Method Code XRF-MOX: Burnham 2014). Trace elements in unmineralized samples were analyzed by inductively-coupled plasma mass spectrometry (Method IMC-100: Burnham 2008) using a Perkin-Elmer Elan 9000 spectrometer following a 10-16 day closed-beaker HF-HClO₄-HCl-HNO₃ digestion (Method Code SOL-CAIO: Burnham et al., 2002).

Metals and semi-metals in mineralized samples were analyzed by flame atomic absorption spectrophotometry (Method Code AAF-101) using an AA Varian Spectra AA280FS instrument and ICP atomic emission spectrometry (Method Code IAT-100) using a Thermo iCAP6500 ICP-OES (radial view configuration) instrument following open-beaker aqua regia (Method Code: SOL-ARD) and HF-HClO₄-HCl-HNO₃ digestion (Method Code SOL-OT3), respectively. Mineralized samples were analyzed for Au, Pt, Pd, Rh, Ru, and Ir by ICP-MS using a Perkin-Elmer Elan 5000 ICP-MS following Ni sulfide fire-assay preconcentration and Te-coprecipitation (Method Code IMP-200: Richardson and Burnham, 2002).

C and S were analyzed by inductive combustion and infrared spectroscopy (Method Code IRC-100) using a Leco CS844 analyzer system. Loss-on-ignition was determined gravimetrically by heating at 100 °C under a nitrogen atmosphere and then at 1000 °C under an oxygen atmosphere until a constant weight was determined (Method Code LOI-3ST).

A total of 25 mineralized samples, including 5 disseminated, 10 leopard-net, 5 disrupted-net, and 5 massive sulfide, were analyzed for ³²S/³⁴S by stable isotope ratio mass spectrometry at Indiana University in Bloomington under the supervision of Dr. Edward M. Ripley.

4 Geology of the Eagle's Nest Dike

4.1 Geometry and Composition

The Eagle's Nest Dike is ~500 m wide (N-S) x ≤85 m thick (E-W) x >1500 m deep (**Fig. 2** and **3**) with a narrow, flattened tube-like morphology. It composed mainly of peridotite and lesser pyroxenite, grading to the SE from mineralized peridotite through unmineralized peridotite to minor zones of unmineralized pyroxenite, with fine-grained pyroxenitic margins. In some areas the tonalitic country rocks are contact metamorphosed. Allowing for the same structural rotation that has affected the Esker intrusive complex and consistent with the asymmetric lithological zoning, it is interpreted to have originally been a subhorizontal blade-shaped dike (Mungall et al., 2010; Zuccarelli et al., 2018a).

The shape of the intrusion varies with depth. From surface to 250 m depth, the intrusion is 500 m wide (thick) and the NW (basal) contact defines ~150 m wide (deep) embayment. Between 250 and 360 m depth, the basal contact protrudes to the SW, representing a ~50 m wide (high) topographic feature. Between 360 and 1500 m depth the intrusion narrows to 50 m wide (thick) and the basal contact defines a ~150 m wide (deep) embayment.

The NW (original lower) and lower lateral (NE-SW) contacts between the ultramafic intrusion and the tonalite country rocks are highly irregular and are commonly characterized by 10-50 cm-thick intervals of peridotite containing angular 30-60 cm tonalite fragments and by 10-30 cm-thick veins of peridotite and pyroxenite intruding tonalite. Lower contacts between massive sulfide and country rock tonalite are relatively sharp and locally sheared with 2-5 mm-thick zones of

chalcopyrite along the contact and 1-5 cm-thick veins of Cu-rich sulfides that extend ~30 cm into the country rocks, Lower contacts between net-textured sulfide are rich in chalcopyrite and are also sometimes sheared.

The SE (original upper) and upper-lateral (NE and SW) contacts are characterized by a 5-10 m-thick fine-grained pyroxenitic margins that have been altered to tremolite-actinolite, which occasionally contain 1-2 m angular fragments of angular tonalitic country rock, and 10-30 cm veins of pyroxenite, which intrude the adjacent tonalite. The veins are altered to fine-grained tremolite-actinolite, marked by 2-5 cm-thick fine-grained ultramafic margins and by 5-10 cm-thick margins of baked/melted tonalite marked by local anhedral/truncated plagioclase crystals and pockets of granophyre. There are no significant sulfides along the SE (original upper) contact of the dike.

4.2 Sulfide Distribution

The greatest proportion of Ni-Cu-(PGE) mineralization and Ni grade is restricted to the narrow NW contact of the intrusion, extending almost continuously from surface to ~1300 m (**Fig. 3**). In the upper parts of the deposit, the drill hole spacings are 10-30 m, making them more definitive, however, below ~450 m depth, the spacings are 50-100 m, making them less definitive (**Fig. 3A**). Nevertheless, there is generally fairly good agreement between adjacent drill holes, so the results appear to be representative.

The ore body can be subdivided into three major domains, each of which is zoned from N to S (**Figs. 3A-B**):

- 1) An upper embayment between surface and 270 m depth that contains 50-70 m of massive sulfide along the basal contact overlain by 50-100 m of net-, disrupted-net, and disseminated mineralization that grades through 30-60 m of disseminated sulfide in peridotite into 80 m of barren pyroxenite.
- 2) A paleo-topographic high between 270 and 350 m depth that is overlain by 50 m of barren peridotite and very minor disseminated sulfide
- 3) A lower embayment between 350 m and 1300 m depth that can be subdivided into five subdomains:
 - A. An upper part between 350-450 m that is a 20 m wide x 30 m long x 20-30 m thick zone of massive sulfide grading through to a 25-50 m thick zone of disseminated sulfide.
 - B. An upper-middle part between 450 and 600 m depth that is underlain by up to 30 cm of 0.05–10 m thick sulfide veins with sharp margins in tonalitic country rocks. This is overlain by 50–150 m of leopard-net texture and minor disrupted-net texture, and 100 m of barren peridotite and pyroxenite with only very sparse disseminated sulfides.
 - C. A middle part between 600 and 800 m depth that comprises 30–70 m of leopard-net, disrupted-net, and lesser pinto-net and inclusion-net textures with little to no massive sulfide and very little disseminated sulfide. The contacts between disrupted-net and leopard-net-textured zones are very irregular and gradational.
 - D. A lower-middle part between 800 and 1050 m that comprises of 20-60 m of leopard-net and 5-10 m of disrupted-net texture, underlain by 5-10 m thick sulfide veins and overlain by disseminated sulfide and 100-150 m of barren peridotite
 - E. A lower part between 1050 and 1300 m that comprises 20–30 m of leopard-net and highly altered leopard-net with minor massive sulfide veins, and 30 m of barren peridotite. One

hole at 1240 m depth intersected massive sulfide, but drilling has not progressed past this point to define its extent.

Estimates of disseminated, net, semi-massive and massive sulfide distributions are based on S assays from 340 drill hole intersections in the Noront Resources database (over 10,000 samples). The vast majority of samples plot in the disseminated (<5 wt% sulfide) and net-textured (15-35 wt% sulfide) categories (collectively 85% of mineralization) whereas semi-massive (50-80 wt% sulfide) and massive sulfide (>80 wt% sulfide) make up the rest of mineralization (**Table 1, Fig. 4**).

5 Country Rocks

The rocks surrounding the Eagle's Nest Dike include tonalite, iron formation, and gabbro (**Fig. 5**). The predominant country rock adjacent to and near the Eagle's Nest intrusion is tonalite containing ~30% quartz, ~50% plagioclase, and ~20% biotite and hornblende.

Rafts of silicate-oxide-(sulfide) facies iron formation up to 2-20 m thick locally occur within the tonalite (medium-grained greyish-white, plagioclase, quartz, and lesser biotite) northeast of Eagle's Nest (see **Fig. 2**: Metsaranta and Houlé, 2020; Houlé et al., 2020). The iron formation is comprised of interbedded layers dominated by silicates (fine-grained quartz \pm stilpnomelane \pm grunerite \pm allanite), oxide (fine-grained magnetite), and lesser chlorite (probable mafic volcanoclastic horizons: Carson et al., 2018; Carson, in prep.), with fine-grained acicular ferristilpnomelane along the contacts between the silicate and oxide layers. Rafts of 25 – 60 m thick leuco-meso-melagabbroic rocks also occur in the tonalite. The plagioclase is predominantly fine-medium grained but locally porphyritic, and is normally altered to chlorite and amphibole (Carson et al., 2018; Carson, in prep.).

6 Host Rocks

6.1 Lithologies

Ultramafic rocks host all the sulfide mineralization at Eagle's Nest deposit. They range in composition from olivine websterite to lherzolite (**Fig. 6**), and most are variably altered and metamorphosed to serpentine-tremolite-chlorite-magnetite and lesser talc-carbonate-chlorite assemblages. In order of abundance, they include:

Lherzolites are normally light grey-dark grey and strongly magnetitic. They contain 40–75% modal % olivine (2–10 mm in size; normally altered to serpentine-magnetite along rims and fractures), 10-40 modal % oikocrystic (olivine inclusions) Opx (3-8 mm, often altered to anthophyllite), 10-40 modal % cumulus Cpx (0.2-0.7 mm, altered to tremolite), and 3–5% intercumulus/cumulus chromite (0.2-0.7 mm, variably altered to and/or overgrown by magnetite). Relict igneous olivine is normally surrounded by serpentinized rims and/or contains serpentine-magnetite filled fractures.

Olivine websterites (Fig. 7A-B) are light bluish-grey and essentially non-magnetic. They contain 10–30% cumulus olivine (2-10 mm, commonly but not always altered to serpentine-magnetite), 20–60% oikocrystic Opx (5-10 mm, altered to talc), and 10-50% cumulus Cpx (1-3 mm, altered to actinolite). Altered pyroxenes also contain minor muscovite and biotite.

Wehrlites (Fig. 7C) are dark grey-blue and weakly magnetic. They contain 40–60% olivine (2-10 mm, altered to serpentine-magnetite along rims and fractures), <5% oikocrystic Opx (3-8 mm, altered to anthophyllite), 40–60% intercumulus Cpx (0.5-4 mm, altered to tremolite), and <2% cumulus 0.2–0.7 mm chromite.

Harzburgites are uncommon, but are normally light grey-blue and strongly magnetic. They contain 60–75% cumulus olivine (2-10 mm, altered to serpentine-magnetite along rims and fractures), 20-40% oikocrystic Opx (3-8 mm, altered to anthophyllite), <5% intercumulus Cpx (0.5-4 mm, altered to tremolite), and <2% cumulus/intercumulus 0.2–0.7 mm chromite.

Dunites are rare within the Eagle’s Nest dike or the Double Eagle Intrusion (Azar et al., 2010), but are more common in the nearby Blackbird deposit and the Black Thor Intrusion (Carson et al., 2015, 2018; Carson, Ph.D. in prep.). They are composed of >90% cumulus olivine (2-10 mm, normally altered to serpentine-magnetite ± talc-magnesite) with <10% intercumulus pyroxene and ~1% intercumulus chromite (Carson, Ph.D. in prep.).

Contacts between ultramafic rocks and the country rock tonalite are often diffuse and highly irregular (Fig. 7D), with localized brecciation of tonalite clasts into the dike margins. The chilled margins of the dike examined in this study were highly altered to chlorite-biotite, retaining no original mineralogy or textures.

6.2 Mineralogy

6.2.1 Olivine

Almost all of the olivine in the ores and host rocks at Eagle’s Nest is pseudomorphed by serpentine-magnetite or talc-magnesite, but relict igneous olivine is sporadically preserved within zones of late pyroxenite cross-cutting net-textured mineralization and peridotite.

Olivine is the most common silicate mineral within the Eagle’s Nest dike, occurring as small (2–10 ellipsoidal to prismatic black primocrysts in all of the mineralized and unmineralized rocks forming vermiform networks in some net-textured sulfides and in coarse (2-5 mm) ellipsoidal dunite-peridotite anteliths in inclusion-net-textured sulfides. The vermiform networks resemble some of the habits of crescumulate olivine at Kambalda (Leshner, 1983), but the alteration precludes verification that it formed the optically continuous networks that characterize crescumulate olivine.

Across all rock types, olivine ranges 39-40 wt % SiO₂, 43-45 wt % MgO, and 13-18 wt % FeO with minor MnO (0.3%), NiO (0.2-0.3%), CaO (0.04%), CoO (0.04%), Cr₂O₃ (0.2%), and trace amounts of Al₂O₃ (0.01%), K₂O (0.003%), and Na₂O (0.002%). When recalculated to atomic percentages, olivine in Eagle’s Nest ranges (Mg₄₇₋₄₈Fe₆₋₃₆Ca_{0.03}Mn_{0.15}Ni_{0.1-0.2})₂SiO₄, corresponding to Fo₈₄₋₈₆.

6.2.2 Pyroxene

The vast majority of pyroxene in the ores and host rocks at Eagle’s Nest is altered. Even where uncommon fresh orthopyroxene (Opx) is preserved it is almost entirely cross-cut by fractures containing alteration minerals and could not be analyzed. This hampers discrimination between Opx and clinopyroxene (Cpx), but Opx normally forms coarse (0.5-1 cm) oval to circular oikocrysts containing chadacrysts of fresh Ol and is normally pseudomorphed by grey talc ±

anthophyllite, whereas Cpx normally forms isolated intercumulus crystals and is normally pseudomorphed by grey-blue tremolite.

Opx appears to be most abundant in pinto-net-textured sulfides amongst black serpentinized olivine and interstitial sulfide. Opx is also more abundant in pinto-net textured sulfides than in barren peridotites.

Rare unaltered Cpx ($n = 3$) has a composition of 52.5 wt % SiO₂, 19.6 wt % CaO, 18 wt % MgO, 4.8 wt % FeO, 3 wt % Al₂O₃ with minor Cr₂O₃ (0.9%), Na₂O (0.3%), NiO (0.03%), TiO₂ (0.2%), and trace amounts of MnO (0.1%) and CoO (0.01%).

7 Mineralized Rocks

7.1 Lithologies

The sulfide textural facies in the Eagle's Nest deposit (**Table 1**) are similar to those present in many other komatiite-associated Ni-Cu-(PGE) deposits (e.g., Alexo: Naldrett, 1966; Houlé et al., 2012; Kambalda: Ewers and Hudson, 1972; Raglan: Leshner, 2007; see review by Barnes et al., 2016), but there are several types that have been not been described previously. Each of the textures in the deposit is described below, based on core logging and petrography, and sulfur and sulfide percentages are presented as wt%. Core slab scans, thin sections and μ XRF scans (Zuccarelli et al., 2020) are shown in **Figures 8-23**.

7.1.1 Disseminated Sulfides

Disseminated sulfide (Figs. 8-9) containing $\sim <6\%$ S and 0.5–15 wt% sulfide comprises approximately 5% percent of the known mineralization in the deposit. It is distributed heterogeneously across the deposit, most commonly between underlying net-textured sulfides and overlying barren host rocks. In this facies pyrrhotite-pentlandite-chalcopyrite \pm magnetite \pm chromite occur as very small to small (<0.5 –40 mm), isolated, irregularly- to uniformly-dispersed disseminations in the interstitial spaces between olivine and pyroxene in peridotite and pyroxenite (**Fig. 8**).

Disseminated sulfides occur as lightly, medium, heavily, patchy, and blebby subfacies. Lightly disseminated sulfide occurs as 0.5–5 wt% sulfide distributed in very fine (0.2–0.5 mm) grains. Medium disseminated sulfide occurs as 5–10 wt% sulfide in small to medium (0.5–10 mm) irregular wisps. Heavily disseminated sulfide occurs as 10–15 wt% sulfide in 10–30 mm irregular wisps. Patchy disseminated sulfide (8–10 wt% sulfide) occurs as very small to small (<0.5 –30 mm), isolated, unevenly- to uniformly-dispersed irregular patches. Blebby disseminated sulfide (2–5 wt% sulfide) occurs as small to medium (20–40 mm) rounded to subrounded blebs in the interstitial spaces between olivine and pyroxene in peridotite and pyroxenite. The sulfides within coarser blebs are occasionally fractionated with chalcopyrite-rich upper parts and pyrrhotite-pentlandite-rich lower parts, whereas finer blebs are rarely systematically fractionated.

A typical example of 8% patchy disseminated sulfide is shown in **Fig. 9A**. In the scanned optical image, sulfides are present in wisps and small blebs. In the S-Fe-Ca μ XRF map (**Fig. 9B**), sulfide phases (yellows and oranges) are more abundant in olivine-rich domains (dark green), than in pyroxene domains. Cpx-rich domains contain ellipsoidal peridotite (dark and medium green) and chromitite (bright green) clasts. Some of the latter are embayed. In the Cr-Fe-Ca μ XRF map (**Fig.**

9C), it is possible to identify two types of chromitite clasts: 1) net-textured chromitite where chromite occurs as clusters of single crystals (red to yellow) within olivine-rich domains (dark to dark-green) and 2) rounded ellipsoidal massive chromitite clasts exhibiting varying degrees of alteration to ferrichromite (i.e., red = Cr-rich core, yellow = Cr-poor rim). These textures are more complex than the more uniformly disseminated sulfides in most Ni-Cu-PGE deposits (see Barnes et al., 2017).

7.1.2 Net-Textured Sulfides

Net-textured sulfides (Figs. 10-19) containing approximately 5–12% S and 15–35 wt% sulfide comprises ~80 % of known mineralization along the entire length of the deposit. It consists of 70–85% tightly packed cumulate olivine and pyroxene with 15–30% interstitial sulfides forming thin films between olivine and triangular patches between olivine ± pyroxene. All net textures occasionally exhibit 0.5-5 mm thick, parallel foliations of sulfide that crosscut the sulfides and silicates at 50–80° to the core axis and ~60° to a weak igneous lamination defined by the olivine aggregates. An example of this is in **Figs. 10-11**, which was drilled subparallel to the basal contact of the intrusion; since the sawn surface is not necessarily perpendicular to the foliation (non-oriented core), the sulfide foliation may be perpendicular to oblique to the original basal contact of the intrusion, but the igneous lamination cannot be any less oblique (corresponding to ~60°–90° to original basal contact).

Leopard-net-textured sulfide (Figs. 10-11) is the most common subfacies of net texture. It comprises ~52% of all net-textured sulfides and contains ~7–14% S and ~15–35% wt% sulfide. It consists of ~65–85% cumulus olivine and lesser intercumulus altered clino/orthopyroxene and ~25–30% interstitial sulfide forming thin films between olivine, and triangular-shaped patches between olivine ± altered clino/orthopyroxene. Olivine and clino/orthopyroxene are bimodal, ranging in size from 1–3 mm to 5–15 mm. The coarser crystals and lesser crystal aggregates are what define this texture as “leopard net”, as the large black pseudomorphs of serpentine-magnetite after olivine among the network of yellowish sulfides gives the appearance of a leopard coat. The sulfide assemblage is composed of pyrrhotite > pentlandite > chalcopyrite.

Abundant magnetite occurs as irregularly distributed grains (> 0.5 mm) throughout both sulfide and silicates. Sulfide blebs rarely occur within magnetite crystals, but exhibit internal fractionation (chalcopyrite at the inferred top, pyrrhotite-pentlandite at the inferred base).

A typical example of leopard-net-textured sulfide is shown in **Fig. 11**. In the scanned optical image, sulfides are evenly distributed except within serpentinized olivine mesocrysts (dark black) and fine grained aggregates (dark greyish-black phases) (**Fig. 11A**). In the Ni-Cu-S map (**Fig. 11B**), abundant chalcopyrite (green) forms an anastomosing network around very fine and very coarse olivine (black), most of the pentlandite (magenta) occurs more sporadically, and most of the pyrrhotite (blue) defines a foliation oriented ~60° to the core axis and ~60° to a weak igneous lamination defined by the olivine aggregates. In the Cr-Fe-Ca map (**Fig. 11C**), coarse serpentinized olivine (black) is oikocrystic, containing fine chromite (red) and ferrichromite (yellow) chadacrysts, or xenolithic, comprising clasts of chromite-bearing dunite. The matrix is fine disseminated Cpx (blue) and Fe-bearing sulfides (green).

Inclusion-net-textured sulfide (Figs. 12-13) is an uncommon variety of net-textured sulfide (<1% of total net-textured sulfide) and contains ~4–10% S and ~15–30 wt% sulfide. It has all the same features of leopard-net texture with the exception of a wider variety of clinopyroxene, ranging

from 10–15% of silicates, and the presence of up to 300 mm-long silicate inclusions. The inclusions are typically dunite-peridotite in composition and vary from subrounded to rounded, differing from the lesser olivine aggregates (i.e. leopard ‘spots’) in leopard-net texture due to their highly irregular distribution. The contacts between inclusions and net-textured sulfide are irregular, due to the infiltration of sulfides between olivine-pyroxene grains in the clasts themselves. One particularly large (30 cm) inclusion in inclusion-net texture is exceptionally angular (**Fig. 12A**), but exhibits the same irregular and diffuse edge as other clasts within inclusion-net texture.

In the optical image (**Fig. 13A**), sulfide is not evenly distributed and is controlled mainly by the distribution of inclusions and to lesser extent olivine. In the Ni-Cu-S map (**Fig. 13B**), pentlandite (magenta), pyrrhotite (blue), and lesser chalcopyrite (cyan or green) occur both in large domains with silicates (reddish-black in this image) and in fine pyrrhotite-pentlandite-rich filaments oriented $\sim 90^\circ$ to the core axis (subparallel to the dike contact). Chalcopyrite, silicates, and lesser pyrrhotite-pentlandite dominate the other domains. In the Cr-Fe-Ca map (**Fig. 13C**), it is clear that the silicate phases include coarse-grained olivine (black) containing small inclusions of chromite (red), orthopyroxene (opalescent), medium-grained clinopyroxene (blue), and fine-grained olivine (black) within sulfide (green). The 1 cm inclusion in this sample is a serpentinized peridotite composed of serpentine (black) with magnetite (green) veinlets and fine chromite inclusions (red).

Pinto-net-textured sulfide (Figs. 14-15) is an uncommon variety of net-textured sulfide. It makes up <5% total net textured sulfide and contains ~ 3 –11% S and ~ 15 –30 wt% sulfide. Pinto-net-textured sulfide is most commonly found as 1–2 m zones among areas of disrupted-net texture, or where leopard-net texture meets barren pyroxene regions. It is similar to leopard-net in that it consists of small serpentinized olivine surrounded by interstitial sulfides, but differs with large (0.3–10 mm) subhedral-euhedral oikocrysts of talc-carbonate altered pyroxene (appearing whiteish-grey in core) with distinctive optical properties indicating original orthopyroxene composition. The oikocrysts of orthopyroxene are what define this texture as ‘pinto net’, as the large grey-white oikocrysts among the network of black serpentinized olivine and yellowish sulfides is similar to the appearance of white spots on the otherwise dark coat of a pinto-textured horse. The oikocrysts contain both fresh olivine, and serpentinized olivine. The interstitial sulfides consist of pyrrhotite, pentlandite and chalcopyrite up to 1 mm in diameter. Magnetite exists in anhedral and infrequent euhedral blebs up to 0.5 mm in diameter, and sometimes contains inclusions of sulfide.

A typical example of pinto net-textured sulfide facies is shown in **Fig. 15**. In the optical image (**Fig. 15A**) the amount of sulfide is relatively small (~ 20 –25%) and occurs almost exclusively in close association with small serpentinized olivine crystals (black) interstitial to coarse sulfide-free orthopyroxene oikocrysts (grey) (**Fig. 15A**). In the Ni-Cu-S map (**Fig. 15B**), pyrrhotite (blue), pentlandite (magenta), and chalcopyrite (green) are more-or-less evenly disseminated throughout the sample except within the large weakly aligned pyroxene domains (black). Nevertheless, chalcopyrite is more common on peripheries of the pyroxene oikocrysts. In the Cr-Fe-Ca map (**Fig. 15C**), the matrix is dominated by sulfides (green) and fine-grained olivine (black), and the pyroxene-rich domains include parts comprising mainly orthopyroxene (black), chromite (red), and ferrichromite (orange and yellow) as well as parts comprising mainly clinopyroxene (blue).

Disrupted-net-textured sulfide (Figs. 16-18) is a localized but common form of net-textured sulfide ($\sim 28\%$ of net-texture) containing ~ 6 –10% S and 18–25 wt% sulfide. It appears as localized <20 m zones predominantly between 500–900 m depth in the deposit, although it is not restricted

to that area. Disrupted-net texture appears as highly irregular serpentinized olivine cumulate patches surrounded by interstitial sulfide, directly adjacent to barren regions of talc-carbonate altered pyroxenite. In drillhole NOT-09-053, a large, 50 cm zone of barren pyroxenite can be found cutting through disrupted net, with a very similar style contact with olivine cumulates on its edges (**Fig. 16**) The first ‘disrupted-net texture’ (DN in Fig. 16) section (857.1-857.7 m) contains olivine cumulate and interstitial sulfide with highly irregular 2-10 cm zones of pyroxenite throughout. The central barren pyroxenite (857.7m-858.2 m) contains minimal mineralization and relict olivine, with a gradual transition back to leopard-net texture (858.2-858.4 m). In disrupted-net-textured sulfide, the most abundant sulfide mineral is pyrrhotite, with varying amounts of pentlandite (0.1-0.5 mm) and chalcopyrite (0.1-3 mm). Magnetite occurs sporadically in both barren and mineralized areas, occurring up to 0.5 mm in diameter, and ranging from anhedral to euhedral. Minor chromite is also present.

The contacts between the cumulate and barren zones are very irregular and ‘wispy’, with some serpentinized olivine crystals/chains isolated from their respective cumulates and seen ‘floating’ in the pyroxenite (**Figs. 17A-B**). The barren pyroxenite zones contain frequent fresh olivine which can be up to 4mm in diameter, but almost all olivine in the cumulates containing interstitial sulfide are serpentinized (**Figs. 17C-H**).

A typical example of disrupted-net-textured containing ~25 wt% sulfides is shown in **Fig. 18**. The optical image (**Fig. 18A**) indicates that sulfide is much more abundant in leopard-net-textured domains containing abundant fine-grained serpentinized olivine (black) and much less abundant in areas containing abundant pyroxene (grey) of the pyroxenite. In the Ni-Cu-S map (**Fig. 18B**), there is a zonation away from the pyroxenite from i) pyrrhotite (blue) \approx pentlandite (magenta) \gg chalcopyrite (green) through ii) chalcopyrite \gg pyrrhotite \approx pentlandite to iii) pyrrhotite \approx pentlandite $>$ chalcopyrite. In the Cr-Fe-Ca map (**Fig. 18C**), the distinction between the pyroxenitic material (blue), which contain patches of residual olivine (black), magnetite (yellow), and chromite (red), and the surrounding net-textured sulfides (green; all sulfide facies), is more distinct.

Patchy-net-textured sulfide (Fig. 19) is a moderately common sulfide texture (~14% of all net texture) which occurs adjacent to leopard-net-textured and disrupted-net-textured sulfides and contains ~3–10% S and ~15–25 wt% sulfide. It appears as peridotite with 50–60% 1–3 mm diameter olivine and 40–50% interstitial altered pyroxene, with isolated patches of sulfide that do not visually connect on the two-dimensional surface of the half core. Patchy-net-textured sulfides differ from leopard net-texture because all olivine crystals are uniform in size, and interstitial sulfide occurs irregularly. Patchy-net texture differs from disrupted net because no patches of barren pyroxenite occur. Sulfides are predominantly pyrrhotite and contain with varying amounts of pentlandite (0.1–1 mm) and chalcopyrite (0.1–4 mm). Magnetite can be commonly found between some silicate minerals, but also as indiscriminate euhedral-subhedral minerals up to 1 mm in diameter.

7.1.3 Semi-Massive Sulfides

True semi-massive sulfide, defined as massive sulfide containing lithic silicate inclusions, (**Fig. 20**) is very uncommon in the Eagle’s Nest deposit (~7% mineralization) but contains ~18–30% S and ~50–80 wt% sulfide. It occurs in both the lower and upper parts of the deposits, although most commonly along the footwall. Semi-massive can generally be described as massive sulfide (**Fig. 21**) containing ~10–20% silicate inclusions. The non-sulfide component is normally composed of

gabbro or tonalite xenoliths derived from the country rocks and peridotite anteliths or autoliths (AKA “cognate xenoliths” derived from this or other phases of the intrusive system). Although much less common, sulfide-bearing inclusions also occur within this facies and are normally composed of leopard-net-textured sulfides. Semi-massive sulfides contain no olivine and pyroxene crystals, except those within ultramafic inclusions. In thin section, the sulfide portion of semi-massive sulfides appears similar to massive sulfide, although with more chalcopyrite.

7.1.4 Massive Sulfides

Massive sulfide (**Fig. 21**) is highly localized within Eagle’s Nest, and contains $\sim >30\%$ S and $\sim >80$ wt% sulfide. It occurs predominantly within two $\sim 100 \times 50$ m pockets at 100 m and 450 m depths. In all other areas it occurs as 0.5-10 m lenses, or as cross-cutting veinlets (30-50 mm thickness). Massive sulfide is yellow-brass in colour, with 50–75% pyrrhotite, 20–25% pentlandite (2–20 mm) and 0.5–9% chalcopyrite (5–100 mm). Pentlandite often occurs as distinctly reflective, roughly circular crystals, and chalcopyrite occurs as irregularly distributed grains throughout and as concentrations along contacts with host rocks, in fractures or in secondary veining.

In thin section (**Figs. 21H-I**), pyrrhotite contains fractures that often host anhedral pentlandite and chalcopyrite, and < 0.5 mm flames of pentlandite occur perpendicular to these fractures. Pyrrhotite is pinkish-brown in colour and also contains euhedral-subhedral magnetite ranging from 0.5-3 mm. In thin section, pentlandite occurs as large pale yellow ‘eyes’ that range from 1-20 mm in diameter and show higher relief than pyrrhotite, and can exist with multiple minerals forming clusters, or as smaller eyes distributed regularly throughout the sample (right side of **Fig. 22A**; see semi-massive sulfide section above). Chalcopyrite occurs as irregular patches throughout massive sulfide 1-5 cm in diameter. All massive sulfides also contain irregularly distributed magnetite (0.5-5 mm). There are often small (< 100 microns) PGMs associated with massive sulfide as well, composed mostly of Pd, Bi and Te. In some massive sulfide samples, small ductile deformation structures seen predominantly in alignment of Ccp and Pn, although this is not common.

A contact between semi-massive and massive sulfide facies is shown in **Fig. 22**. The amount of sulfides varies from $\sim 60\%$ in semi-massive sulfides (left side of **Fig. 22A**) to $\sim 95\%$ in massive sulfides (right side of **Fig. 22A**). The semi-massive sulfide domain contains abundant inclusions of altered, recrystallized, and partially-melted gabbro. In the Ni-Cu-S map (**Fig. 22B**), it is clear that the semi-massive sulfides are composed of pyrrhotite (blue) \gg pentlandite (magenta) \approx chalcopyrite (cyan) and that the massive sulfides are composed of pyrrhotite $>$ pentlandite \approx chalcopyrite. Pentlandite and chalcopyrite are finer grained and more dispersed (as patches and along pyrrhotite grain boundaries) in semi-massive sulfides, and coarser grained and more segregated in massive sulfides. In the Cr-Fe-Ca map (**Fig. 22C**), pyrrhotite is bright green, and pentlandite and chalcopyrite are both dark green. The sulfides minerals display a combination of coarse granular pentlandite (at contacts with chalcopyrite) and thin (sub-mm) “loops” of exsolved pentlandite (commonly in semi-massive sulfides around pyrrhotite grain boundaries). The inclusions contain a Ca-rich phase (dark blue), likely altered clinopyroxene based on the habit, and a Cr-Fe-Ca-poor phase (black), likely altered (albitic) plagioclase. Ferrichromite (orange) occurs as isolated crystals and as rims on inclusions.

A contact between semi-massive/massive sulfide and leopard-net-textured sulfide facies is shown in **Fig. 23**. The amount of sulfides in the semi-massive ‘vein’ is $\sim 60\%$ (central part of **Fig. 23A**). The semi-massive sulfide domain contains abundant inclusions of a Ca-rich phase. In the Ni-Cu-S map (**Fig. 23B**), it is clear that the semi-massive sulfides are composed of pyrrhotite (blue) \gg

pentlandite (magenta) \approx chalcopyrite (cyan) and that there is abundant chalcopyrite (green) along the contact between semi-massive and leopard-net-textured sulfide. Pentlandite and chalcopyrite are in large patches in semi-massive sulfides, and more segregated in massive sulfides. In the Cr-Fe-Ca map (**Fig. 23C**), pyrrhotite is bright green, and pentlandite and chalcopyrite are both dark green. The Ca-rich phases stand out from the Fe-rich (green) sulfides. The sulfides minerals display a combination of coarse granular pentlandite (at contacts with chalcopyrite) and thin (sub-mm) “loops” of exsolved pentlandite (commonly in semi-massive sulfides around pyrrhotite grain boundaries).

7.1.5 Contacts between Sulfide Textures

The vast majority of contacts between sulfide textures are gradational, occurring over >30 cm, with three exceptions. The first is within disrupted-net texture, where larger zones of apparently cross-cutting pyroxenite often exhibit irregular but abrupt contacts with net-textured sulfide. The second is between massive sulfide and silicate lithologies, which are extremely sharp and bordered by skeletal chromites/ferrichromites. The third is between contacts of massive sulfide/cross-cutting massive sulfide veins with all lithologies. These veins typically cause chalcopyrite to bleed into existing interstitial sulfide within net-textured sulfide, significantly increasing the sulfide:olivine ratios proximal to the vein contact and similar to ‘soft-walled veins’ described in Barnes et al. (2017).

7.2 Sulfide Mineralogy

Representative chemical compositions of major silicate and sulfide minerals are given **Electronic Appendix A, Table 2** and plotted in **Fig. 24**.

Pyrrhotite (Fe_{1-x}S) is the most common sulfide mineral in the Eagle’s Nest deposit. In core, it appears light brownish-pink and is magnetic. Pyrrhotite is the most abundant sulfide in the interstitial mineralization between silicate minerals in all net textured sulfide ores, and most blebs within disseminated sulfide are also pyrrhotite. Pyrrhotite contains 36-41% S (Avg. 39%), 55-64% Fe (Avg. 60%), 0.04-0.9% Ni (Avg. 0.3%), 0.001-0.016% Co (Avg. 0.006%), 0.005-0.023% As (Avg. 0.005%) and, 0.001-0.05% Ag (Avg. 0.02%) (**Fig. 24**).

Pentlandite ($\text{Fe,Ni}_9\text{S}_8$) is the main nickel-bearing sulfide mineral in the Eagle’s Nest deposit. In core, it appears bright brown-beige, noticeably more yellow than surrounding pyrrhotite. It exists as either coarse anhedral ‘eyes’ (5-20 mm), small anhedral crystals within pyrrhotite (0.1-0.5 mm), or as exsolution ‘flames’ in fractures within pyrrhotite (<0.1 mm diameter). Small anhedral crystals of pentlandite occur in all the net textured sulfides, with some occurring in disseminated sulfides as well, and in some of the coarser ‘eyes’ there is clear alteration of the pentlandite in the form of Co-rich fractures and stringers.

Pentlandite contains 35-37% S (Avg. 36%), 25-37% Fe (Avg. 31%), 29-38% Ni (Avg. 33%) 0.3-2% Co (Avg. 1%), 0.009-0.025% As (Avg. 0.01%), and 0.001-0.045% Ag (Avg. 0.02%) (**Fig. 24**).

Chalcopyrite (CuFeS_2) is the major copper sulfide mineral in the Eagle’s Nest deposit and exists as large brassy yellow patches (>60 mm) within massive sulfide ore. It also occurs as smaller crystals (0.5-1 mm) within pentlandite, and as remobilized veinlets in net-textured sulfides. Chalcopyrite is common adjacent to contacts between host rock and deposit rock, and where massive sulfide contacts other sulfide textures.

Chalcopyrite contains 34-36% S (Avg. 35%), 33-35% Cu (Avg. 34%), 29-32% Fe (Avg. 31%), and 0.002-0.023% Co (Avg. 0.003%) (**Fig. 24**). It also contains 0.009-0.029% As (Avg. 0.01%) and 0.001-0.061% Ag (Avg. 0.02%).

Most of the PGM in the Eagle's Nest deposit appears to be merenskyite (Pd,Pt)(Te,Bi)₂ and michenerite (PdBiTe, occurring as small crystals (< 20 μm) within massive sulfide and net-textured sulfide (**Fig. 25**). These are relatively common, with at least 1-2 grains visible in each sample, although several uncommon examples of PGMs in massive sulfides are up to ~110 μm in diameter. Other interesting minor minerals include electrum (Ag-Au) in some altered samples of net-texture, occurring as small < 10 μm grains among patches of amphibole alteration. Most PGM are slightly zoned, but one sample of massive sulfide contained a ~40 μm concentrically-zoned euhedral mineral with a Pt-bearing core, a Pd-bearing inner zone, and an As-bearing outer rim.

8 Whole-Rock Geochemistry

Whole-rock geochemical compositions of the host rocks and ores are given in **Table 3 and 4, Appendix B** and plotted in **Figures 26-37**. Where indicated, data from this study are presented in comparison with Noront's assay data to provide an accurate overview of the deposit.

8.1 Host Rocks

Non-mineralized peridotites and pyroxenites in the Eagle's Nest dike vary between ~22–38% and ~21–34% MgO (**Fig. 26**), respectively, and plot along the same trends as barren host rocks at Black Thor (Carson, Ph.D. in prep.). For other elements, Si-Ti-Ca (**Figs. 26A-B, F**) increase with decreasing Mg except for samples containing significant Opx (which plot at lower Si-Al-Ca). The same trends are observed for the silicate components of disseminated and net-textured mineralization. Cr-Fe (**Fig. 26D, 26E**) broadly decrease with decreasing Mg, and olivine analyzed plot along the trend of Fo₈₃₋₈₆, while most samples plot along the cotectic olivine-chromite cumulate trend but some plot below it. Importantly, most of the trends from mineralized rocks project to olivine compositions and equilibrium liquids that are more magnesian than any of the analyzed olivines (**Fig. 26E**).

All rocks in the dike are enriched in highly incompatible lithophile elements (HILE; Cs-U-Th-LREE) relative to Nb-Ta-Ti and moderately incompatible lithophile elements (MILE: Zr-Hf-MREE-Y-HREE) (**Fig. 27**). Two pyroxenite samples are significantly enriched in Li-Rb-Ba.

In terms of Nb/Tb vs Th/Yb (**Fig. 28A**), the data ranges between 0.1-1 Th/Yb and 0.9-2 Nb/Yb, extending between N-MORB and E-MORB toward Archean felsic (i.e., upper) continental crust. The enrichment in Th (and other HILE) ranges up to 30-40% contamination (**Fig. 28B**).

8.2 Ores

8.2.1 Sulfur Content

In terms of wt % S, massive sulfides contain ~28-37.5% S, semi-massive sulfides contain ~18-30% S, net-textured sulfides contain ~5-12.5% sulfur, and disseminated sulfides contains ~<2.5% S. These differ slightly from the nominal sulfur contents of similar textures at other deposits (**Table 1**).

The S contents of subfacies of net-textured sulfide are plotted as a histogram in **Fig. 29**. Leopard net-textured sulfides contain ~9.5-12% S, disrupted-net-textured sulfides ~6-12.5% S, pinto-net-textured sulfides ~3.5-11.5% S, inclusion-net-textured sulfides ~4-10.5% S, and patchy-net textured sulfides ~3-10% S. These values fall within the range of nominal net-textured ores in **Table 1**, but Eagle's Nest net-textured ore range to lower sulfide content.

8.2.2 Metals versus S

Ni, Cu, and Fe increase with increasing sulfur content (**Fig. 30A-C**) indicating they are housed within sulfides. Pd-Pt increase only weakly with increasing S, indicating that they are housed in sulfides and non-sulfide phases, that magmas did not contain a significant amount of these elements, or that they have been mobile during metamorphism (**Fig. 30D-E**). There is a very weak correlation between increasing Ag and increasing S (**Fig. 30F**), and little to no correlation between Au and sulfur content (**Fig.30G**).

8.2.3 Elemental Variations

The abundances of metals in the different ore facies in the Noront assay database and in the ore subfacies analyzed in this study are presented as box plots (Tukey plot mode in ioGAS v.7.0) in **Figures 31-35**, with the lower fence/whisker representing the interquartile range (IQR: box length) divided by 1.5, the lower part of the box the 25th percentile, the upper part of the box the 75th percentile, and the upper fence/whisker representing IQR * 1.5. The dot represents the mean and the horizontal line represents the median. Outliers (between IQR * 1.5 and IQR *3) and far outliers (>IQR * 3) are represented by open circles and far outliers, respectively, and have not been included in ranges described in the text.

S: The Noront assays (**Fig. 31A**) and breakdown of net-textured sulfides (**Fig. 31B**) have already been described in Section 8.2 (**Fig. 4, Fig. 29**); the histograms in **Figure 31** provide details on outliers as well as statistical details of wt % S for each texture.

Ni: Massive sulfides contain ~5-10% Ni, semi-massive sulfides contain ~0.5-8% Ni, net-textured sulfides contain ~0.5-3% Ni and disseminated sulfides contain ~<1% Ni (**Fig. 31B**). In general leopard-net texture contains more Ni (~1.5-3%) than other net textures (~0.5-2.50%) but overall net textures cannot be distinguished by Ni content (**Fig. 31C**).

Cu: Massive sulfides contain ~0.1-10% Cu, semi-massive sulfides contain ~0.1-12%, net-textured sulfides contain between ~0.1 and ~2.5%, and disseminated sulfides contain <0.5% (**Fig. 31E**). Inclusion-net-textured sulfides contain the most Cu by far (~0.25-4.75%) which correlates with the preference of chalcopyrite to form on the edges of clasts. All other net textures contain ~0.1-1.75% Cu (**Fig. 31F**).

Fe: There is a gradational overlap in wt % Fe (**Fig. 31G**) from disseminated sulfide (~2.5-12.5%) and net-textured sulfides (~10-23%), net-textured sulfides to semi-massive sulfides (~20-45%) and massive sulfide (~27-50%). All net textures strongly overlap with Fe%, which means this cannot be used to distinguish them from each other (**Fig. 31H**).

Ca: Disseminated sulfide by far has the widest range (~0.1-7% CaO), whereas massive sulfide has the narrowest range (0.1-0.5% CaO) (**Fig. 32A**). Leopard net-textured sulfide (~0.1-0.25% CaO) contains significantly less Ca than all other net textures (~0.3-2.75%), allowing it to be distinguished from other textures on the basis of chemistry (**Fig. 32B**).

Pd and Pt: Massive sulfide contains the widest range of Pd (~0.1-23 ppm), whereas disseminated sulfide contains the least (~0.1-2 ppm) (**Fig. 32C**). There are no significant variations in Pd content amongst the net-textured sulfide subfacies, although leopard net-texture has the highest consistent Pd content (~2.5-5 ppm versus ~0.1-5 ppm for all other textures) (**Fig. 32D**). This is a general indicator that palladium is associated with sulfide. Platinum contents are not distinguishable between all major textures, with the general range between ~0.1-5.25 ppm (**Fig. 32E-F**).

Au and Ag: Gold and silver contents (**Fig. 33A-D**) range ~0.1-0.65 ppm and ~0.1-25 ppm, respectively with no differences between different ore textures and only a poor correlation with S content.

8.2.4 Metal Tenors

Metals were recalculated to 100% sulfide to compare samples containing different abundances of sulfides and to establish metal modal mineral abundances. This was done using the method of Naldrett (1979) in which Cu is allocated to stoichiometric chalcopyrite (34.62% Cu, 30.43% Fe, 34.94% S), Ni is allocated to pentlandite (34.15% Ni, 31.06% Fe, 33.72% S, equivalent to $\text{Fe}_4\text{Ni}_5\text{S}_8$) after correction for 0.2% Ni in olivine, and the remaining S is allocated to pyrrhotite (61.05% Fe, 38.94% S, equivalent to $\text{Fe}_{0.9}\text{S}$). These values are based on analyzed mineral compositions from this deposit (see section 7.2: Sulfide Mineralogy).

Ni_{100} values are roughly similar for all textures (~3-12%: **Fig. 34A**), with a much larger range in disseminated sulfides (0-47.5%). Within the subfacies of net textures, Ni_{100} values are relatively consistent (~6-8.5%) with the exception of inclusion net-textured sulfide (~3-7.5%) (**Fig. 34B**). Based on Noront Resources assays, Cu_{100} (**Fig. 34C**) ranges ~0.1-12%, with the exception of semi-massive sulfides which have an upper extent of 18% Cu_{100} . Within the subfacies of net-textured sulfides, leopard-net texture (~1-6%), pinto net-texture (~0.5-3%) and disrupted net-texture (~1-4%) have similar Cu_{100} compositions, inclusion-net texture (~1-17%) and patchy-net texture (~2-9%) have far broader ranges (**Fig. 34D**).

Based on these tenors, massive sulfide contains ~12.5–28% pentlandite and ~0.1–28% chalcopyrite. Semi-massive sulfides contain ~2–25% pentlandite and ~0.1–33% chalcopyrite, net-textured sulfides contain ~2.5–8% pentlandite and ~0.1–8% chalcopyrite, and disseminated sulfides contain ~0.1–2.5% pentlandite and <2% chalcopyrite. When breaking down net-textured sulfides into the five subfacies, leopard-net contains ~4–8%, and other net textures contain ~1.5–7% pentlandite. Inclusion-net by far contains the largest range of chalcopyrite, (~1–14%) all other textures contain ~0.5–5%.

Ni_{100} decreases with increasing Cu_{100} (**Fig. 35A**) in the Noront dataset and the inclusion net-textured samples in this study. Pt_{100} and Pd_{100} correlates poorly with Cu_{100} (**Fig. 35B**). The calculated R-factor trends from this study (see section 8.7) and from an earlier study (Mungall et al., 2010) are plotted for reference.

8.2.5 Mantle-Normalized Metal Variations

The Ni-Cu-(PGE) mantle-normalized metal abundances of average Eagle's Nest ore types and the ranges for Kambalda and Raglan ores are given in **Figure 36**. The amount of each element in each major ore type (massive, semi-massive, net-textured, disseminated) is based on the median from Noront Resources assays, divided by the amount of each element in primitive mantle (Taylor and McLennan, 1989). In a general sense and with the exception of disseminated sulfides, Eagle's

Nest ores follow the same enrichment-depletion pattern as Kambalda and Raglan ores. Eagle's Nest ores (massive, semi-massive, net-textured sulfides) are consistently slightly more enriched than Kambalda and Raglan ores in Pd, Cu, Pt, and Rh, but similar to Raglan and Kambalda in terms of Ru, Os, and Co.

8.2.6 Magma to Sulfide Ratios

The abundances of Ni, Cu, Co, and Pd in sulfide as a function of variations in the magma : sulfide + olivine ratio (R' : **Fig. 37**) were calculated using the method of Lesher and Burnham (2001), assuming 900 ppm Ni, 60 ppm Cu, 100 ppm Co, and 10 ppb Pd in the magma (Lesher and Campbell, 1993), 2238 ppm Ni, 4 ppm Cu, 180.2 ppm Co, and 0.01 ppb Pd in olivine (EMPA from this study), and an olivine:sulfide ratio of 60:1. Based on these trends and focusing primarily on Pd (which has the highest sulfide/silicate partition coefficient), the range of R' factors for Eagle's Nest ores for this study would be 100–200, averaging ~150, which is slightly lower than the value of 225 calculated from the Noront database by Mungall et al. (2010) who used similar metal contents in the magma, but who did not include the influence of olivine in the mass balance calculations.

8.2.7 S Isotopes

Eagle's Nest ores range narrowly between +1.2 to -0.3 ‰ $\delta^{34}\text{S}$ (**Table 5, Fig. 38**), within the -3 to +2 range of sulfides in the Black Thor Intrusion (Farhangi, 2020), within the -0.5 to -2 range of Black Label sulfides, and within the range of some Blue Jay data, but far outside the range of the outliers (-15 to +0.5). The Eagle's Nest values are close to but slightly heavier than the 0.1 ± 0.5 range for MORB (Sakai et al., 1984), but also within the range of sulfidic iron formation (IF) in the footwall of the Black Thor intrusion (Carson, Ph.D. in prep.). There are no significant differences between different sulfide textures, suggesting that all S in the Eagle's Nest deposit had a similar source.

9 Discussion

9.1 Geometry of the Eagle's Nest Dike

Although the Eagle's Nest Dike is presently a subvertical flattened pipe (**Fig. 3**), the following features suggest that it was originally emplaced as a subhorizontal blade-shaped dike that was subsequently rotated $\sim 90^\circ$ to the SE:

- 1) All of the contacts and layering in the Esker intrusive complex, including the Black Thor and Double Eagle intrusions and all of the stratiform chromite horizons, dip subvertically or steeply to the NW and exhibit textures and geochemical variations consistent with them younging to the ESE but emplaced subhorizontally, and therefore rotated into the present position (Mungall et al., 2010; Tuchscherer et al., 2010; Carson et al., 2015; Metsaranta and Houlé, 2020; Houlé et al., 2020; Carson, Ph.D. in prep.).
- 2) The SE-grading massive/net/disseminated sulfide segregation profile in the upper embayment of the Eagle's Nest deposit has been attributed to gravitational segregation in all other deposits of this type (e.g., Naldrett, 1966; Ewers and Hudson, 1972; Usselman et al., 1979; see reviews by Lesher, 1989; Naldrett, 2004; Barnes and Lightfoot, 2005; Barnes et al., 2016), also consistent with the mineralization younging to the ESE but emplaced subhorizontally, and therefore rotated into the present position.

- 3) The SE gradation from peridotite (olivine-pyroxene cumulates) to pyroxenite (pyroxene cumulates) in the Eagle's Nest Dike is not a diagnostic indicator of younging to the SE, as some intrusions exhibit reverse gradations (e.g., Perseverance: Barnes et al., 1995), but the consistency of this gradation along the exposed length of the dike is consistent with the intrusion having been originally emplaced subhorizontally (Zuccarelli et al., 2018).

Rotation of the Esker intrusive complex and the Eagle's Nest Dike 90° back to the NW, would restore all of the igneous layering to a gravitationally stable subhorizontal orientation and leave the Eagle's Nest Dike ~250m beneath the Double Eagle intrusion (Laudadio, 2019). The geometry would then be that of a subhorizontal blade-shaped dike (Mungall et al., 2010) with mineralization along the keel. Asymmetrically-differentiated mineralized blade-shaped dikes have also been identified in the Expo Intrusive Suite in the Cape Smith Belt (Mungall, 2007), at Savannah in Western Australia (Barnes and Mungall, 2018), and in several localities in China (Lu et al., 2019) (see review by Lesher, 2019). Blade-shaped dikes appear to form only in areas where density contrasts in the country rocks limit upward ascent and where a radial stress field favours linear rather than planar magma emplacement (e.g., Pollard and Rubin, 1987; Bolchover and Lister, 1999).

The irregular lower contact of the dike may represent the original morphology of the intrusion, but it may also have been enhanced by preferential thermomechanical erosion below the high-density, low-viscosity molten sulfides (e.g., Groves et al., 1986; Lesher, 1989; Williams et al., 1989). Barnes and Mungall (2018) suggest a dynamic mechanism whereby sulfide liquid derived from assimilation of country rock at higher level accumulates gravitationally at the lower edge of the blade and partially drives the downward propagation of the dike during its emplacement.

9.2 Genesis of Silicate Rocks

9.2.1 Connection to Other Deposits in Esker Intrusive Complex

The lithologies, mineralogy, mineral chemistry, and geochemistry of the Eagle's Nest Dike are similar to those of the Double Eagle intrusion (Azar, 2010; Mungall et al., 2010) and the Black Thor intrusion (Carson, 2015; Carson, Ph.D. in prep.), suggesting that they are petrogenetically related. However, the Eagle's Nest Dike contains predominantly peridotite, pyroxenite, and sulfides with sparse chromitite inclusions, whereas the Double Eagle and Black Thor intrusion contains dunite, peridotite, gabbros, and chromitites with negligible (Double Eagle) or minor (Black Thor) sulfides (Farhangi et al., 2013; Farhangi, M.Sc. 2020.).

The paucity of adcumulate dunite and chromite mineralization (other than anteliths) in the Eagle's Nest Dike and the relatively small amounts of Fe-Ni-Cu sulfides in the Double Eagle intrusion, suggests that the Eagle's Nest Dike is not the feeder to the Double Eagle Intrusion (Houlé et al., 2020), which is consistent with a 3D geological model (Laudadio, 2019). If so, this suggests that the Double Eagle intrusion was fed from an unexposed or eroded part of the plumbing system, and that the Eagle's Nest Dike fed another unexposed or eroded intrusion. More drilling is needed to test these possibilities, but similar inconsistencies between the composition of putative feeder dikes and sills and overlying volcanic rocks have been observed at Thompson (Lesher et al., 2001), Norilsk (Latypov, 2002), Raglan (McKevitt et al., 2020, Bazilevskaya, 2009), and other areas (see review by Lesher, 2019), highlighting the complex nature of magmatic plumbing systems.

9.2.2 Parental Magma and Contamination

The parental magma for Eagle's Nest and other parts of the Esker intrusive complex has previously been estimated to have contained ~22% MgO and ~12% FeO_t (Mungall et al., 2010; Azar, 2010; Carson et al., 2015), which would have been in equilibrium with ~Fo₉₀ olivine. However, Laarman (2014) reported olivine up to Fo₉₄ in the Black Label zone of the associated Black Thor intrusion, Carson (in prep.) has noted that the compositions of large numbers of Black Thor dunites/peridotites require that they contained (prior to serpentinization) olivine up to Fo₉₄, and many of the higher-Mg, lower-Fe peridotites (barren and recalculated sulfide-free) analyzed in this study also appear to have contained olivine with a composition up to Fo₉₄.

Importantly, a small but significant number of Eagle's Nest rocks have Cr contents that are consistent with accumulation of olivine and less-than-cotectic proportions of chromite (**Fig. 26D-E**), also consistent with a more magnesian liquid (Murck and Campbell, 1986; Leshner and Stone, 1996). Together, this suggests that the parental magma contained ~28% MgO and ~10% FeO_t, making it a high-Mg komatiite (Carson, in prep.). The maximum Fo₈₄₋₈₆ analyzed in this study and the maximum Fo₈₂₋₈₆ analyzed by Mungall et al. (2010) can be attributed to the most magnesian olivine not being analyzed (very few are preserved), fractional crystallization ± crustal contamination, and/or re-equilibration with trapped liquid (see Barnes, 1986; Cawthorn et al., 1992; and discussion by Mungall et al., 2010).

The enrichments in HILE relative to MILE (**Fig. 27**) with negative Nb-Ta-(Ti) anomalies and the Th/Yb versus Nb/Yb diagram are consistent with up to ~30-40% crustal contamination of a mantle-derived magma (**Figs. 28A-B**), significantly more than the 13% inferred by Mungall et al. (2010). Because all rocks are contaminated, the majority of the contamination most likely occurred below rather than within the current conduit (see discussion by Leshner and Arndt, 1995; Leshner et al., 2001).

9.2.3 Minerals and Alteration

Like most other komatiite-associated Ni-Cu-(PGE) deposits (see Leshner, 1989; Leshner and Keays, 2002; Barnes, 2006; Arndt et al., 2008; Leshner and Barnes, 2009), the Eagle's Nest Dike contains mainly olivine-rich cumulate rocks. Where olivine exhibits highly elongate, embayed, or branching crescumulate textures and/or in other deposits where olivine compositions vary systematically with stratigraphic height (e.g., Kambalda: Leshner, 1989; Raglan: Leshner, 2007) it appears to have crystallized in situ rather than representing transported phenocrysts. This requires the host units to represent dynamic conduits in which olivine crystallized and accumulated (Leshner et al., 1984; Leshner, 1989; see review by Arndt et al., 2008).

The scatter of Cs-Rb-K-Na and Ba-Sr-Ca (**Fig. 27**) in most peridotites and many pyroxenites suggests that they have been mobile during serpentinization. In contrast, the well-defined negative correlations between Mg and Ti-Al-Si (**Fig. 26**) suggest that they have been relatively immobile, which is consistent with evaluations of alteration in other greenschist facies komatiitic rocks (see reviews by Leshner and Stone, 1996; Arndt et al., 2008). The presence of multiple cumulate phases (Ol-Opx, Ol-Cpx, Ol-Sul) and variable amounts of trapped silicate liquid hamper evaluations of the mobility of Si-Mg-Fe-Mn, but by analogy with studies of other serpentinized but texturally well-preserved komatiitic rocks we can assume that they have been only slightly mobile (e.g., Leshner and Stone, 1996; Arndt et al., 2008).

9.2.4 Late Pyroxenite

The barren late pyroxenite phase that disrupted the net-textured mineralization in the Eagle's Nest Dike is similar, but more olivine rich than the barren late websterite phase that invaded the lower part of the Black Thor intrusion, including the Black Label Cr deposit (Spath et al., 2015; Spath, 2017). Establishing the composition of the magma it crystallized from is hampered by the cumulate nature of the pyroxenite, the absence of unaltered Opx, and the paucity of unaltered Cpx, but the lower abundance of olivine (**Fig. 6**) indicates that it was less magnesian and more silica rich than the magma from which the peridotites in the Eagle's Nest dike and Double Eagle intrusion crystallized.

9.3 Sulfide-Silicate Contacts

The textural relationships between silicate minerals and sulfides at Eagle's Nest provide insights into the genetic and temporal relationships between silicates and sulfides. Olivine exhibits subhedral crystal forms and could not have crystallized from a sulfide liquid, suggesting that olivine crystallized first and was later infiltrated by sulfide melt. There are abundant clasts of olivine cumulate in inclusion net-textured sulfides with sulfide in between and 'breaking' up individual olivine (**Fig. 12**), suggesting that these also formed before sulfides. Sulfides sometimes cross-cut olivine, but in most if not all cases these appear to be sulfides mobilized into or replacing magnetite in fractures generated during serpentinization of olivine. There are rare occurrences of pockets of sulfide in olivine crystals, this may be attributed to remobilized sulfide exploiting serpentinizing fractures in olivine, or may be a result of sulfide adjacent to olivine being cut so some sulfide is left on the olivine surface, appearing to be inside the olivine.

The abundance of olivine \pm sulfide cumulate rocks in the Eagle's Nest dike requires that olivine and molten sulfide 1) crystallized/exsolved and accumulated together in the dike during emplacement without physical segregation from one another, or that 2) one or both were physically transported into and accumulated in the dike independently of one another and subsequently mixed. The former is unlikely because olivine and sulfide crystallize/exsolve along a cotectic, forming rocks containing $\sim 60\times$ more olivine than sulfide (e.g., Duke, 1986; Barnes, 2007). The latter is more likely, but the relative transportability of less dense olivine and denser sulfide melt droplets depend on their sizes (or effective sizes in the case of slugs or pseudoslugs), the density, viscosity, and velocity of the magma (e.g., Leshner and Groves, 1986; de Bremond d'Ars et al., 2001; Robertson et al., 2015), and the orientation of transport (e.g., Leshner, 2017, 2019). Coarser olivine and finer sulfide can be transported together but they would be expected to become segregated from one another if not hydrodynamically equivalent.

The presence of a well-defined massive\net\disseminated sulfide segregation profile in the upper embayment and a comparatively irregular distribution of net and massive sulfide in the lower embayment may be explained by Eagle's Nest being emplaced at a shallow angle. The upper embayment could represent a less dynamic area in front or behind the topographical high where ore could undergo gravitational segregations, while the lower embayment may represent a more dynamic area further away from the topographical high; however, complex fluid dynamic studies are beyond the scope of this thesis.

9.4 Sulfur Source

The S isotopic compositions of Eagle's Nest ores (**Fig. 38**) are consistent with the S being derived from 1) a mantle-derived magma, 2) an unfractionated crustal source such as the iron formation in the country rocks, or 3) some combination of the two. The much smaller variations in the strongly-mineralized Eagle's Nest Dike and the much greater variations in the weakly mineralized Black Thor intrusion are not consistent with a control by the relative masses of magma and sulfide (see Leshner and Burnham, 2001; Ripley, 2017), suggesting multiple isotopically different crustal sources.

The amount of sulfide in the Eagle's Nest dike, which is estimated to be ~11% (weighted bulk sulfide content calculated from S data for mineralized and barren rocks in the Noront database), is 35x greater than the ~0.3% S that can dissolve in a komatiitic liquid (e.g., Shima and Naldrett, 1975; Li and Ripley 2009; Fortin et al. 2015; Smythe et al. 2017). Although solubility is reduced by cooling and/or contamination (see review by Naldrett, 2004), those processes would induce crystallization of 60-100x more olivine than sulfide (Duke, 1986; Barnes, 2007), resulting in disseminated not net-textured mineralization. This suggests that Fe-Ni-Cu sulfides at Eagle's Nest formed by partial melting of a S-rich horizon and that immiscible sulfides were left behind in the dike (as inferred for Thompson: Leshner et al., 2001; Expo-Ungava: Mungall: 2007) or that they were transported into their current location from "upstream" in the magmatic plumbing system (as inferred for Kambalda: Leshner and Campbell, 1993; Raglan: Leshner, 2007). Given the abundance of sulfide in the Eagle's Nest dike, the latter process seems more likely, although we cannot discount a contribution by the former process.

Though many models for the genesis of Ni-Cu-(PGE) deposits involve upward transport (e.g., Lightfoot and Evans-Lamswood, 2015; Robertson et al., 2016), Leshner (2017, 2019) has argued that most sulfides do not appear to have been transported vertically and that most appear to have formed at more-or-less the same stratigraphic level that they are localized. This is consistent with the inferred subhorizontal orientation of the Eagle's Nest dike and the presence of some sulfide-bearing lithologies at the same stratigraphic level in the McFaulds Lake greenstone belt.

9.5 Sulfide Geochemical Variations

The distribution of S contents in the Noront assay database, indicates that the majority of the samples are subeconomic rocks with <2% S and <5 wt% sulfide and net-textured ores with 5.9-12.5% S and 15-35 wt% sulfide. The maximum amount of sulfide in Eagle's Nest net-textured mineralization is much less than what is observed at Alexo (up to 50%: Houlé et al., 2012), Jinchuan (up to 35%: deWaal et al., 2004; Tonnelier, 2010), Kambalda (up to 60%: Ewers and Hudson, 1972), and Raglan (up to 70%: Leshner, 2007). The reason for Eagle's Nest net-textured sulfides not extending to higher sulfide contents appears to be related to the olivine being packed more tightly than in other deposits.

The paucity of mineralization containing 35-50 wt% sulfide at Eagle's Nest is similar to Jinchuan (e.g., deWaal et al., 2004) but different from many other deposits (e.g., Kambalda, Pechenga, Raglan, Thompson). The greater abundance of massive and semi-massive sulfide mineralization at the latter deposits is consistent with the sulfide having formed early, prior to accumulation of the majority of the olivine in the host units, whereas the lower abundance of massive and semi-massive sulfide mineralization at Eagle's Nest and Jinchuan is consistent with the sulfide melt

having been introduced later, allowing it to accumulate with and infiltrate olivine (see section 9.6, below).

The positive correlations between Fe-Ni and S (**Fig. 30**) confirm that these minerals are housed in sulfides. Cu correlates less well, which is the case in many Ni-Cu-PGE deposits. The weaker correlation between Pd and S is consistent with the majority of the Pd being housed in sulfides or exsolved from phases associated with sulfides, with the remainder in platinum-group minerals. The scatter of Au-Pt-Ag are most likely attributed to them being housed in platinum-group minerals or alloys and heterogeneously distributed on the scale larger than the analyzed samples. The greater variation of Pd compared to Pt may represent a greater mobility of Pd in magmatic/metamorphic hydrothermal fluids than Pt, which have different solubilities in S-rich and Cl-rich fluids (see review by Hanley, 2005).

The lower Ca content of leopard net texture (~0.1-0.25%) relative to the other net textures (~0.30-2.75%) reflects the greater abundance of olivine and lower abundance of Cpx, permitting this texture to be identified from other net textures geochemically. The negative correlation between MgO and both Al₂O₃ and CaO (**Fig. 26**) is an indicator that where more magnesian-rich (olivine) rocks exist, fewer less primitive (CaO-altered pyroxenes) and non-ultramafic/mafic (Al₂O₃) rocks exist.

The very similar Ni tenors (**Fig. 34A-B**) across all textures indicate that all of the sulfide equilibrated with magmas of similar compositions at similar magma:sulfide:olivine ratios (see Lesher and Burnham, 2001). The slight differences in Cu tenors (**Figs. 34C-D**) indicate that mobilization of chalcopyrite has a moderate impact on tenors. The fact that massive sulfide contains the most pentlandite but similar chalcopyrite to semi-massive sulfide is an indicator that pentlandite is significantly less mobile than chalcopyrite, and that late stage veins may be Cu fractionates of massive sulfide. The negative correlation between Ni₁₀₀ and Cu₁₀₀ (**Fig. 35**) indicates that the more Ni-rich the sulfide is, the less Cu it contains.

The Ni-Cu-(PGE) mantle-normalized metal abundances indicate magmatic enrichment and contamination in all presented metals (**Fig. 36**; Pd-Cu-Pt-Rh-Ru-Ni-Ir-Os-Co), with massive and semi-massive sulfide at Eagle's Nest containing equal to or higher values than Kambalda and Raglan.

9.6 Net-Textured Sulfide Genesis

Although massive sulfide and disseminated sulfide are present in Eagle's Nest, the sub-species of net-textured sulfide, particularly those not seen in other deposits, require a more in-depth analysis. There are several existing models for the generation of net-textured sulfides as a whole:

- 1) The 'billiard ball' model of Naldrett (1966) attributes the formation of net texture to static gravitational segregation (from base to top) of dense sulfide melt (analogous to mercury), closely-packed olivine with interstitial sulfide melt (analogous to closely-packed billiard balls with interstitial mercury), and olivine and interstitial silicate melt with disseminated sulfides trapped between olivine crystals (analogous to billiard balls + water ± mercury). This model was modified by Usselman et al. (1979) to allow for the solidification of the lower layer of massive sulfide melt in situations where the overlying column of olivine was too thick to preserve any massive sulfide. It may apply to Kambalda and other ore bodies with simple massive/net\disseminated ore profiles, but cannot explain the more complex ore profiles at

Alexo or Raglan where the ore profiles are much more complex (Houlé et al., 2012; Leshner, 2017).

- 2) The flow segregation model of (Hudson, 1972) attributes the formation of net texture to dynamic gravitational segregation of massive sulfide melt, olivine + sulfide melt, and olivine + silicate melt ± small sulfide droplets during lava/magma emplacement. It may also apply at Kambalda and other ore bodies with simple massive\net\disseminated ore profiles, and it may also explain some of the more complex ore profiles at Alexo or Raglan as multiple pulses.
- 3) The gravity percolation model of Barnes et al. (2016) attributes the formation of net texture to downward migration of denser sulfide melt through a network of closely-packed olivine, where the degree of migration is controlled by the size of the sulfide droplets, the size of the pore spaces between olivine crystals, and the ability of sulfide melt to displace the silicate melt (see Mungall and Su, 2005; Chung and Mungall, 2009).

All three models are consistent with the broadly upward segregation of discontinuous massive\net-textured\disseminated mineralization at Eagle's Nest, but none can explain i) the bimodal olivine crystals/clasts in leopard-net-textured sulfides, ii) the different aggregate and xenolith populations in the different sulfide textures (leopard net-textured versus inclusion net-textured versus Disseminated sulfides), or iii) the transgressive nature of disrupted net-textured sulfides.

Leopard-net texture contains fine-grained subhedral olivine phenocrysts and coarse-grained ellipsoidal serpentized olivine-(chromite) aggregates. Similar aggregates are present at Sakatti (Brownscombe et al., 2015) and Nova (Maier et al., 2016) and their origin is not well understood. The difference in the mineralogy of the phenocrysts and aggregates at Eagle's Nest suggests that the former crystallized from a higher-Mg magma that was saturated only in olivine, whereas the latter crystallized from a lower-Mg magma that was saturated in olivine and chromite (see Murck and Campbell, 1993, Barnes, 1998). The weak alignment and more-or-less even distribution of the olivine-rich aggregates suggest that they nucleated more-or-less homogeneously and crystallized in situ, much as pyroxene oikocrysts have crystallized in other types of leopard net- and pinto net-textured sulfides (Barnes et al., 2017). Why olivine would nucleate homogeneously to form the aggregates rather than crystallizing as overgrowths on pre-existing fine-grained olivine phenocrysts is not clear, but may relate to the latter being subhedral phenocrysts that may have undergone some degree of abrasion and/or dissolution during transport, retarding topotactic overgrowth in favour of growth of the aggregate (see discussion by Holness and Vernon, 2015). The absence of sulfides (other than late-stage veinlets formed during serpentization) inside the phenocrysts or aggregates suggests that the sulfides percolated into the olivine crystal network after they accumulated.

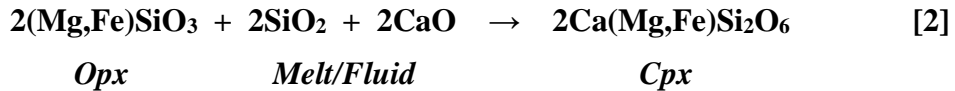
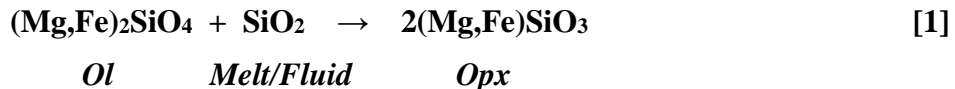
Pinto net-textured sulfide, containing a network of olivine net-textured sulfide with large talc-altered Opx oikocrysts, appears to have formed from a more siliceous magma (see review of phase equilibria in Arndt et al., 2008). Because this texture is uncommon and is sporadically distributed, it may reflect incomplete homogenization of contaminants (see discussion by Leshner and Arndt, 1995) rather than an influx of a distinct more-contaminated magma pulse.

Inclusion net-textured sulfide contains more sporadic and less evenly distributed coarse, ellipsoidal peridotite and pyroxenite anteliths. These were likely incorporated "upstream" in the plumbing system. Subsequent sulfide infiltration of the anteliths may have caused some smaller olivine cumulate fragments to break off and be preserved in the net-textured sulfide surrounding the anteliths (**Figs. 22E-F**).

Patchy net-textured sulfide may represent localized ‘transition’ zones between barren peridotite and more common leopard net-textured sulfide. Because olivine is tightly packed throughout patchy net-textured samples, this implies a mechanical explanation for the patchiness of the sulfide.

Disrupted net-textured sulfide contains patches of leopard-net-textured mineralization with cross-cutting barren pyroxenite (**Fig. 16**). The diffuse, irregular contacts suggest that the pyroxenite was emplaced before the net-textured mineralization had solidified, and the preservation of relict igneous olivine in the barren pyroxenite suggests that it was refractory. The absence of sulfide in the pyroxenite or additional sulfide adjacent to the pyroxenite suggests that it was dissolved. The restriction of disrupted net-textured mineralization to the central parts of the dike, not the upper or lower parts, suggests that this part of the dike was rheologically more susceptible to being intruded.

The nature of the invading phase and the mechanism of replacement of net-textured mineralization are not clear, but the process appears to have involved reactions of the form:



and dissolution of sulfides. It may have involved one or more of the following processes:

- 1) Reaction with an internally- or externally-derived supercritical Si-Ca-rich fluid phase, as proposed by Barnes et al. (2016) for similar rocks at the Ntaka deposit in Tanzania. Such a process is consistent with the highly irregular contacts and gradational nature of the pyroxenite zones that have invaded leopard-net-textured sulfides, but this model does not explain the restriction of the transgressive pyroxenite zones to net-textured sulfide zones.
- 2) Reaction with an internally-derived residual silicate melt. This process is supported by the presence of rare barren pyroxenite cross-cutting barren peridotite, but it is not clear whether an internally-derived residual liquid would be out of equilibrium enough to replace silicates and sulfides.
- 3) Reaction with an externally-derived but petrogenetically related silicate melt, similar to the process proposed by Spath (2017) for more Opx ± Chr-rich rocks in the AT-12 keel of the Black Thor intrusion. Evidence for this includes the large scale (up to 40 cm) of some of the transgressive pyroxenite (**Fig. 16**) and the preservation of relict igneous olivine in disrupted-net-textured mineralization, which is consistent with it being refractory during emplacement of the pyroxenite.

9.7 Evolution and Genesis of the Eagle’s Nest Deposit

The above constraints suggest that the emplacement and crystallization of the Eagle’s Nest dike and the formation of the Ni-Cu-(PGE) mineralization occurred as follows (**Fig. 39**):

T0 (not shown): Generation of sulfide-undersaturated high-Mg komatiitic magma, most likely related to a mantle plume (see e.g., Sproule et al., 2002; Herzberg et al., 2007) and ascent near the

southern margin of the North Caribou Superterrane, possibly related to rifting along that margin. (Stott et al., 2010; Mungall, 2013; Houlé et al., 2020).

T1: Intrusion of the first pulse of komatiitic magma, as a blade-shaped dike below the contact between less dense underlying granitoids and overlying more-dense mafic-dominated volcanic rocks, forming barren olivine-poor margins.

T2: Deposition of olivine phenocrysts and/or olivine primocrysts through *in situ* fractional accumulation (e.g., Leshner, 1989) forming a network of ortho to mesocumulate olivine (65-85% Ol, 15-35% silicate melt) and minor anteliths/xenoliths.

T3: Incorporation of S-rich country rock, probably from footwall iron formations “upstream” from the dike, and generation of immiscible Fe-(Cu) sulfide xenomelts that were upgraded to Fe-Ni-Cu sulfide melts during transport.

T4: Deposition of sulfide melts onto the network of cumulus olivine, displacing less-dense silicate melts, forming leopard net-textured mineralization along the length of the dike.

T5: Density-driven segregation of massive sulfide melts into embayments along the base of the dike, which formed during intrusion, but were likely enlarged by thermomechanical erosion by sulfides (Groves et al., 1986; Williams et al., 1998).

T6: Deposition of additional sulfide (waning of system) to form disseminated sulfides and patchy-net textured sulfides along the length of the dike.

T7: Invasion of the dike by one or more pulses of pyroxenite melt and/or Si-Ca rich fluid, generating disrupted-net texture.

T8: Crystallization of MSS and mobilization of residual sulfide melt (now represented by chalcopyrite) to form cross-cutting veins of massive sulfide that transgress other mineralized zones.

T9: Waning magmatism, cooling, and solidification of the Eagle’s Nest bladed dike, followed by serpentinization of olivine.

T10: Burial, deformation (rotation, faulting, local shearing), metamorphism to greenschist facies, and metasomatism by CO₂-rich fluids producing local talc-carbonate alteration of the host rocks.

If this model is correct, then the different inclusion populations imply changes in accessibility of sources for inclusions: early Ol aggregates in leopard net and peridotite-dunite anteliths in inclusion net, followed by no inclusions in patchy net, followed by chromitite anteliths in disseminated.

9.8 Implications for Exploration, Mining, and Beneficiation

The following are the major implications for exploration, mining, and beneficiation:

- 1) Additional drilling, geophysical surveys, and structural studies would aid in confirming the lack or presence of a connection between Eagle’s Nest and the rest of the Esker Intrusive Complex.
- 2) The irregular massive sulfide mineralization along the footwall contact will require more detailed drilling to define more clearly.
- 3) The predominance of net-texture in the deposit will aid in designing an efficient beneficiation process.

- 4) Disrupted-net texture will dilute the grade to a certain degree, but should not affect beneficiation.
- 5) The majority of pentlandite is >3-5 mm, which should aid in beneficiation.
- 6) The low Ni contents (0.4-0.09%) in pyrrhotite means that monoclinic pyrrhotite can be removed magnetically without significant Ni loss.

10 Conclusions

- 1) The Eagle's Nest Ni-Cu-PGE deposit is hosted by a subvertical blade-shaped dike, which appears to have been emplaced subhorizontally and rotated 90 degrees to the SE along with the overlying Double Eagle intrusion (in the resulting geometry, the SE portion is the top of the dike)
- 2) Most of the rocks were hydrated and locally carbonated during greenschist facies metamorphism, but they are only locally penetratively deformed, preserving a wide range of igneous textures.
- 3) The barren ultramafic rocks and the silicate components of the mineralized rocks are mainly lherzolite and Ol websterite with lesser wehrlite and harzburgite, and rare dunite. Relict igneous olivine compositions range Fo₈₄₋₈₆, but the MgO compositions of Eagle's Nest cumulate rocks suggest that the silicate component of the mineralized rocks formed from a more magnesian-rich olivine, which was not found during this study.
- 4) The S isotope compositions at Eagle's Nest are consistent with a S source derived from a mantle-derived magma, local iron formation in country rocks, or both. The very narrow variations of S-isotope data at Eagle's Nest compared the larger variations in smaller Ni-Cu-(PGE) occurrences in the Black Thor intrusion are consistent with it being a more dynamic system in which multiple isotopically distinct S sources (represented by the wider ranges in analyzed country rocks and smaller showings in the Black Thor part of the system) were homogenized.
- 5) The ore body is zoned NW to SE (i.e. bottom to top) from discontinuous massive and semi-massive sulfides, a dearth of sulfides in the 35-60 wt% sulfide range, and then through net-textured sulfides to disseminated sulfides, consistent with gravitational segregation in the original orientation.
- 6) Net-textured sulfide facies contains five subfacies: a more-or-less continuous zone of leopard-net-textured sulfide subfacies containing discontinuous zones of inclusion net-, pinto net-, patchy net-, and disrupted net-textured subfacies.
- 7) The Eagle's Nest dike appears to represent a dynamic magmatic conduit. The ores and host rocks appear to have formed from at least three distinct magma pulses:
 - a) The first pulse was a moderate- to high-Mg komatiitic magma that was sulfide undersaturated and crystallized the sulfide free units lherzolite, harzburgite, wehrlite), which are preserved discontinuously along the NW margin and continuously along the SE margin.
 - b) The second phase was a variably high- to moderate-Mg komatiitic magma that was sulfide saturated and appears to have carried olivine phenocrysts and Fe-Ni-Cu sulfide droplets. After local segregation of MSS and residual sulfide liquid, all of the mineralization – regardless of texture or location in the system – has similar metal tenors and ³²S/³⁴S isotope ratios, so was likely emplaced in several semi-continuous magmatic events. Each contained different inclusion types and/or formed different aggregate/oikocryst types: gabbro xenoliths and peridotite anteliths in massive sulfide facies, coarse olivine aggregates in

leopard net-textured sulfide subfacies, Opx oikocrysts in pinto net-textured sulfide subfacies, peridotite and smaller olivine aggregates/inclusions and Cpx oikocrysts in inclusion net-textured sulfide subfacies, and chromitite inclusions in disseminated sulfide facies.

- c) The third phase was a sulfide-undersaturated low-Mg komatiitic magma – similar to that present in the feeder and lower part of the Black Thor intrusion – that locally disturbed mainly the net-textured sulfides producing the disrupted net-textured subfacies.
- 8) The Eagle’s Nest dike contains mainly cumulate rocks and appears to have lost most of the residual magma to unexposed or unpreserved intrusions or volcanic rocks. It contains small chromitite anteliths/xenoliths, but does not appear to have been the feeder to the overlying chromite-rich, sulfide-poor Double Eagle intrusion.
- 9) The Eagle’s Nest Ni-Cu-(PGE) deposit contains the widest range of net-textured sulfide subfacies reported thus far, allowing for insight into the genesis of net-textured sulfides as a whole, making it one of the best places in the world to study textures of this type.

11 Acknowledgements

We are very grateful to Alan Coutts and Ryan Weston for logistical support; Ryan Weston, Matt Deller, and Geoff Heggie for insights and discussions during core logging; Cory Exell, Rob Lyght, Tristan Megan, and Roydon Spence for assistance during core pulling and core layout and the rest of the Esker Camp crew for their hospitality; Dave Crabtree and Sandra Clarke assistance with the SEM and EMPA analyses; Ed Ripley for assistance with the S isotope analyses; and Pedro Jugo for insightful discussions. The project was supported by the Targeted Geoscience Initiative 5 program of the Geological Survey of Canada, a NSERC-Cliffs/Noront CRD grant (446109-12) and a NSERC-Discovery grant (203171-2012) to CML, and a GSC Research Affiliate Program award to Natascia Zuccarelli. Scientific inputs from Charley Duran (IOG) and Wouter Bleeker (GSC) on early version have greatly helped to improve this contribution.

12 References

- Arndt, N.T., Leshar, C.M., and Barnes, S.J., 2008. Komatiite. Cambridge: Cambridge University Press (Cambridge, UK), 488 pp.
- Azar, B., 2010. The Blackbird chromite deposit, James Bay Lowlands of Ontario, Canada: implications for chromitite genesis in ultramafic conduits and open magmatic systems. Unpublished MSc thesis, University of Toronto (Toronto, Canada), 154 pp.
- Barnes, S.-J. and Lightfoot, P.C., 2005. Formation of magmatic nickel-sulfide ore deposits and processes affecting their copper and platinum-group element contents. In Hedenquist, J.W., Thompson, J.F.H., Goldfarb, R.J. and Richards, J.P. (eds.) Economic Geology 100th Anniversary Volume, p. 179-213.
- Barnes, S.J., 1986. The effect of trapped liquid crystallization on cumulus mineral compositions in layered intrusions. *Contributions to Mineralogy and Petrology*, v. 93, p. 524–531
- Barnes, S.J., 1998. Chromite in Komatiites, 1. Magmatic controls on crystallization and composition. *Journal of Petrology*, 39(10), 1689-1720.

- Barnes, S.J., 2007. Cotectic precipitation of olivine and sulfide liquid from komatiite magma and the origin of komatiite-hosted disseminated nickel sulfide mineralization at Mount Keith and Yakabindie, Western Australia. *Economic Geology*, v.102, p. 299-304
- Barnes, S.J. and Mungall, J.E., 2018. Blade-shaped dikes and nickel sulfide deposits: a model for the emplacement of ore-bearing small intrusions. *Economic Geology*, v.113 (3), p. 789–798.
- Barnes, S.J., Staude, S., Le Vaillant, M., Pina, R., and Lightfoot, P.C., 2018. Sulfide-Silicate textures in magmatic Ni-Cu-PGE sulfide ore deposits: Massive, semi-massive and sulfide matrix breccia ores. *Ore Geology Reviews*, v.101, p. 629-651
- Barnes, S.J., and Robertson, J.C., 2019. Time scales and length scales in magma flow pathways and the origin of magmatic Ni–Cu–PGE ore deposits. *Geoscience Frontiers*, v.10 (1), p. 77-87.
- Barnes, S.J., Cruden, A.R., Arndt, N, and Samur, B.M., 2016. The mineral system approach applied to magmatic Ni-Cu-PGE sulphide deposits. *Ore Geology Reviews*, v.76, pp. 296-316
- Barnes, S.J., Leshner, C.M., and Keays, R.R., 1995. Geochemistry of mineralised and barren komatiites from the Perseverance nickel deposit, Western Australia. *Lithos*, v. 34, p. 209-234
- Barnes, S.J., Mungall, J.E., Le Vaillant, M.L., Godel, B., Leshner, C.M., Holwell, D.M., Lightfoot, P.C., Krivolutszkaya, N., and Wei, B., 2017. Sulfide-silicate textures in magmatic Ni-Cu-(PGE) sulfide ore deposits: Disseminated and net-textured ores. *American Mineralogist*, v. 102, p. 473–506.
- Barnes, S. J., Taranovic, V., Miller, J. M., Boyce, G., Beresford, S. W., 2020, Sulfide emplacement and migration in the Nova-Bollinger Ni-Cu-Co deposit, Albany-Fraser Orogen, Western Australia: *Economic Geology*, in press.
- Bazilevskaya, E., 2009. Primary and Secondary Textures of Fe-Ni-Cu sulfide mineralization in the Kattiniq member of the Raglan Formation, Cape Smith Belt, New Quebec; M.Sc. thesis, Laurentian University, Sudbury, 59 pp.
- Bolchover, P. and Lister, J.R., 1999. The effect of solidification on fluid-driven fracture, with application to bladed dykes. *Proceedings of the Royal Society of London. Series A: Mathematical, Physical and Engineering Sciences*, v. 455(1987), p.2389-2409.
- Brownscombe, W., Ihlenfeld, C., Coppard, J., Hartshorne, C., Klatt, S., Siikaluoma, J.K. and Herrington, R.J., 2015. The Sakatti Cu-Ni-PGE sulfide deposit in northern Finland. In *Mineral Deposits of Finland* (p. 211-252). Elsevier.
- Burnham, O.M., Hechler, J.H., Semenyna, L. and Schweyer, J., 2002. Mineralogical controls on the determination of trace elements following mixed acid dissolution. Summary of field work and other activities, p.36-110.
- Burnham, O.M., 2008. Trace element analysis of geological samples by inductively coupled plasma mass spectrometry (ICP-MS) at the Geoscience Laboratories: Revised capabilities due to method improvements. Summary of field work and other activities. Ontario Geological Survey, Open File Report, 6226, p.38-102.

- Campbell, I.H., and Murck, B.W., 1993. Petrology of the G and H chromitite zones in the Mountain View area of the Stillwater Complex, Montana. *Journal of Petrology*, v. 34(2), p.291-316.
- Carson, H.J.E., Leshner, C.M., and Houlié, M.G., 2015. Geochemistry and petrogenesis of the Black Thor intrusive complex and associated chromite mineralization, McFaulds Lake greenstone belt, Ontario: Targeted Geoscience Initiative 4, Geological Survey of Canada, v. 7856, p. 87-102.
- Carson, H.J.E., Leshner, C.M., and Houlié, M.G., PhD in prep. Geochemistry and petrogenesis of the Black Thor intrusive complex and associated chromite mineralization, McFaulds Lake greenstone belt, Ontario. Laurentian University, Sudbury.
- Cawthorn, R.G. and Barry, S.D., 1992. The role of intercumulus residua in the formation of pegmatoid associated with the UG2 chromitite, Bushveld Complex. *Australian Journal of Earth Sciences*, v. 39(3), p.263-276.
- de Bremond d'Ars, J., Arndt, N.T. and Hallot, E., 2001. Analog experimental insights into the formation of magmatic sulfide deposits. *Earth and Planetary Science Letters*, v. 186(3-4), p.371-381.
- De Waal, S.A., Xu, Z., Li, C. and Mouri, H., 2004. Emplacement of viscous mushes in the Jinchuan ultramafic intrusion, western China. *The Canadian Mineralogist*, v. 42(2), p. 371-392.
- Eckstrand, O.R., 1975. The Dumont serpentinite; a model for control of nickeliferous opaque mineral assemblages by alteration reactions in ultramafic rocks. *Economic Geology*, v. 70(1), p.183-201.
- Ewers, W.E. and Hudson, D.R., 1972. An interpretive study of a nickel-iron sulfide ore intersection, Lunnon Shoot, Kambalda, Western Australia. *Economic Geology*, v. 67(8), p.1075-1092.
- Farhangi, N., Leshner, C.M., and Houlié, M.G., 2013. Mineralogy, geochemistry and petrogenesis of nickel-copper-platinum group element mineralization in the Black Thor intrusive complex, McFaulds Lake greenstone belt, Ontario: Ontario Geological Survey, v. 6290, p. 55-1-55-7.
- Farhangi, N. 2020. Mineralogy, Geochemistry, and Genesis of Ni-Cu-PGE Mineralization in Black Thor Igneous Complex, McFaulds Greenstone Belt, ON. Master's Thesis, Sudbury, Ontario, Laurentian University.
- Fortin, M.A., Riddle, J., Desjardins-Langlais, Y. and Baker, D.R., 2015. The effect of water on the sulfur concentration at sulfide saturation (SCSS) in natural melts. *Geochimica et Cosmochimica Acta*, v.160, pp.100-116.
- Gresham, J.J., Loftus-Hills, G.D. 1981. The geology of the Kambalda nickel field, Western Australia. *Economic Geology*, v. 76 (6), p. 1373-1416.
- Groves, D.I., Korzikoski, E.A., McNaughton, N.J., Leshner, C.M., and Cowden, A., 1986. Field evidence for thermal erosion by komatiites at Kambalda, Western Australia and the genesis of nickel ores. *Nature*, v. 319, p. 136-139
- Herzberg, C., Asimow, P.D., Arndt, N.T., Niu, Y., Leshner, C.M., Fitton, J.G., Cheadle, M.J., Saunders, A.D., 2007. Temperatures in ambient mantle and plumes: Constraints from

- basalts, picrites, and komatiites. *Geochemistry, Geophysics, and Geosystems (G³)*, v.8(2), 34 pp.
- Holness, M.B., and Vernon, R.H., 2015. The influence of interfacial energies on igneous microstructures, *in* Charlier, B. et al. (eds.), *Layered Intrusions*, Springer Geology, Dordrecht, p. 183-228.
- Houlé, M.G., and Leshner, C.M., 2011. Komatiite-associated Ni-Cu-(PGE) deposits, Abitibi greenstone belt, Superior Province, Canada. *Reviews in Economic Geology*, v. 17, p. 89-121.
- Houlé, M.G., Leshner, C.M., and Davis, P.C., 2012. Thermomechanical erosion at the Alexo Mine, Abitibi greenstone belt, Ontario: implications for the genesis of komatiite-associated Ni-Cu-(PGE) mineralization. *Mineralium Deposita*, v.47(1), p. 223-229.
- Houlé, M.G., Leshner, C.M., McNicoll, V.J., and Bécu, V., 2017. Ni-Cr Metalloctect: Synthesis, updates, and revised models for the Superior Province; in *Targeted Geoscience Initiative – 2016 Report of Activities*, (ed.) N. Rogers; Geological Survey of Canada, Open File 8199, p. 59-61. <https://doi:10.4095/299573>
- Houlé, M.G., Leshner, C.M., Schetselaar, E., Metsaranta, R.T., and McNicoll, V., 2017, Architecture of magmatic conduits in Cr-(PGE)/Ni-Cu-(PGE) Ore Systems, in Rogers, N., ed., *TGI Phase 5: Ore systems from source to deposit – 2016 Activity Report and Synthesis: Geological Survey of Canada Open File 8199*, p. 55-58.
- Houlé, M.G., Leshner, C.M., Metsaranta, R.T., and Sappin, A.-A., 2019. Architecture of magmatic conduits in chromium-PGE and Ni-Cu-PGE ore systems in Superior Province: example from the ‘Ring of Fire’ region, Ontario; in *Targeted Geoscience Initiative: 2018 report of activities*, (ed.) N. Rogers; Geological Survey of Canada, Open File 8549, p. 441–448. <https://doi.org/10.4095/313678>
- Houlé, M.G., Leshner, C.M., Metsaranta, R.T., Sappin, A.-A., Carson, H.E.J., Schetselaar, E.M., Laudadio, A., 2020. Magmatic architecture of the Esker intrusive complex, Ring of Fire Intrusive Suite, McFaulds Lake greenstone belt, Superior Province, Ontario: Implications for the genesis of Cr and Ni-Cu-(PGE) mineralization in an inflationary dyke-chonolith-sill complex; in *Targeted Geoscience Initiative 5: Advances in the understanding of Canadian Ni-Cu-PGE and Cr ore systems – Examples from the Midcontinent Rift, the Circum-Superior Belt, the Archean Superior Province, and Cordilleran Alaskan-type intrusions*, (ed.) W. Bleeker and M.G. Houlé; Geological Survey of Canada, Open File 8722
- Hudson, D.R., 1972. Evaluation of genetic models for Australian sulphide nickel deposits: Australasian Institute of Mining and Metallurgy Conference, Newcastle, p. 59-68.
- Huminicki, M.A.E., 2004. Geology, mineralogy, and geochemistry of the Kelly Lake nickel-copper-platinum group element deposit, Sudbury, Ontario. MSc Thesis, Laurentian University, Sudbury, Ontario.
- Keating, G.L. and Burnham, O.M., 2012. Revision of the calibration for major element analysis of geological samples by wavelength dispersive X-ray fluorescence at the Geoscience Laboratories. summary of field work and other activities. Ontario Geological Survey, Open File Report, 6280, p.39-102.

- Laarman, J., 2014. PhD thesis, A detailed metallogenetic study of the McFaulds Lake chromite deposits, northern Ontario, Western University, 530 pp.
- Latypov, R.M., 2002. Phase equilibria constraints on relations of ore-bearing intrusions with flood basalts in the Noril'sk region, Russia. *Contributions to Mineralogy and Petrology*, v. 143(4), p.438-449.
- Laudadio, A., 2019. 3D Geological Modeling of the Double Eagle–Black Thor Intrusive Complexes, McFaulds Lake Greenstone Belt, Ontario, Canada; Unpublished M.Sc. thesis, Carleton University, Ottawa, Canada, 107 p.
- Leshner, C.M., 1989. Komatiite-associated nickel sulfide deposits. Chapter 5 in Whitney JA and Naldrett, A.J. (Editors), *Ore Deposition Associated with Magmas, Reviews in Economic Geology* v. 4, Economic Geology Publishing Company, El Paso, p. 45-101.
- Leshner, C.M., 2007. Ni-Cu-(PGE) Deposits in the Raglan Area, Cape Smith Belt, New Québec, in Goodfellow, W.D. (Editor), *Mineral Resources of Canada: A Synthesis of Major Deposit-types, District Metallogeny, the Evolution of Geological Provinces, and Exploration Methods*, Geological Survey of Canada and Mineral Deposits Division of the Geological Association of Canada Special Publication 5, p. 351-386.
- Leshner, C.M., 2017. Roles of residues/skarns, xenoliths, xenocrysts, xenomelts, and xenovolatiles in the genesis, transport, and localization of magmatic Fe-Ni-Cu-(PGE) sulfides and chromite. *Ore Geology Reviews*, v. 90, p. 465-484.
- Leshner, C.M., 2019. Up, down, or sideways: Emplacement of magmatic Ni-Cu ± PGE sulfide melts in Large Igneous Provinces, *Canadian J Earth Sciences (Special Issue on Large Igneous Provinces)*, v. 56(7), p. 756-773.
- Leshner, C.M., and Barnes, S.J., 2009. Komatiite-Associated Ni-Cu-(PGE) Deposits, *in* C Li and EM Ripley (Editors), *Magmatic Ni-Cu-PGE Deposits: Genetic Models and Exploration*, Geological Publishing House of China, p. 27-101.
- Leshner, C.M., and Campbell, I.H. 1993. Geochemical and fluid dynamic modelling of compositional variations in Archean komatiite-hosted nickel sulfide ores in Western Australia. *Economic Geology*, v. 88 (4), p.804-816.
- Leshner, C.M., and Groves. D.I., 1986. Controls on the formation of komatiite-associated nickel-copper sulfide deposits, *in* Friedrich, G., Genkin, A.D., Naldrett, A.J., Ridge J.D., Sillitoe, R.H., Vokes, F.M. (Editors), *Geology and Metallogeny of Copper Deposits*. Springer-Verlag, Heidelberg, p. 43-62.
- Leshner, C.M., and Keays, R.R., 2002. Komatiite-associated Ni-Cu-(PGE) deposits: geology, mineralogy, geochemistry and genesis. In *The Geology, Geochemistry Mineralogy and Mineral Beneficiation of Platinum Group Elements*. Edited by L.J. Cabri. Canadian Institute of Mining Metallurgy and Petroleum Special Volume 54, p. 579-617.
- Leshner, C.M., and Stone, W.E., 1996. Exploration geochemistry of komatiites, in Wyman D (Editor), *Igneous Trace Element Geochemistry: Applications for Massive Sulphide Exploration*, Geological Association of Canada, Short Course Notes 12, p. 153-204.

- Leshner, C.M., Arndt, N.T. and Groves, D.I., 1984. Genesis of komatiite-associated nickel sulphide deposits at Kambalda, Western Australia: A distal volcanic model. In Nickel sulphide field conference, p.70-80.
- Leshner, C.M., Burnham, M.O., Keays, R., Barnes, S.J., & Hulbert, L., 2001. Trace-element geochemistry and petrogenesis of barren and ore-associated komatiites. *The Canadian Mineralogist*, v. 39, p. 673-696.
- Li, C. and Ripley, E.M., 2009. Sulfur contents at sulfide-liquid or anhydrite saturation in silicate melts: empirical equations and example applications. *Economic Geology*, v. 104(3), p.405-412.
- Lightfoot, P.C. and Evans-Lamswood, D., 2015. Structural controls on the primary distribution of mafic-ultramafic intrusions containing Ni-Cu-Co-(PGE) sulfide mineralization in the roots of large igneous provinces. *Ore Geology Reviews*, v. 64, p.354-386.
- Maier, W.D., Roberts, M.P., Kiddie, O., Kirkland, C.L., Barnes, S.J., Spaggiari, C.V. and Smithies, R.H., 2016. The Evolution of Mafic and Ultramafic Rocks of the Mesoproterozoic Fraser Zone, Albany-Fraser Orogen, and Implications for Ni-Cu Sulphide Potential of the Region. Geological Survey of Western Australia, p. 1-49.
- McKevitt, D., Leshner, C.M. and Houlié, M.G., 2019. Anatomy of the Ni-Cu-(PGE) mineralized Expo-Raglan magmatic system in the Early Proterozoic Cape Smith belt, Quebec, Canada. GAC-MAC-IAH, Québec 2019.
- Metsaranta, R.T., and Houlié, M.G., 2017. Precambrian geology of the McFaulds Lake area, “Ring of Fire” region, Ontario— central sheet: Ontario Geological Survey, Preliminary Map P .3805; Geological Survey of Canada, Open File 8201.
- Metsaranta, R.T., Houlié, M.G., McNicoll, V.J., and Kamo, S.L., 2015, Revised geological framework for the McFaulds Lake greenstone belt, Ontario: Targeted Geoscience Initiative4, Geological Survey of Canada, v. 7856, p. 61-73.
- Mungall JE, Su, S., 2005. Interfacial tension between magmatic sulfide and silicate liquids: Constraints on kinetics of sulfide liquation and sulfide migration through silicate rocks. *Earth and Planetary Science Letters* v. 234 (1-2), p. 135-149
- Mungall JE, Harvey JD, Balch SJ, Azar B, Atkinson J, Hamilton MA (2010) Eagle’s Nest: A Magmatic Ni-Sulfide Deposit in the James Bay Lowlands, Ontario, Canada. *Society of Economic Geology Special Publication 15*, p. 539-557
- Mungall, J.E., 2007. Crustal contamination of picritic magmas during transport through dikes: the expo intrusive suite, Cape Smith Fold Belt, New Quebec. *Journal Petrology*, v. 48, p. 1021-1039.
- Murck, B.W., and Campbell, I.H., 1986. The effects of temperature, oxygen fugacity, and melt composition on the behavior of chromium in basic and ultrabasic melts. *Geochimica Cosmochimica Acta* v. 50, p.1871-1887.
- Naldrett, A.J., 1966. The role of sulphurization in the genesis of iron-nickel sulphide deposits of the Porcupine District, Ontario. *Canadian Institute of Mining and Metallurgy Transactions* v. 69, p.147-155.

- Naldrett, A.J., 1973. Nickel sulfide deposits-their classification and genesis, with special emphasis on deposits of volcanic association. *CIM Bulletin*, v. 66(739), p.45-63.
- Naldrett, A.J., 2004. *Magmatic Sulfide Deposits: Geology, Geochemistry and Exploration*; Springer-Verlag, Berlin, 727 pp.
- Pearce, J.A., 2008. Geochemical fingerprinting of oceanic basalts with applications to ophiolite classification and the search for Archean oceanic crust. *Lithos*, v. 100(1-4), p.14-48.
- Robertson, J.C., Barnes, S.J. and Le Vaillant, M., 2015. Dynamics of magmatic sulphide droplets during transport in silicate melts and implications for magmatic sulphide ore formation. *Journal of Petrology*, v. 56(12), p.2445-2472.
- Rose, L.A., and Brenan, J.M., 2001. Wetting Properties of Fe-Ni-Co-Cu-O-S melts against olivine: Implications for sulfide melt mobility. *Economic Geology*, v. 96, p. 145–157.
- Rudnick, R.L. and Gao, S., 2003. Composition of the continental crust. *Treatise in Geochemistry*, v. 3, p.1-64.
- Rubin, A.M. and Pollard, D.D., 1987. Origins of blade-like dikes in volcanic rift zones. *US Geological Survey Professional Paper*, v. 1350(2), p.1449-1470.
- Sakai, H., Marais, D., Ueda, A., Moore, J., 1984. Concentrations and isotope ratios of carbon, nitrogen and sulfur in ocean-floor basalts. *Geochimica et Cosmochimica Acta*, v. 48(12), p. 2433–2441.
- Shima, H. and Naldrett, A.J., 1975. Solubility of sulfur in an ultramafic melt and the relevance of the system Fe-SO. *Economic Geology*, v. 70(5), p. 960-967.
- Smythe, D.J., Wood, B.J. and Kiseeva, E.S., 2017. The S content of silicate melts at sulfide saturation: new experiments and a model incorporating the effects of sulfide composition. *American Mineralogist*, v. 102(4), p.795-803.
- Spath III, C.S., Leshner, C.M., and Houlié, M.G., 2015, Hybridized ultramafic rocks in the Black Label hybrid zone of the Black Thor intrusive complex, McFaulds Lake greenstone belt, Ontario: Targeted Geoscience Initiative 4, Geological Survey of Canada, v. 7856, p. 103-114.
- Spath III, C.S., Leshner, C.M., and Houlié, M.G., 2017, *Geology and Genesis of Hybridized Ultramafic Rocks in the Black Label Hybrid Zone of the Black Thor Intrusive Complex, McFaulds Lake Greenstone Belt*. Sudbury, Ontario, Canada. Laurentian University Thesis.
- Sproule, R.A., Leshner, C.M., Ayer, J.A., Thurston, P.C., and Herzberg, C.T., 2002. Spatial and temporal variations in the geochemistry of komatiitic rocks in the Abitibi greenstone belt. *Precambrian Research*, v. 115, p. 153–186.
- Tang, Z., 1993. Genetic model of the Jinchuan nickel-copper deposit, in Kirkham, R.V., Sinclair, W.D., Thorpe, R.I. and Duke, J.M., eds., *Mineral Deposit Modeling: Geological Association of Canada, Special Paper 40*, p. 389-401.
- Taylor, S.R. and McLennan, S.M., 1985. *The continental crust: its composition and evolution*. Blackwell Scientific, London, U.K., 328 pp.
- Tuchscherer, M.G., Hoy, D., Johnson, M., Shinkle, D., Kruze, R., and Holmes, M., 2010. Fall 2008 to winter 2009 Technical drill report on the Black Thor chromite deposit, Black Label

- chromite zone, and associated Ni-Cu-PGEs, McFaulds property (100%), James Bay Lowlands, northern Ontario, Latitude 52°78' N, longitude -86°20' W, Freewest Resources Canada Ltd., unpublished report, 62 pp.
- Usselman, T.M., Hodge, D.S., Naldrett, A.J. and Campbell, I.H., 1979. Physical constraints on the characteristics of nickel-sulfide ore in ultramafic lavas. *The Canadian Mineralogist*, v. 17(2), p. 361–372.
- Williams, D.A., Kerr, R.C., and Leshner, C.M., 1998. Emplacement and erosion by Archean komatiite lava flows: Revisited. *Journal of Geophysical Research*, v. 103(B11), p. 27533-27549.
- Zuccarelli, N., Leshner, C.M., Houlié, M.G., and Weston, R.J., 2017. Sulfide textural variations and multiphase ore emplacement in the Eagle's Nest Ni-Cu-(PGE) deposit, McFauld's Lake greenstone belt, Ontario, Canada; *Proceedings of Mineral Resources to Discover: 14th SGA Biennial Meeting 2017*, v. 2, p. 583–586.
- Zuccarelli, N., Leshner, C.M., and Houlié, M.G., 2018a. Sulphide textural variations and multiphase ore emplacement in the Eagle's Nest Ni-Cu-(PGE) deposit, McFaulds Lake greenstone belt, Ontario; in *Targeted Geoscience Initiative: 2017 report of activities, volume 2*, (ed.) N. Rogers; Geological Survey of Canada, Open File 8373, p. 29–34. <https://doi.org/10.4095/306598>
- Zuccarelli, N., Leshner, C.M., Houlié, M.G., and Weston, R.J., 2018b. Sulfide Textural Variations and Multiphase Ore Emplacement in the Eagle's Nest Ni-Cu-(PGE) Deposit, McFaulds Lake Greenstone Belt, Superior Province, Ontario, Canada. *GSA Annual Meeting 2018: Indianapolis, Indiana*.
- Zuccarelli, N., Leshner, C.M., and Houlié, M.G., 2019. Multiphase ore emplacement in the Eagle's Nest Ni-Cu-(PGE) deposit, McFaulds Lake greenstone belt, Superior Province, northern Ontario, Canada; *GAC-MAC 2019 Annual Meeting; Quebec City, Quebec*.
- Zuccarelli, N., Leshner, C.M., Houlié, M.G., and Barnes, S.J., 2020. Variations in the textural facies of sulphide minerals in the Eagle's Nest Ni-Cu-(PGE) deposit, McFaulds Lake greenstone belt, Superior Province, Ontario: Insights from microbeam scanning energy-dispersive X-ray fluorescence spectrometry; in *Targeted Geoscience Initiative 5: Advances in the understanding of Canadian Ni-Cu-PGE and Cr ore systems – Examples from the Midcontinent Rift, the Circum-Superior Belt, the Archean Superior Province, and Cordilleran Alaskan-type intrusions*, (ed.) W. Bleeker and M.G. Houlié; Geological Survey of Canada, Open File 8722, 15 pp.

13 Figure Captions

Figure 1. Geological map of the McFaulds Lake greenstone belt (modified from Metsaranta and Houlé 2020) showing the main mineral deposits/occurrences, including the Eagle's Nest Ni-Cu-(PGE) deposit within the Esker intrusive complex (dashed rectangle in the middle of the figure). Dashed box indicates the location of Figure 2. MLGB = McFaulds Lake greenstone belt.

Figure 2. Geological map of the Esker intrusive complex showing the location of the main mineral deposits and occurrences (after Houlé et al., 2020). The map has been rotated to illustrate the interpreted magmatic stratigraphy (upward towards the top of the figure). Abbreviations: MLGB = McFaulds Lake greenstone belt. Chromite deposits in black: BB1 = Blackbird 1, BB2 = Blackbird 2, BC = Black Creek, BD = Big Daddy, BH = Black Horse, BL = Black Label, BT = Black Thor. Ni-Cu-(PGE) deposits/occurrences in red: BCZ = Basal Contact Zone, BJ = Blue Jay, BJE = Blue Jay Extension, CBZ = Central Breccia Zone, EN = Eagle's Nest, ET = Eagle Two, EZ = East Zone, NEBZ = northeast Breccia Zone, SWBZ = southwest Breccia Zone.

Figure 3. A: Ore shell of the entire Eagle's Nest deposit (3D model) with Ni (wt %) grades superimposed (Noront Resources, 2020) B: Schematic of a northwest-southeast section (NAD 83, Zone 16, UTM 547219 mE) section through the Eagle's Nest dike showing the sulfide facies and subfacies distributions. Note that the Eagle's Nest deposit occurs along the northwestern edge of the dike. . The location of the section is shown in Figure 2.

Figure 4. Histogram of sulfide contents in the Eagle's Nest deposit based on Noront Resources assays. Sulfide content have been calculated on S wt % content assuming 39% S % in 100% sulfides. See Table 1 for the detailed break-up of the various textural facies.

Figure 5. Images of country rocks below the Esker Intrusive Complex (Carson, in prep.). A: Tonalite below Black Thor intrusion (FN-09-1/222m, #1331699), B: Typical medium- to fine-grained gabbro, referred as the 'Footwall gabbro' that occurs below the Black Thor intrusion (FN-09-1/180.7m, #1331695), C: Banded iron formation below the Black Thor intrusion (FN-09-1/152m, #1331691). All photos from section of NQ core (47.6 mm diameter).

Figure 6. Ternary IUGS classification diagram for ultramafic intrusive rocks showing non-mineralized and mineralized rocks within Eagle's Nest dike. Most of the silicate component of the mineralized units is peridotite.

Figure 7. Scanned images of barren ultramafic host rocks (NQ half core, 4.5 cm wide) and photomicrographs from thin sections (2.5x magnification) of the Eagle's Nest dike. A: Core scan of -grained pyroxenite (NOT-07-029/77.18m), B: Core scan of medium-grained pyroxenite with large orthopyroxene (Opx) crystals (NOT-10-GT04/672m), C: Core scan of fine-grained peridotite with black serpentized olivine (Ol) (NOT-10-076-W1/577.69m), D: Core scan of irregular and irregular contact between very fine-grained peridotite and tonalite (NOT-09-062/595.1m). E-F: Photomicrograph of peridotite (lherzolite) containing relict igneous olivine (Ol), and altered pyroxene (Pxn), plane polarized light (E) and cross-polarized light (F) (NOT-09-053/881.7). G-H:

Photomicrograph of pyroxenite (olivine websterite; pyroxenes replaced by amphiboles), plane polarized light (G) and cross polarized light (H) (NOT-09-062/612.9). Opx = orthopyroxene;

Figure 8. Scanned images of disseminated sulfide (NQ half core, 4.5 cm wide) and photomicrographs from thin sections (2.5x magnification). A: Core scan of disseminated sulfide in small bleb in pyroxenite (NOT-08-030/104.1), B: Core scan of disseminated and minor sulfide between orthopyroxene (Opx) in pyroxenite (NOT-09-049/316), C: Core scan of disseminated Pyrrhotite (Po)-Pentlandite (Pn)-Chalcopyrite (Ccp) and fractionated Po-Pn-Ccp bleb in clinopyroxene (Cpx) and orthopyroxene rich pyroxenite; Opx appears as small (0.5-0.2 cm) light grey round crystals, while Cpx appears as darker grey interstitial material (NOT-09-053-W3/827.7). D-E: Photomicrograph of disseminated sulfide in Ol-pyroxenite, polarized reflected light (D) and cross polarized light (E) (NOT-09-053/ 850), F-G: Photomicrograph of disseminated sulfide in pyroxenite with large chromite (Cr)-magnetite (Mag) cluster, polarized reflected light (F) and cross polarized light (G) (NOT-09-062/608.3).

Figure 9. Disseminated sulfide facies at the Eagle's Nest deposit (drillcore NOT-09-053W3 at 828.17 m, NQ core size). A: A scanned slab showing the typical disseminated sulfide texture within olivine pyroxenite. Black phases are chromite, dark grey phases are olivine, grey phases are pyroxene, and yellowish phases are sulfide. B: μ XRF map, normalized relative concentrations of Ca (blue), Fe (green), and S (red). C: μ XRF map, normalized relative concentrations of Cr (red), Fe (green), and Ca (blue). Chromite-magnetite aggregates in yellow. Abbreviations: Chrt = chromitite, Cpx = clinopyroxene, Ol = olivine, Pxt = pyroxenite, Sul = sulfides.

Figure 10. Scanned images of leopard-net-textured sulfide (NQ half core, 4.5 cm wide) and photomicrographs from thin sections (2.5x magnification). A: Core scan of leopard-net texture containing interstitial sulfide (Sul) between olivine (Ol) in peridotite (NOT-07-017/138.49), B: Core scan of leopard-net texture in peridotite (NOT-07-18/143.5). C-D: Photomicrograph of leopard-net-textured sulfides polarized reflected light (C) and cross-polarized light (D) (NOT-07-028/208.3). E-F: Photomicrograph of leopard-net texture, polarized reflected light (E) and cross-polarized light (F). (NOT-07-018/143.5).

Figure 11. Leopard net-textured sulfide subfacies at Eagle's Nest deposit (drillcore NOT-07-017 at 138.01 m, NQ core size). A: A scanned slab of a typical leopard net-textured sulfide. The black minerals are serpentinized olivine and the yellowish minerals are sulfide minerals. B: μ XRF map with normalized relative concentrations of Ni (red), Cu (green), and S (blue) resulting in olivine appearing as black, chalcopyrite as green, pyrrhotite as blue, and pentlandite as magenta. The black arrow indicates the direction of a weak igneous lamination that is defined by the alignment of the olivine aggregates; the magenta arrow indicates the direction of the weak foliation that is defined by pentlandite±pyrrhotite veinlets. C: μ XRF map with normalized relative concentrations of Cr (red), Fe (green), and Ca (blue) resulting in olivine appearing as red-black, chromite as red, and Fe-bearing sulfides as green. Abbreviations: cg = coarse-grained, fg = fine-grained, vfg = very fine-grained; Ccp = chalcopyrite, Chr = chromite, Fe-Chr = ferrichromite, Ol = olivine, Pn = pentlandite, Po = pyrrhotite.

Figure 12. Scanned images of inclusion-net-textured sulfide (NQ half core, 4.5 cm wide) and photomicrographs from thin sections (2.5x magnification). A: Core scan of inclusion-net texture containing pyroxene (Pxn), and olivine(Ol)-sulfide(Sul) cumulate; includes part of 30 cm long peridotite clast (NOT-07-28/197.1). B-C: Photomicrograph of inclusion-net texture, polarized reflected light (B) and cross-polarized light (C) (NOT-07-028/197.1).

Figure 13. Inclusion net-textured sulfide subfacies at the Eagle's Nest deposit (drillcore NOT-07-028 at 208.97 m, NQ core size). A: A scanned slab of a typical inclusion net-textured sulfide facies rock from the Eagle's Nest deposit. The black minerals are olivine and the yellowish minerals are sulfide. B: μ XRF map with normalized relative concentrations of Ni (red), Cu (green), and S (blue). C: μ XRF map with normalized relative concentrations of Cr (red), Fe (green), and Ca (blue). Red-dashed lines show the approximate limit between pentlandite-pyrrhotite-rich and chalcopyrite-rich domains; the magenta arrow in (b) indicates the orientation of the fine veinlets of pentlandite and pyrrhotite. Abbreviations: Ccp = chalcopyrite, Cpx = clinopyroxene, Ol = olivine, Opx = orthopyroxene, Pn = pentlandite, Po = pyrrhotite.

Figure 14. Scanned images of pinto-net-textured sulfide (NQ half core, 4.5 cm wide) and photomicrographs from thin sections (2.5x magnification). A: Core scan of pinto-net texture with large visible orthopyroxene (Opx) oikocrysts among olivine (Ol) and sulfide (Sul) (NOT-10-076-W1/557.1F). B-C: Photomicrograph of pinto-net texture, polarized reflected light (B) and cross polarized light (C) (NOT-09-071/719.65).

Figure 15. Pinto net-textured sulfide subfacies at the Eagle's Nest deposit (sample NOT-10-076-W1/557.1 m, NQ core size). A: A scanned slab of typical pinto net-textured sulfide. The black minerals are olivine, grey minerals are pyroxene, and yellowish minerals are sulfide. B: μ XRF map with normalized relative concentrations of Ni (red), Cu (green), and S (blue) with pyrrhotite appearing as blue, pentlandite as magenta, and chalcopyrite as green. C: μ XRF map with normalized relative concentrations of Cr (red), Fe (green), and Ca (blue) resulting in the sulfides appearing as green, olivine and pyroxene-rich domains as dark brown-orange, chromite as red, and clinopyroxene as blue. The black arrow indicates the direction of the very weak lamination defined by orthopyroxene oikocrysts. Abbreviations: Cpx = clinopyroxene, Chr = chromite, Fe-Chr = ferrichromite, Ol = olivine, Opx = orthopyroxene, Pn = pentlandite, Po = pyrrhotite, Sul = sulfides.

Figure 16. Scanned image of a 1.30 meter interval of disrupted-net texture and invading pyroxenite (NQ half core, 4.5 cm wide) (NOT-09-053/857.1). White dotted lines indicate the gradational contact between the pyroxenite and the net-textured sulfide facies into the disrupted net-textured sulfide subfacies rock. The disrupted-net texture (DN) at the top of the interval becomes a transition zone (TZ) which gives way to invading pyroxenite (IP), an additional transition zone, and finally a zone of disrupted-net texture.

Figure 17. Scanned images of disrupted-net-textured sulfide (NQ half core, 4.5 cm wide) and photomicrographs from thin sections (2.5x magnification). A: Core scan of disrupted-net texture with larger zones of sulfide-free pyroxenite (NOT-09-056/540.83). B: Core scan of

pinto/disrupted-net texture hybrid; like pinto-net-texture (Fig. 15A), orthopyroxene (Opx) crystals are easily distinguished, but here make up the majority of disrupting pyroxenite (NOT-10-076-W1/557.11E). C-D: Photomicrograph of disrupted-net-textured sulfides showing the serpentinized peridotite around the top and the altered pyroxenite containing fresh olivine, polarized reflected light (C) and cross-polarized light (D) (NOT-09-056-W6/782.6). E-F: Photomicrograph of disrupted-net-textured sulfides showing the serpentinized peridotite around the top and altered olivine pyroxenite on bottom (bimodal olivine size), polarized reflected light (E) and cross-polarized light (F) (NOT-07-029/72.3). G-H: Photomicrograph of olivine-pyroxenite domains of disrupted-net texture containing coarse fresh Ol, polarized reflected light (G) and cross-polarized light (H) (NOT-09-053/853.7).

Figures 18. Disrupted net-textured sulfide subfacies from the Eagle's Nest deposit (drillcore NOT-09-053 at 857.26 m, NQ core size). A: A scanned slab of typical disrupted net-textured sulfide. The black minerals are olivine and the yellowish minerals are sulfide. B: μ XRF map with normalized relative concentrations of Ni (red), Cu (green), and S (blue) showing a Po-Pn-Ccp domain adjacent to the disrupting olivine pyroxenite, a Ccp-Po-(Pn) domain moving further from the disruption, and a Po-Pn-Ccp domain on the peripheries C: μ XRF map with normalized relative concentrations of Cr (red), Fe (green), and Ca (blue), showing abundant clinopyroxene (blue) in the disrupting olivine pyroxenite, olivine in black-red, and sulfides in green-yellow. Abbreviations: Ccp = chalcopyrite, Ol = olivine, Pn = pentlandite, Po = pyrrhotite, Px = pyroxene, Pxt = pyroxenite.

Figure 19. Scanned images of patchy-net-textured sulfide (NQ half core, 4.5 cm wide) and photomicrographs from thin sections (2.5x magnification). A: Core scan of patchy-net texture with olivine (Ol), dark blueclinopyroxene (Cpx) and patchy sulfide (Sul) (NOT-10-076/516). B-C: Photomicrograph of patchy-net texture with fresh olivine (Ol), polarized reflected light (B) and cross-polarized light (C) (NOT-10-076/516). D-E: Photomicrograph of patchy-net texture with fresh dark blue clinopyroxene (Cpx) and light grey circular orthopyroxene (Opx) with serpentinized olivine (Ol) chadacryst, polarized reflected light (D) and cross-polarized light (E) (NOT-07-028/207.1).

Figure 20. Scanned images of semi-massive sulfide (NQ half core, 4.5 cm wide) and photomicrographs of semi-massive sulfide (2.5x magnification). A: Core scan of semi-massive sulfide with inclusion of gabbro (GI) (NOT-09-053-W6/761.8, two fragments). B-C: Semi-massive sulfide showing a peridotite inclusion within massive sulfide domain in polarized reflected (B) and cross-polarized light (C) (NOT-07-29/68.3). D-E: Semi-massive sulfide with gabbro inclusion showing feldspar and clinopyroxene (Cpx) in polarized reflected (D) and cross-polarized transmitted light (E) (NOT-10-087A/60.7).

Figure 21. Scanned images of massive sulfide (NQ half core, 4.5 cm wide) and photomicrographs from thin sections of massive sulfide (2.5x and 1x magnification). A: Core scan of massive sulfide with medium-grained pentlandite (Pn) eyes amongst pyrrhotite (Po) and chalcopyrite (Ccp) (NOT-10-076-W1/573.3). B: Core scan of massive sulfide with abundant fine-grained Pn 'eyes' and a

Ccp-rich domain on the left side, with minor magnetite (Mag) throughout (NOT-07-028/217.65). C: Core scan of contact between massive sulfide and country rock tonalite, with mm-scale sulfide protrusion within the tonalite (NOT-07-018/175.2). D: Core scan of contact between massive sulfide containing fragments of net-textured sulfides (upper left) (NOT-07-028/206.18). E: Core scan of contact of massive sulfide with ultramafic host rock, containing clast of same pyroxenite. Note the sulfide zonation with Po-Pn dominated domain versus Po dominated domain (NOT-09-059/507.17) F: Core scan of contact of massive sulfide and disrupted-net texture, with pyroxenite (Pxn) amongst isolated olivine (ol) and sulfide (Sul) cumulate; sulfide overfills net texture at contact (NOT-09-064/1104), G: Core scan of massive sulfide, containing isolated clasts of disrupted net-texture. Note the sulfide protrusion within the disrupted-net-textured inclusion. (NOT-09-071/728.5). H: Photomicrograph of massive sulfide with pentlandite (Pn) ‘eyes’ and large chalcopyrite (Ccp) and pyrrhotite (Po) with small magnetite (Mag) crystals in polarized reflected light (NOT-07-028/217.6). I: Photomicrograph of massive sulfide with Pn ‘eyes’ and large Ccp grains with minor fracturing in pyrrhotite, polarized reflected light (NOT-07-018/222.1.),

Figure 22. Massive and semi-massive sulfide facies at the Eagle’s Nest deposit (drillcore NOT-10-087A at 608 m, NQ core size). A: A scanned slab of typical semi-massive sulfides containing numerous gabbroic inclusions (dark grey on the left side) and massive sulfide (right side). The yellowish minerals are sulfide and fine black minerals are fine ferrichromite. B: μ XRF map with normalized relative concentrations of Ni (red), Cu (green), and S (blue). C: μ XRF map with normalized relative concentrations of Cr (red), Fe (green), and Ca (blue). Abbreviations: Ccp = chalcopyrite, Cpx = clinopyroxene, Fe-Chr = ferrichromite, Pl = plagioclase, Pn = pentlandite, Po = pyrrhotite.

Figure 23. Semi-massive sulfide facies at the Eagle’s Nest deposit (drillcore NOT-09-057 at 584.4 m, NQ core size). A: A scanned slab of typical semi-massive sulfides containing numerous Ca-rich fragments (dark grey). Black minerals are olivine and yellowish minerals are sulfide. B) μ XRF map, normalized relative concentrations of Ni (red), Cu (green), and S (blue). C) μ XRF map, normalized relative concentrations of Cr (red), Fe (green), and Ca (blue). The coarse yellow patches within pyrrhotite crystals in this image are diffraction artefacts.

Figure 24. Ternary diagrams showing compositions of pyrrhotite, pentlandite and chalcopyrite.

Figure 25. Backscattered electron microscope images of platinum-group minerals (PGM) in the Eagle’s Nest deposit. A: Composite PGM within massive pyrrhotite (Po) and minor pentlandite (Pn), darker phase is tellurium-palladium-bismuth (Merenskyite) and lighter phase is Bi-Pd-Te (Michenerite) (NOT-07-05/124). B: Composite PGM within massive sulfide (NOT-07-05/124m), darker zone is tellurium-palladium-bismuth (Merenskyite), lighter zone is bismuth-palladium-tellurium(Michenerite). C: Zoned PGM within massive pyrrhotite (NOT-07-05/114); lighter zone is palladium-ruthenium-osmium (alloy), darker zone is arsenic-platinum-rhodium. Te = Tellurium; Pd = Palladium, Bi = Bismuth, Rh = Ruthenium, Os = Osmium, As = Arsenic, Pt = Platinum, Rh = Rhodium

Figure 26: Bivariate diagrams of selected whole rock oxides against MgO showing barren and mineralized samples from this study with sulfides subtracted, barren samples from other studies, analyzed olivines from this and other studies. Calculated MgO compositions of olivine (assuming stoichiometric $\text{SiO}_2\text{-MgO-FeO}_t$, no $\text{TiO}_2\text{-Al}_2\text{O}_3$, 0.2% NiO and 0.3% $\text{CaO-Cr}_2\text{O}_3$), and liquids in equilibrium with olivine. In general, SiO_2 (A), TiO_2 (B), Al_2O_3 (C), and CaO (F) decrease with increasing MgO, whereas Cr_2O_3 (D) and FeOt (E) increase with increasing MgO. The Cr_2O_3 plot contains fields for cotectic olivine-chromite cumulates (light green) and non cotectic olivine-chromite cumulates (red). The olivine-chromite mixing line contains ratios of each mineral (olivine = red, chromite = black) at different compositions (see Barnes, 1998). The FeOt plot also indicates that the magma which formed the sulfide-bearing rocks was more magnesian than the minimal fresh olivine samples analyzed in the deposit.

Figure 27. Primitive mantle-normalized abundances of highly-incompatible elements in barren ultramafic rocks in the Eagle's Nest dike, showing enrichment in highly incompatible lithophile elements (Cs, U, Th, LREE) relative to Nb-Ta and moderately incompatible lithophile elements (Y, Zr-Hf, MREE), suggests that the magma was contaminated by upper continental crust during ascent.

Figure 28. Th/Yb vs Nb/Yb plots (Pearce, 2008). A: Th/Yb versus Nb/Yb plot of barren rocks in the Eagle's Nest dike compared to the mantle array. Th = Thorium, Yb = Ytterbium, Nb = Niobium, N-MORB = normal mid-ocean basalt, E-MORB = enriched mid-ocean basalt, OIB = ocean island basalt, PM = primordial mantle, A = Archean Crust, P = Felsic Phanerozoic crust, MC = Middle Crust, LC = Lower Crust, UC = Upper Crust, CC = Average continental crust. B: Th/Yb vs Nb/Yb plot of barren rocks compared to compositions of Archean upper crust (AUC) and Archean Felsic Crust (AFC) with various amounts of contamination (F) (Rudnick and Gao, 2003).

Figure 29. Histograms showing the distribution of whole rock sulfur content by subfacies of net-textured sulfides.

Figure 30. Metals versus S plots showing samples from this study (colours) and from Noront assay database (grey). A: Ni vs S. B: Cu vs. S. C: Fe vs S. D: Pt vs S. E: Pd vs S. F:Ag vs S. G: Au vs S. Fe-Ni and weakly Cu correlate positively with S; Pd and Ag correlate weakly with S; Pt and Au do not correlate with S.

Figure 31. Tukey box plot diagrams showing S and metal compositions in Eagle's Nest. The lower fence/whisker representing the interquartile range (IQR: box length) divided by 1.5, the lower part of the box the 25th percentile, the upper part of the box the 75th percentile, and the upper fence/whisker representing $\text{IQR} * 1.5$. The dot represents the mean and the horizontal line represents the median. Outliers (between $\text{IQR} * 1.5$ and $\text{IQR} * 3$) and far outliers ($>\text{IQR} * 3$) are represented by open circles and far outliers, respectively, and have not been included in ranges described in the text. A-C-E-G consist of data from Noront's database and this study and B-D-F-H are based solely on sub-species of net-textured sulfides from this study. A-B: S contents of sulfide facies and subfacies. C-D: Ni contents of sulfide facies and subfacies. E-F: Cu contents of sulfide facies and subfacies. G-H: Fe contents of sulfide facies and subfacies.

Figure 32. Tukey box plot diagrams showing Ca, Pt and Pd in Eagle's Nest. A-B: Ca contents of sulfide facies from Noront assays and subfacies of net-textured sulfides (this study). C-D: Pd contents of sulfide facies from Noront Assays and subfacies of net-textured sulfides (this study). E-F: Pt contents of sulfide facies from Noront Assays and subfacies of net-textured sulfides (this study).

Figure 33. Tukey box plot diagrams showing amount of Au and Ag at Eagle's Nest, in ppm. A-B: Au contents of sulfide facies deduced from Noront Assays and subfacies of net-textured sulfides (this study). C-D: Ag contents of sulfide facies deduced from Noront Assays and subfacies of net-textured sulfides (this study).

Figure 34. Tukey box plot diagrams showing ore tenors (metals in 100% sulfides) at Eagle's Nest. A-B: Ni tenors (Ni_{100}) of sulfide facies deduced from Noront Assays and of subfacies of net-textured sulfides (this study). C-D: Cu tenor (Cu_{100}) of sulfide facies deduced from Noront Assays and of subfacies of net-textured sulfides (this study). Note that median (horizontal line in box) tenors are roughly similar across all textures.

Figure 35. Bivariate diagram showing A: Ni_{100} (Ni tenor) versus Cu_{100} , B: Pt_{100} versus Cu_{100} and C: Pd_{100} versus Cu_{100} . Noront assays from disseminated sulfide facies in purple and from non-disseminated sulfide facies in grey. Other symbols represent samples from this study. The projection of R-factor from Mungall et al. (2010) are shown as red lines. The calculated R-factor ($r = 150$, star) from this study is slightly lower than the calculated R-Factor ($r = 225$) in Mungall et al. (2010).

Figure 36. Precious and base metals normalized to primitive mantle in mineralized samples from Eagle's Nest compared to Raglan and Kambalda (Naldrett 2004, black). Normalization values from McDonough and Sun (1995).

Figure 37. Calculated metal abundances in sulfide melts (A) and derivative magmas (B) versus sulfide:magma ratio (R factor) for a parental Eagle's Nest magma containing 900 ppm Ni, 60 ppm Cu, 100 ppm Co, and 10 ppb Pd (Leshner and Campbell, 1993). Partition coefficients ($D_{sul/sil}$) are 150 Ni, 600 Cu, 30 Co, and 3^4 ppb Pd. Thicker lines represent Eagle's Nest values.

Figure 38. $\delta^{34}S$ values of mineralized rocks in the Eagle's Nest dike (EN, this study), Black Thor intrusion (Farhangi, MSc Thesis, 2020), and footwall magnetite-silicate-sulfide iron formation (Carson et al., in prep.) Green band represents MORB values (0.1 ± 0.5 range, Sakai et al., 1984), BTI = Black Thor Intrusive Complex, IF = Iron Formation

Figure 39: Reconstructed evolution of the Eagle's Nest dike. **T1:** Intrusion of the first pulse of komatiitic magma, as a blade-shaped dike. **T2:** Additional magma and deposition of olivine phenocrysts and/or olivine primocrysts through *in situ* fractional accumulation (e.g., Leshner, 1989) forming ortho to mesocumulate olivine and minor anteliths/xenoliths. **T3:** Incorporation of S-rich country rock (possibly from footwall iron formations "upstream" from the dike) and generation of immiscible Fe-(Cu) sulfide xenomelts that were upgraded to Fe-Ni-Cu sulfide melts during transport. **T4:** Deposition of sulfide melts onto the cumulus olivine, displacing less-dense silicate

melts, forming leopard-net texture. **T5:** Density-driven segregation of massive sulfide melts in embayments along the base of the dike, enlarged by thermomechanical erosion by sulfides (Groves et al., 1986; Williams et al., 1998). **T6:** Deposition of additional sulfide (waning of system) to form disseminated sulfides/patchy-net textured sulfides. **T7:** Invasion of the dike by one or more pulses of pyroxenite melt and/or Si-Ca rich fluid, generating disrupted-net texture. **T8:** Crystallization of MSS and mobilization of residual sulfide melt (now represented by chalcopyrite) to form cross-cutting veins. **T9:** Waning magmatism, cooling, and solidification followed by serpentinization of olivine. **T10:** Burial, deformation (rotation, regional faulting, local shearing), metamorphism to greenschist facies, and metasomatism by CO₂-rich fluids producing local talc-carbonate alteration of the host rocks.

14 Figures

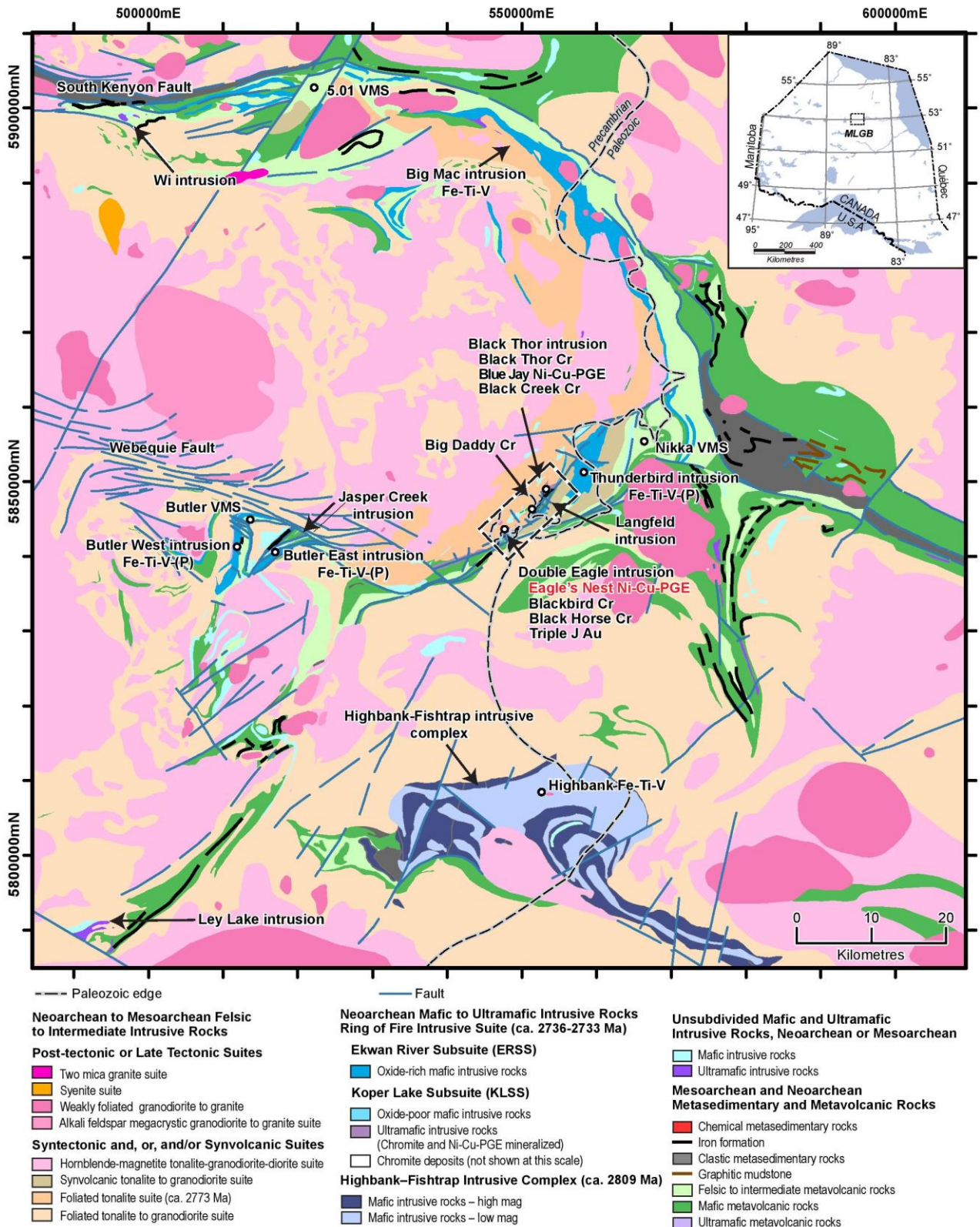
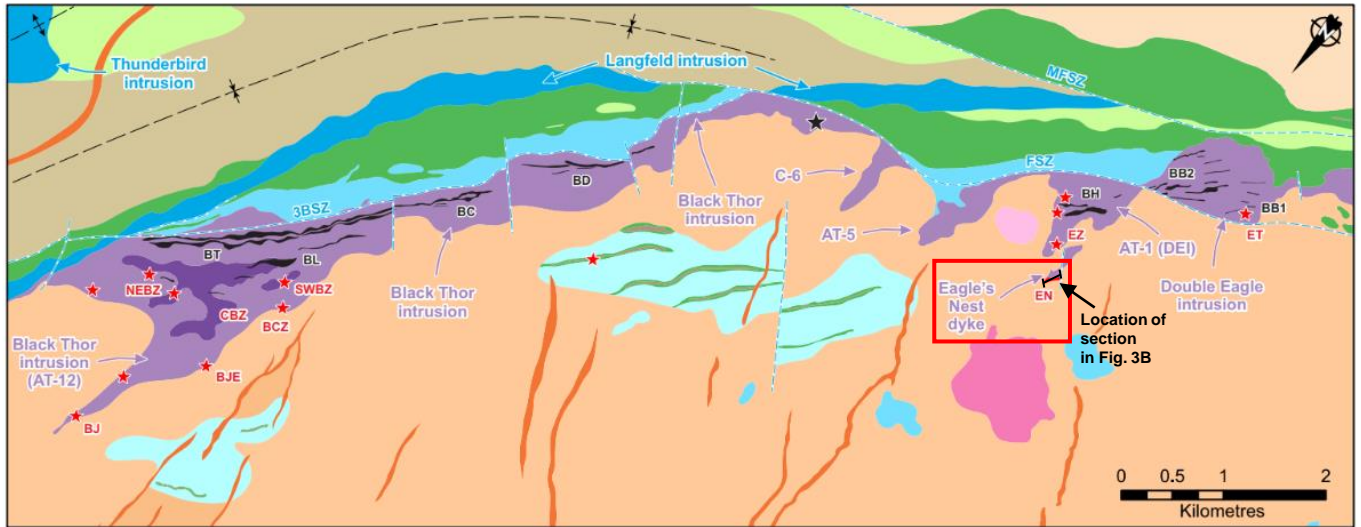


Figure 1.



PROTEROZOIC

Undivided dyke swarm

ARCHEAN

- Weakly foliated granodiorite to granite
- Hbl-Mgt tonalite-granodiorite-diorite suite
- Synvolcanic tonalite to granodiorite suite
- Foliated tonalite suite (ca. 2773 Ma)
- Foliated tonalite to granodiorite suite
- Gabbroic intrusive rocks
- Chemical metasedimentary rocks
- Felsic to intermediate metavolcanic rocks
- Mafic metavolcanic rocks

RING OF FIRE INTRUSIVE SUITE

Ekwan River Subsuite

Oxide-rich gabbroic intrusive rocks

Koper Lake Subsuite

- Late websterite phase
- Oxide-poor gabbroic intrusive rocks
- Ultramafic intrusive rocks
- ★ Chromite-rich rocks - *semi-massive to massive chromitites and layered chromitites (deposit / occurrence)*
- ★ Ni-Cu-(PGE) sulphide mineralization (deposit / occurrence)

Fold axis (*anticline, syncline*)

Fault / Shear zone

- MFSZ : McFaulds Shear Zone
- FSZ : Frank Shear Zone
- 3BSZ : Black Thor-Black Creek-Big Daddy Shear Zone

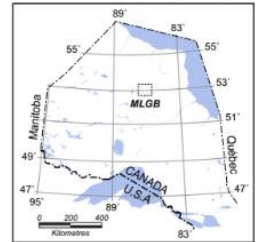
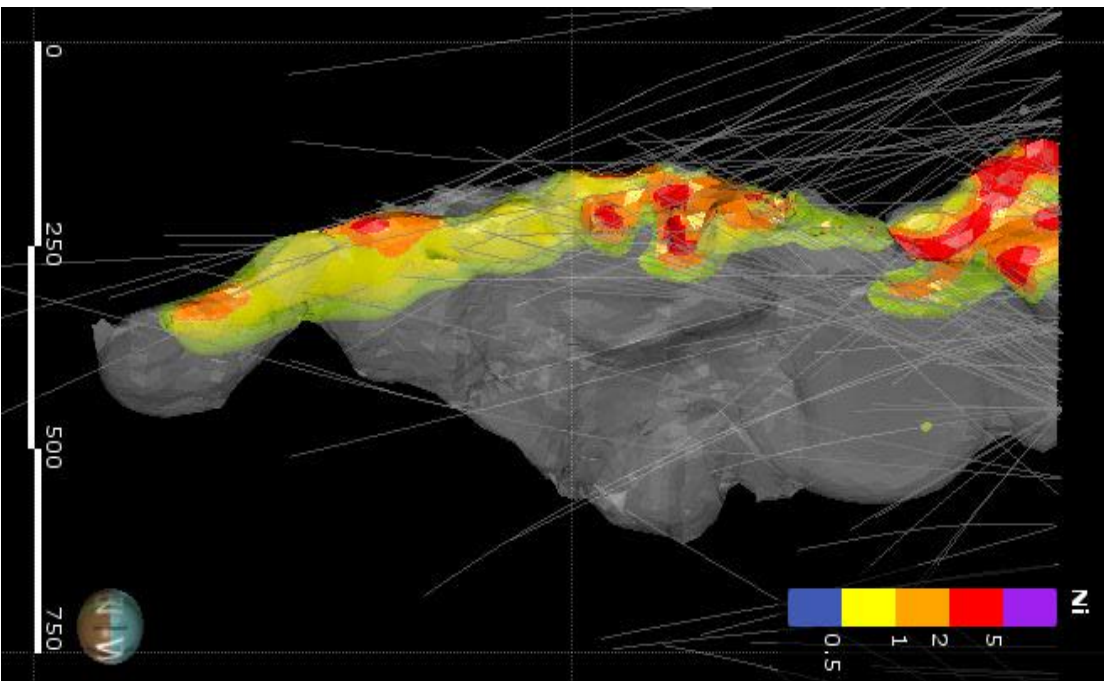


Figure 2.

A



B

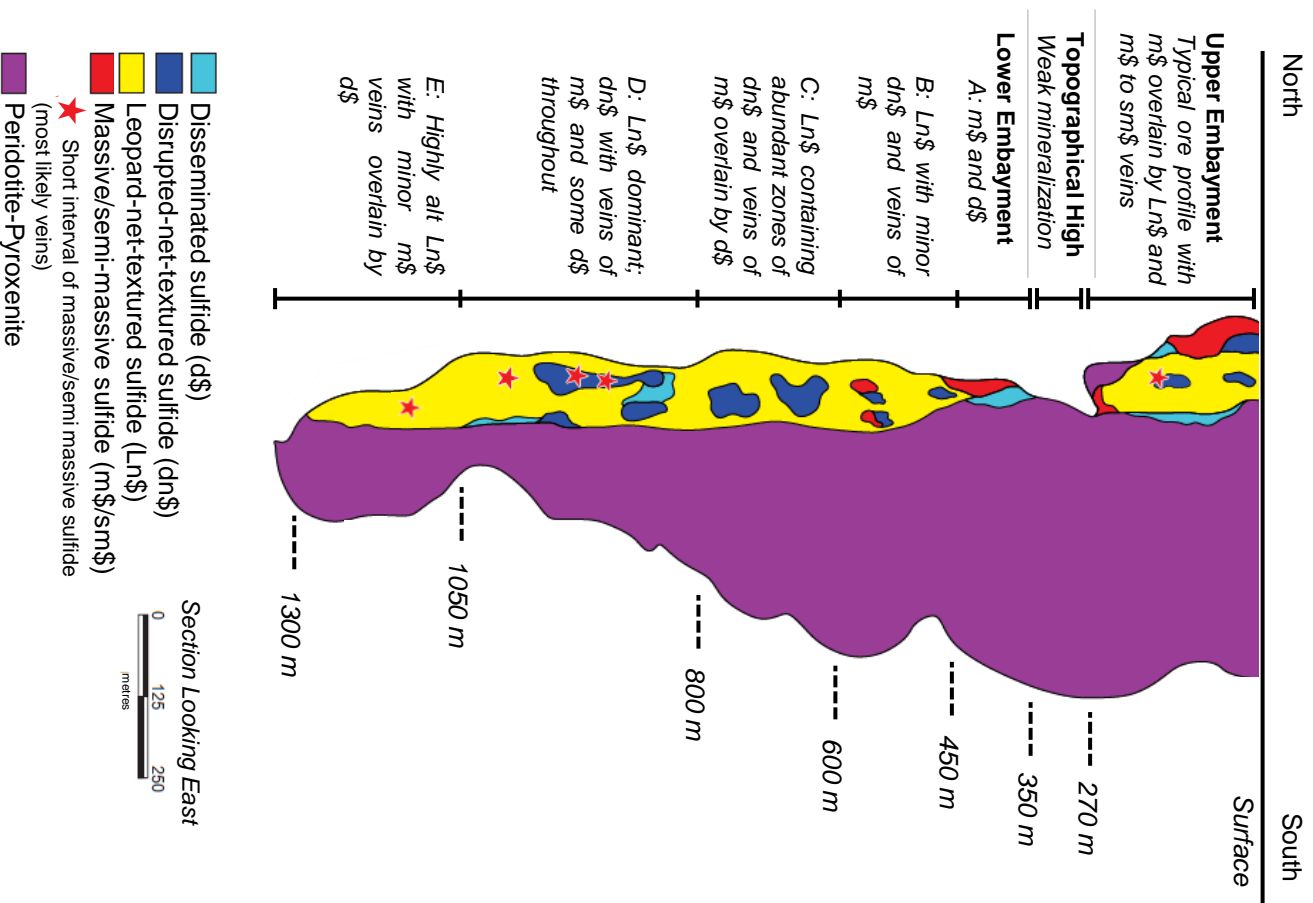


Figure 3.

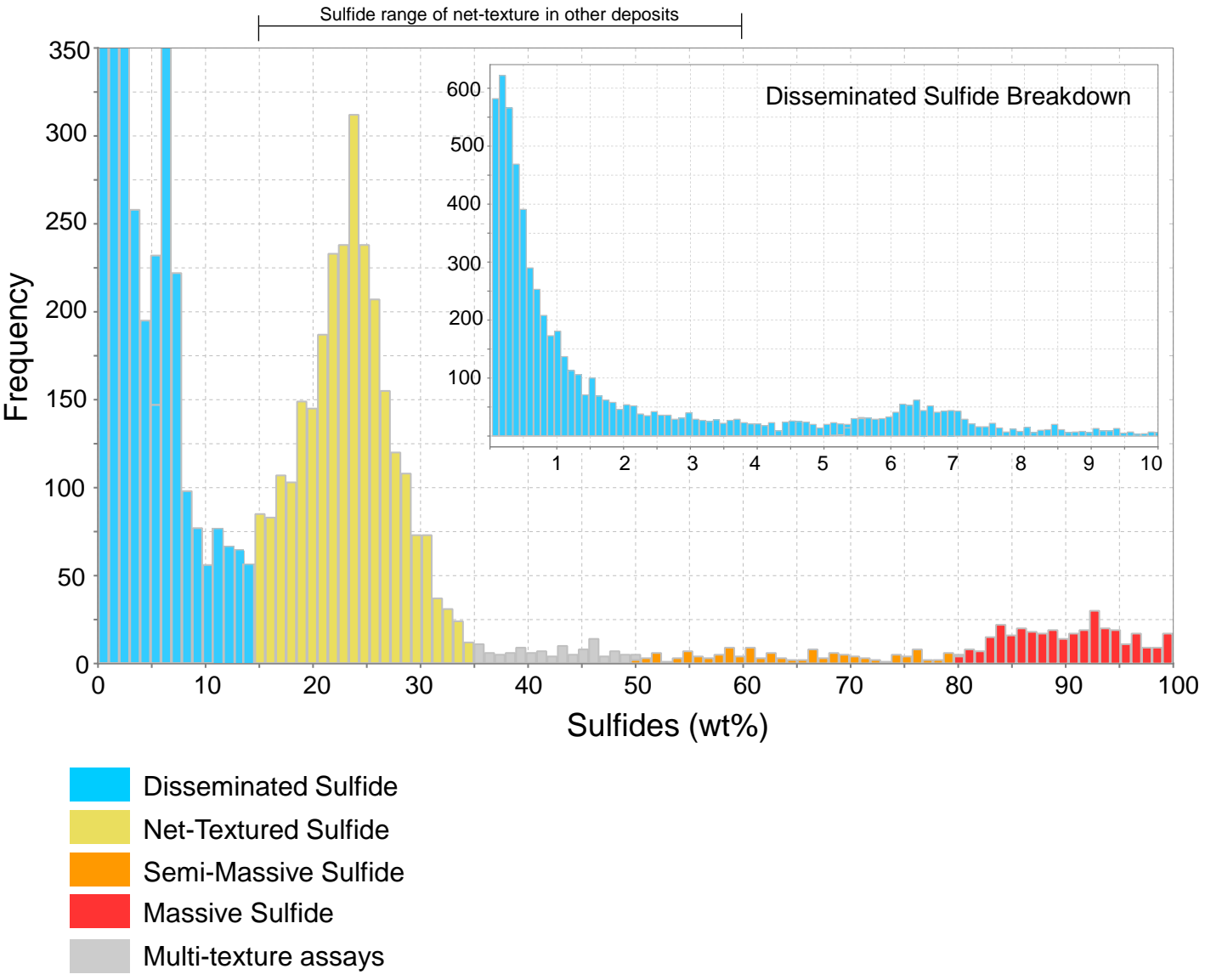


Figure 4.

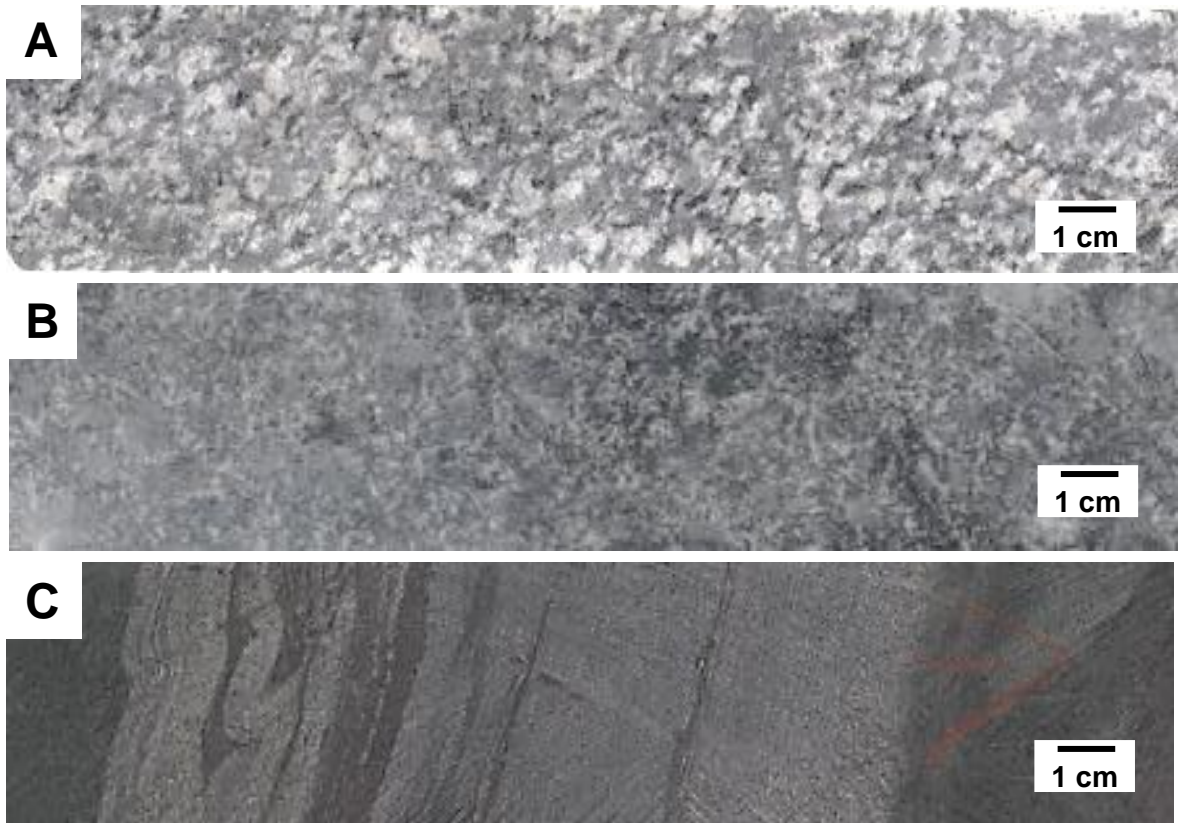


Figure 5.

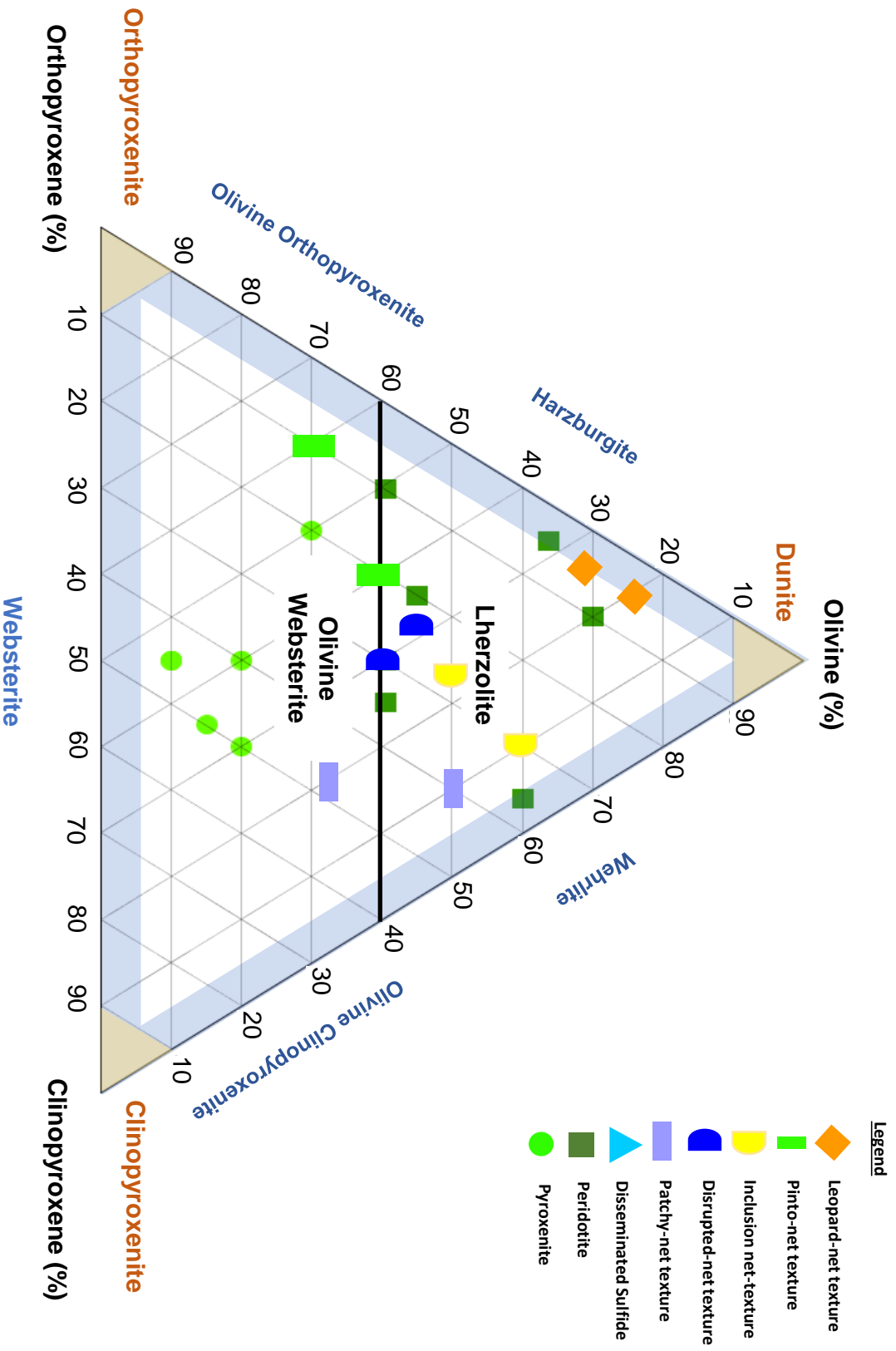


Figure 6.

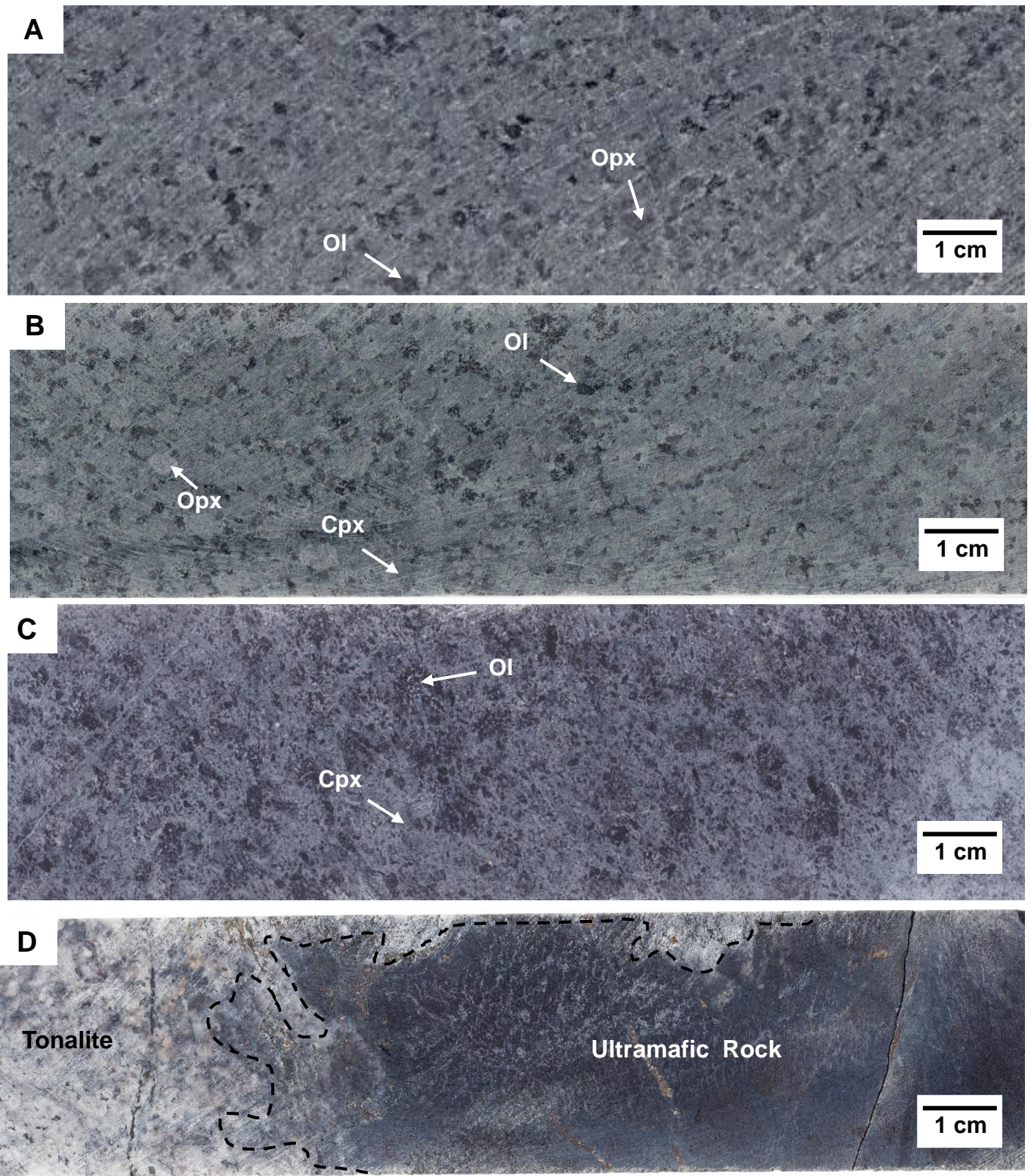


Figure 7.

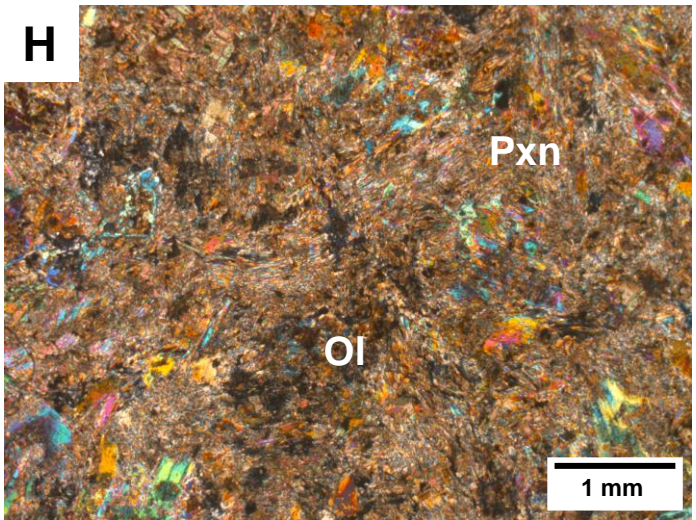
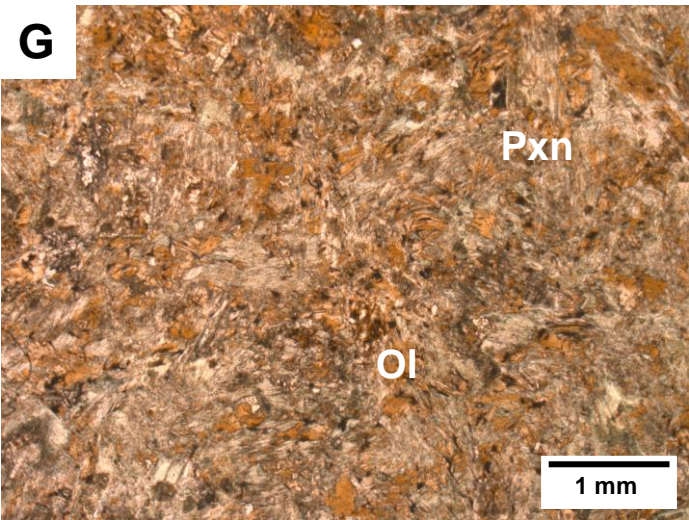
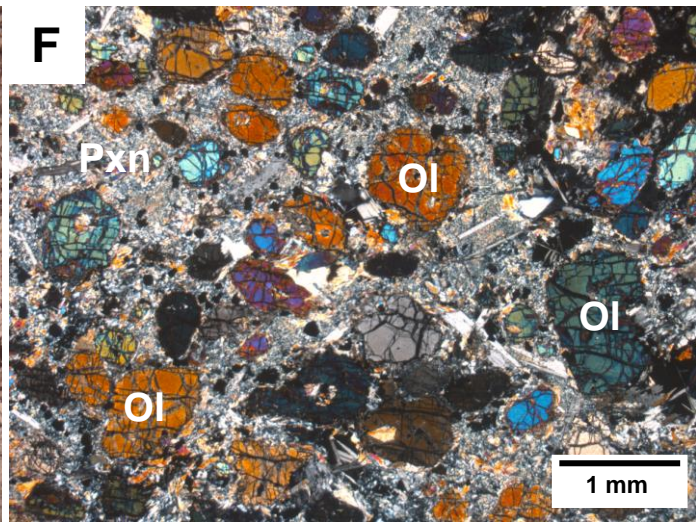
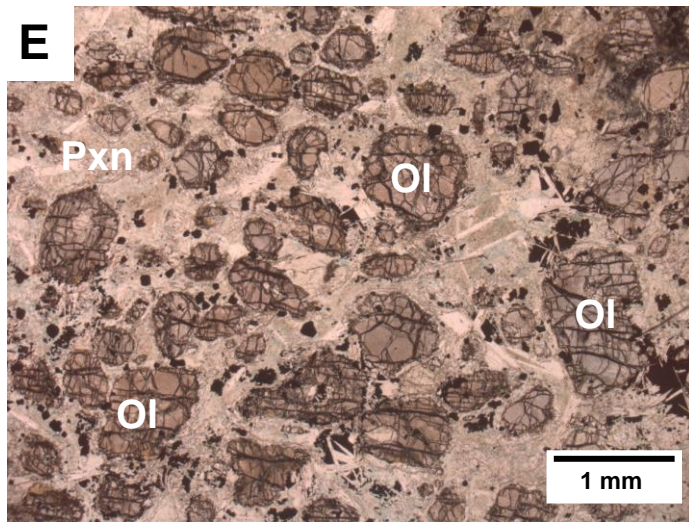


Figure 7 (cont).

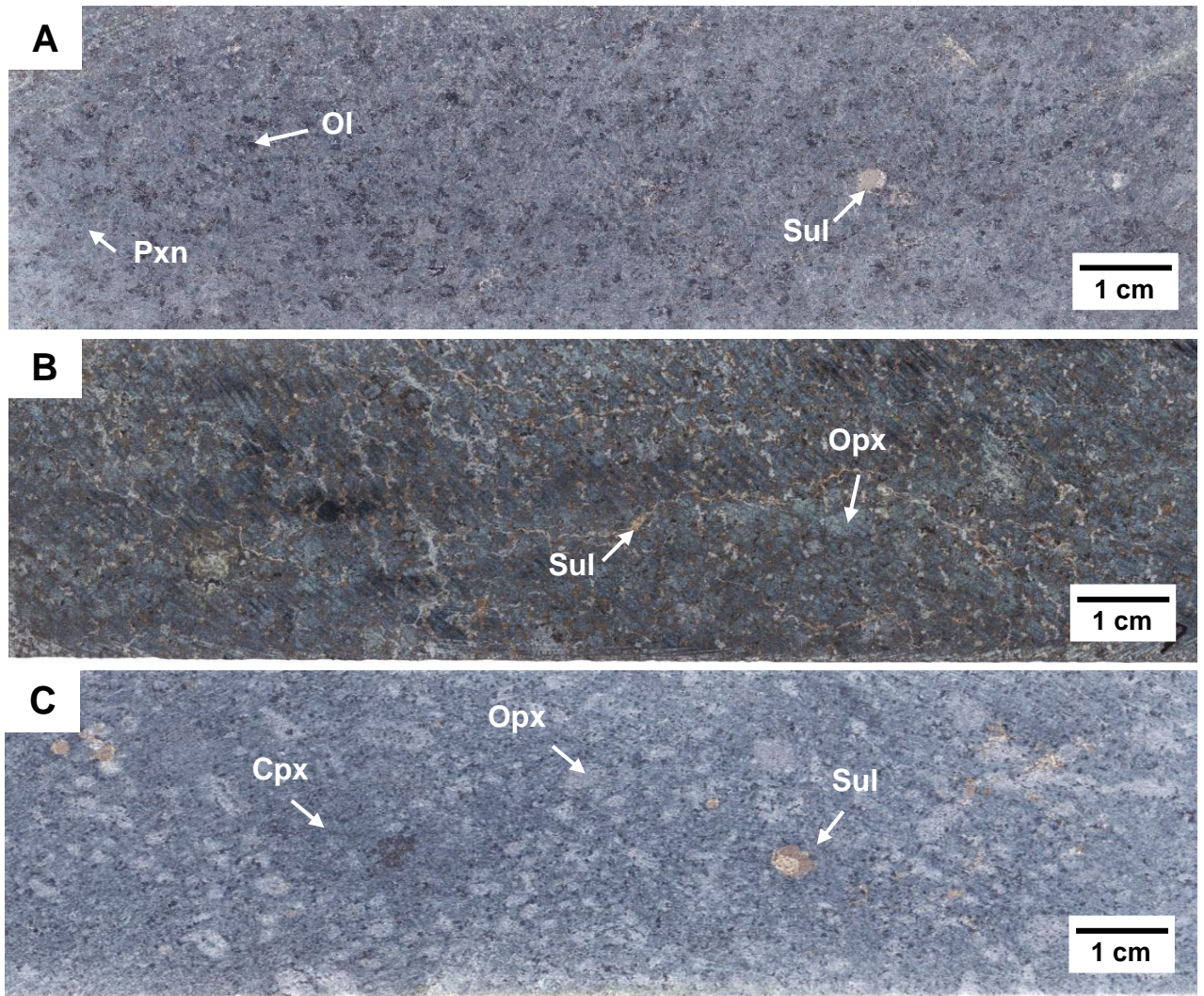


Figure 8.

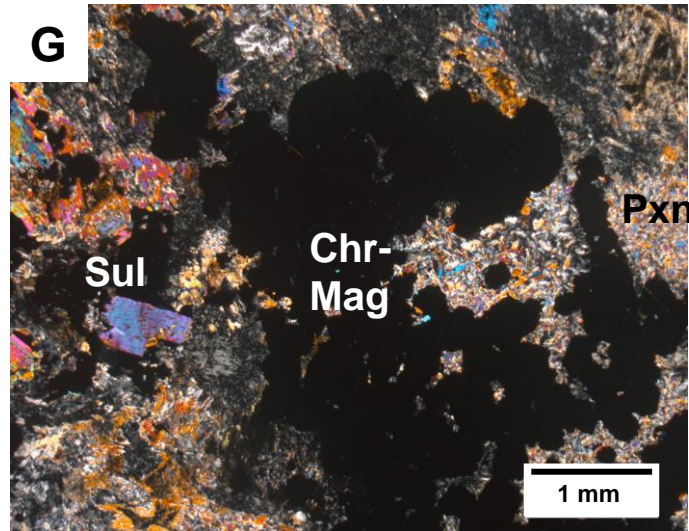
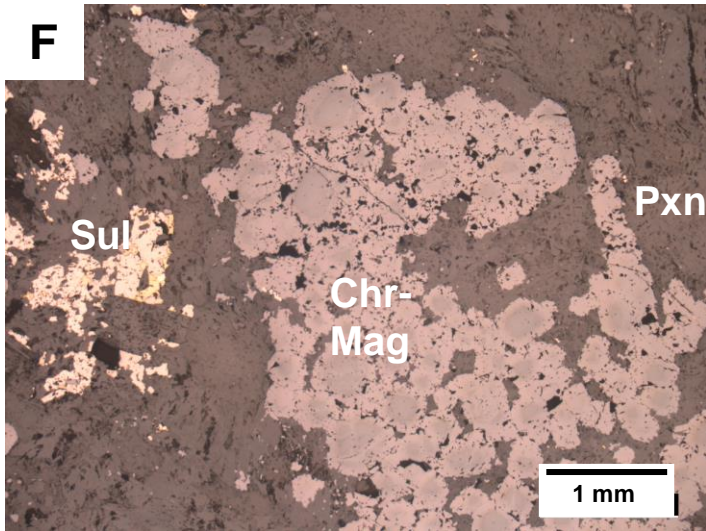
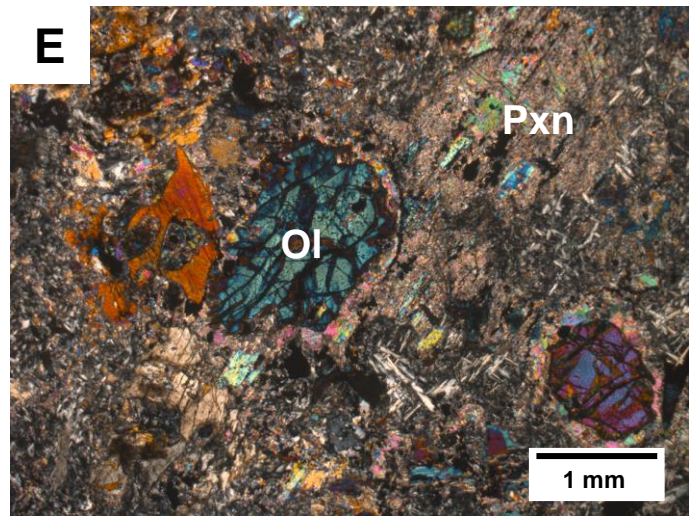
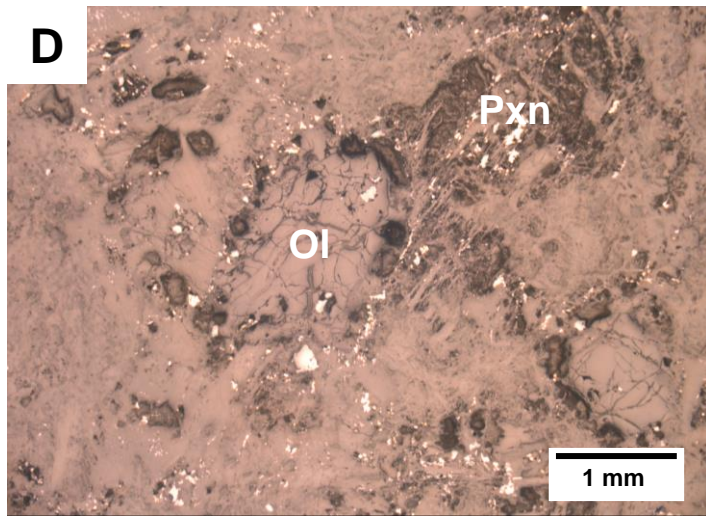


Figure 8 (cont).

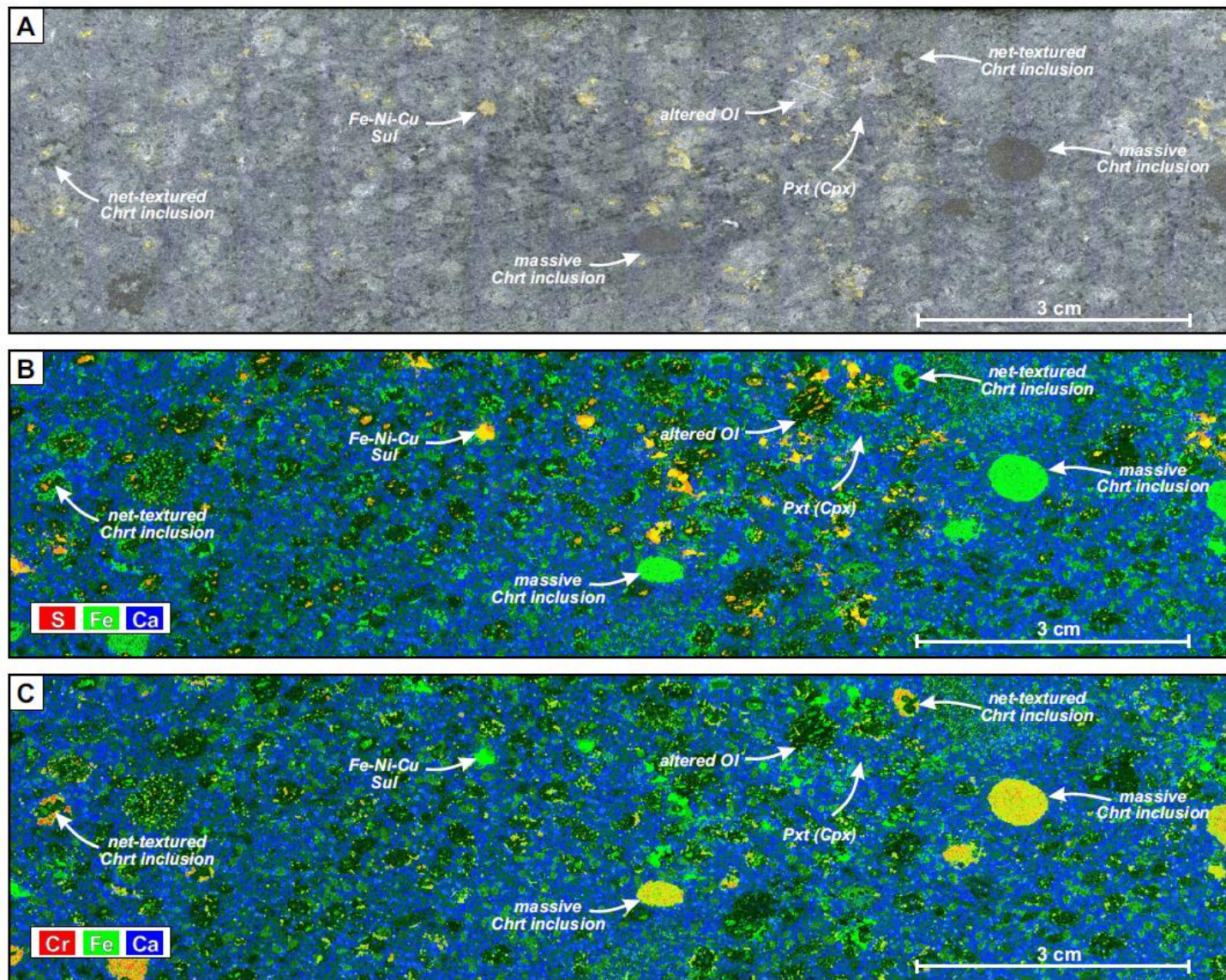


Figure 9.

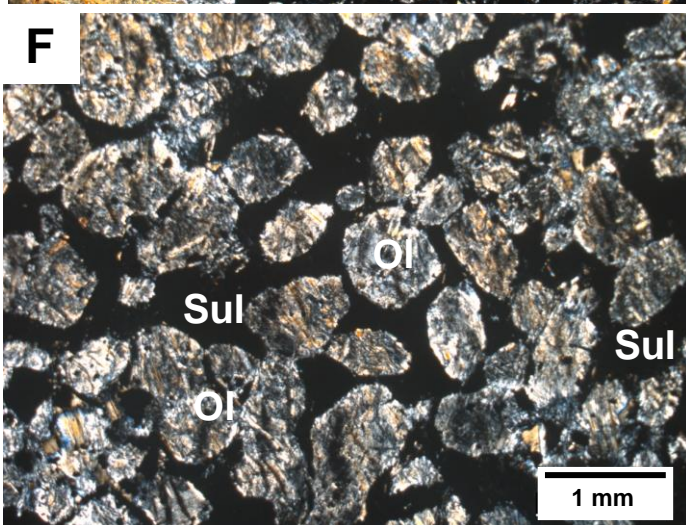
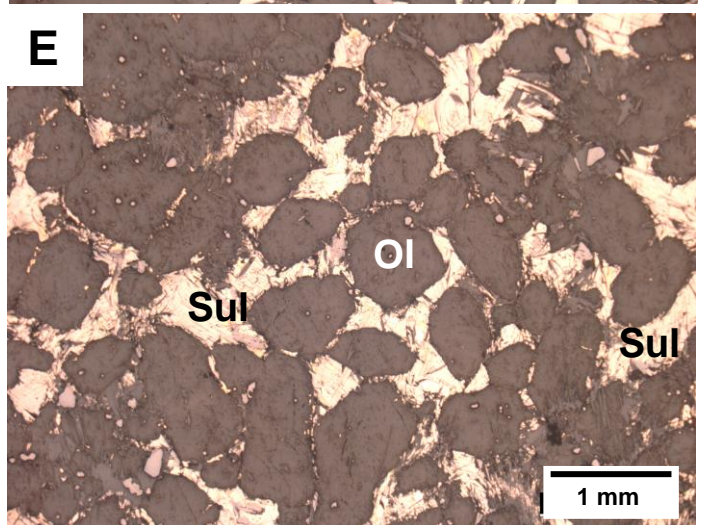
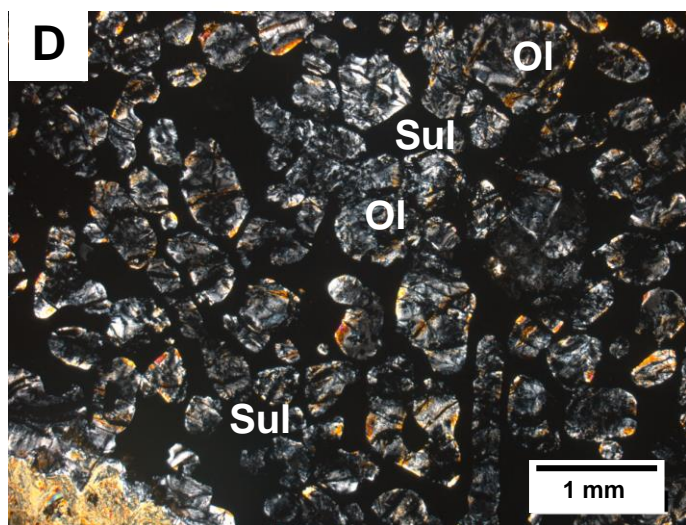
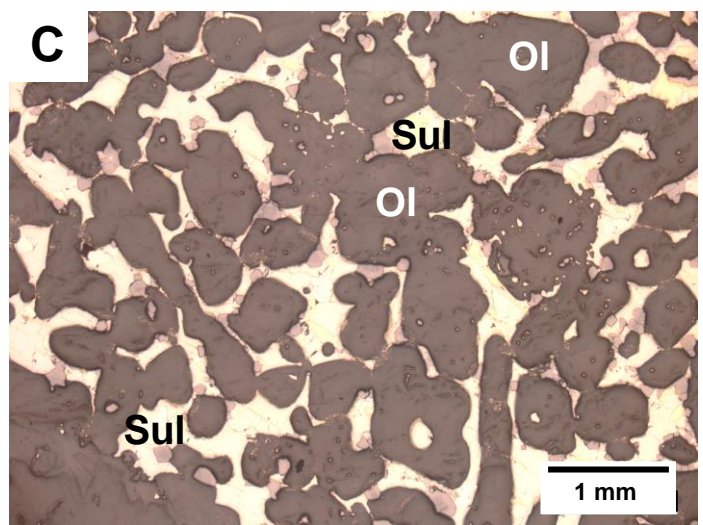
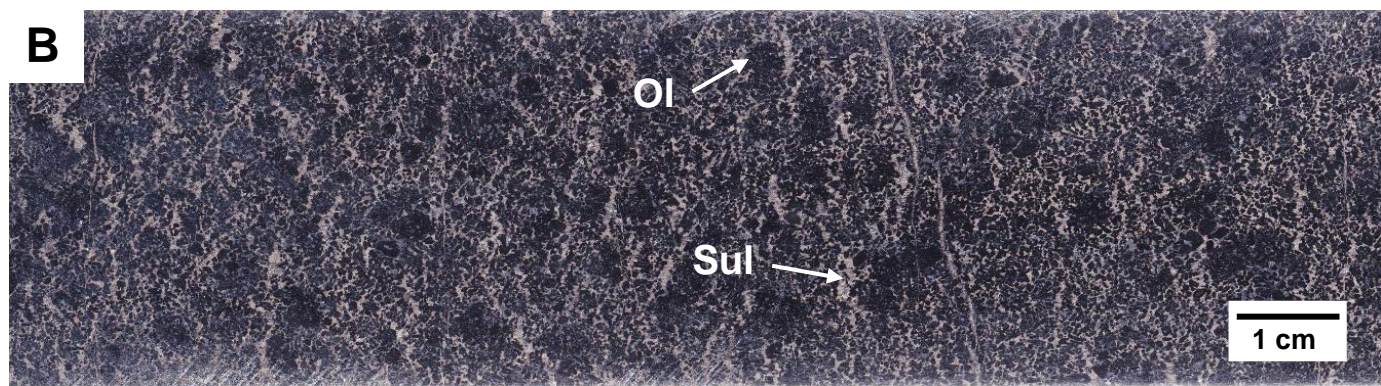
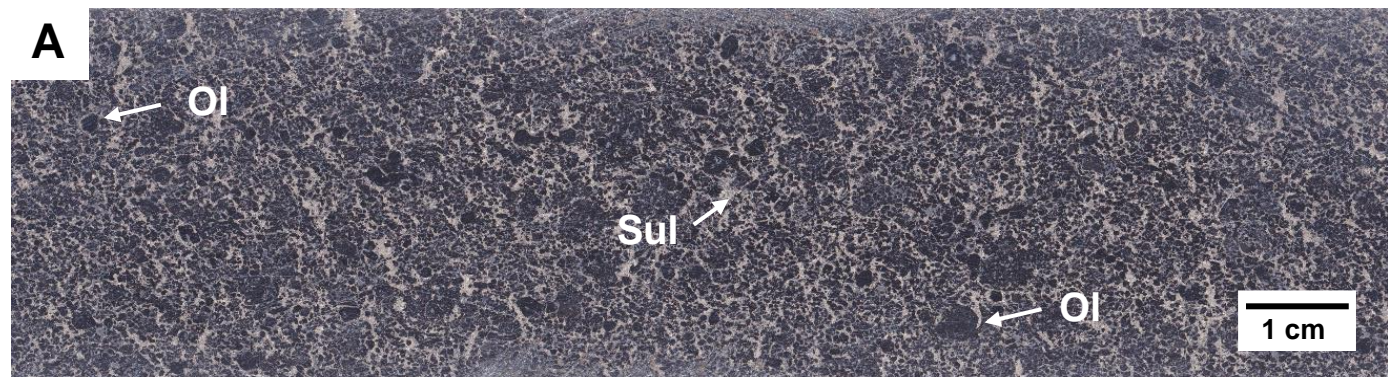


Figure 10

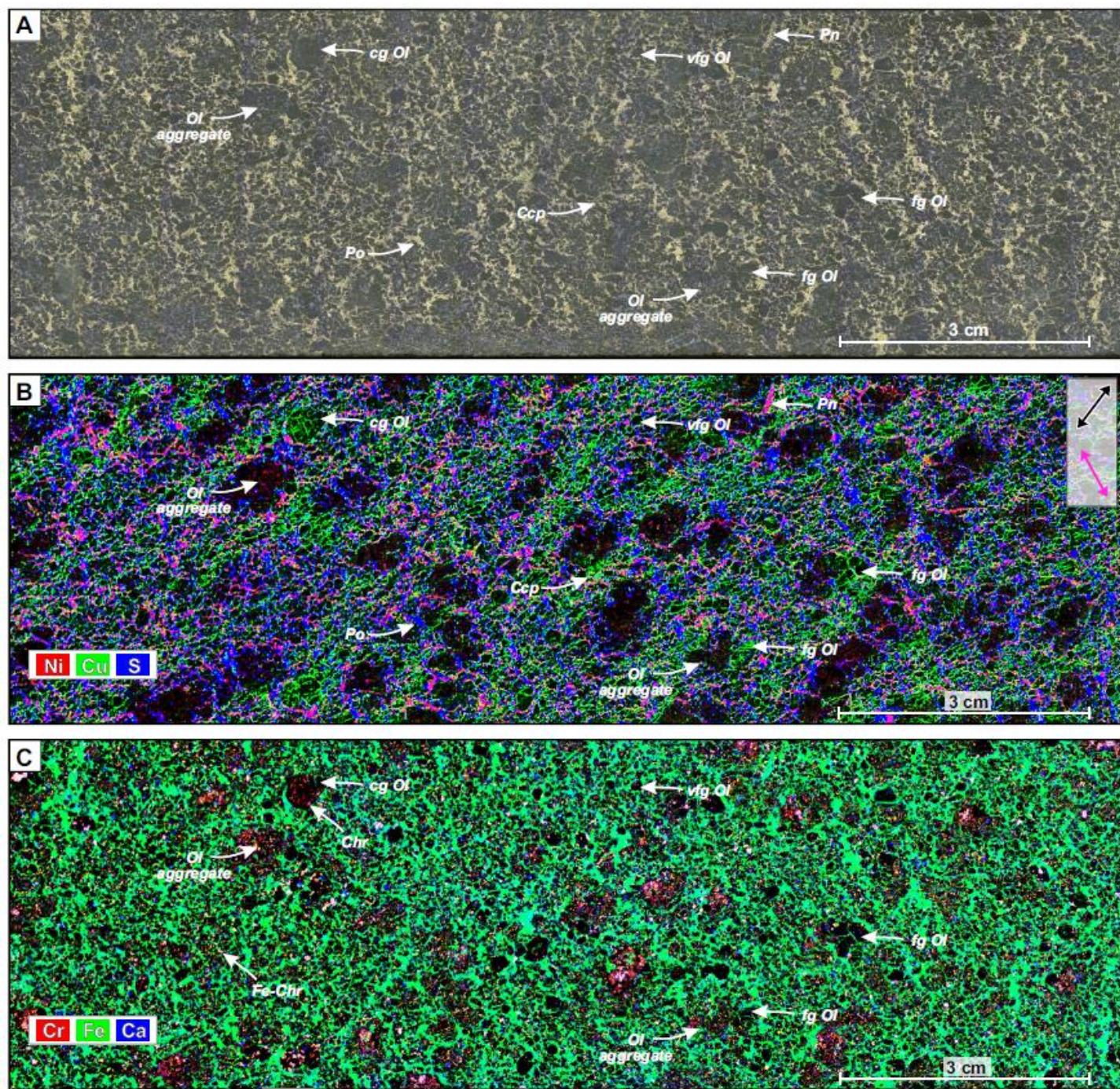


Figure 11.

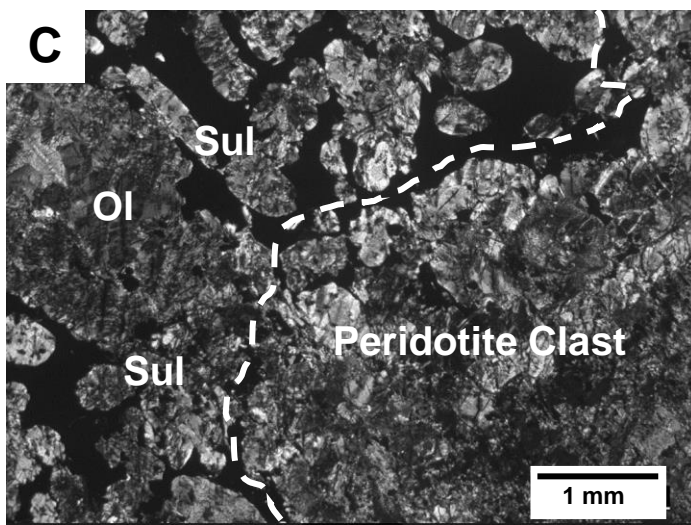
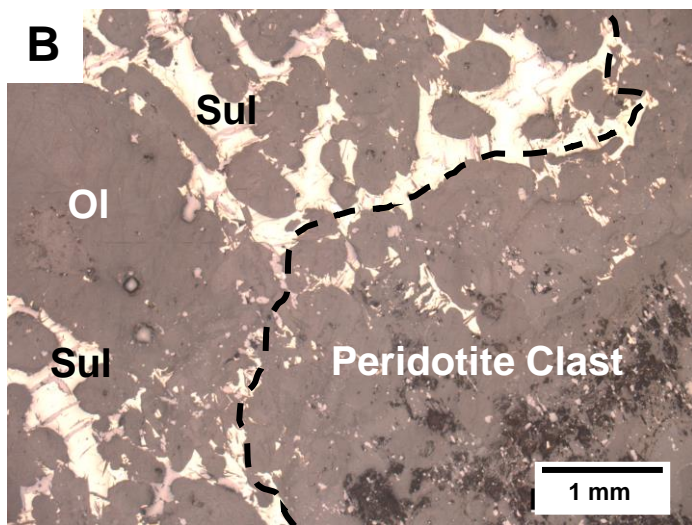
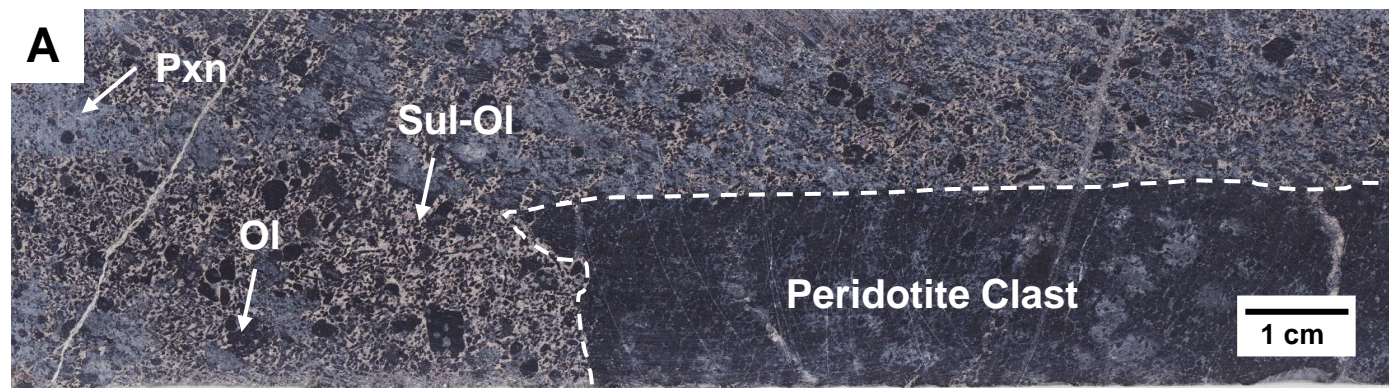


Figure 12.

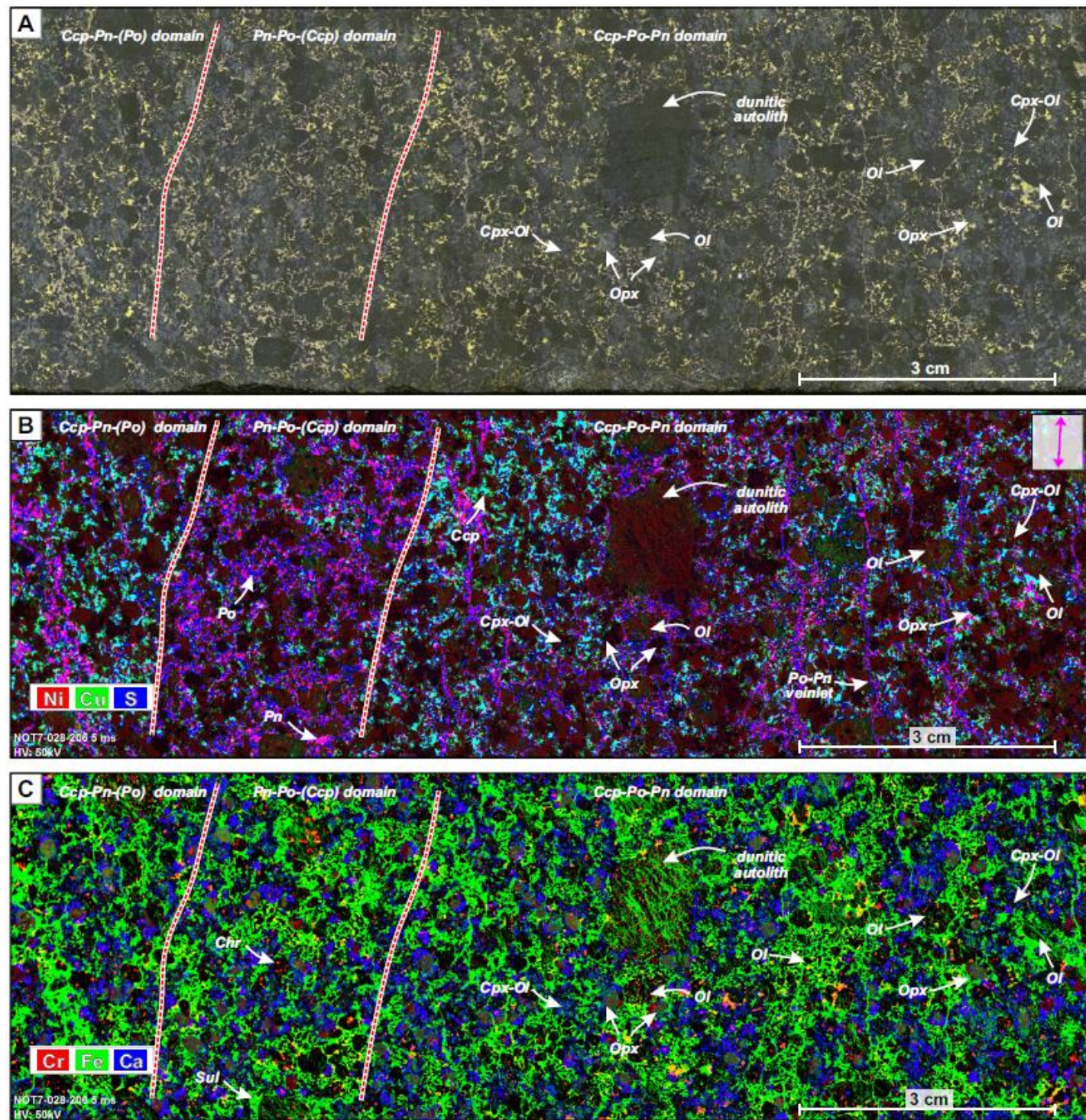


Figure 13.

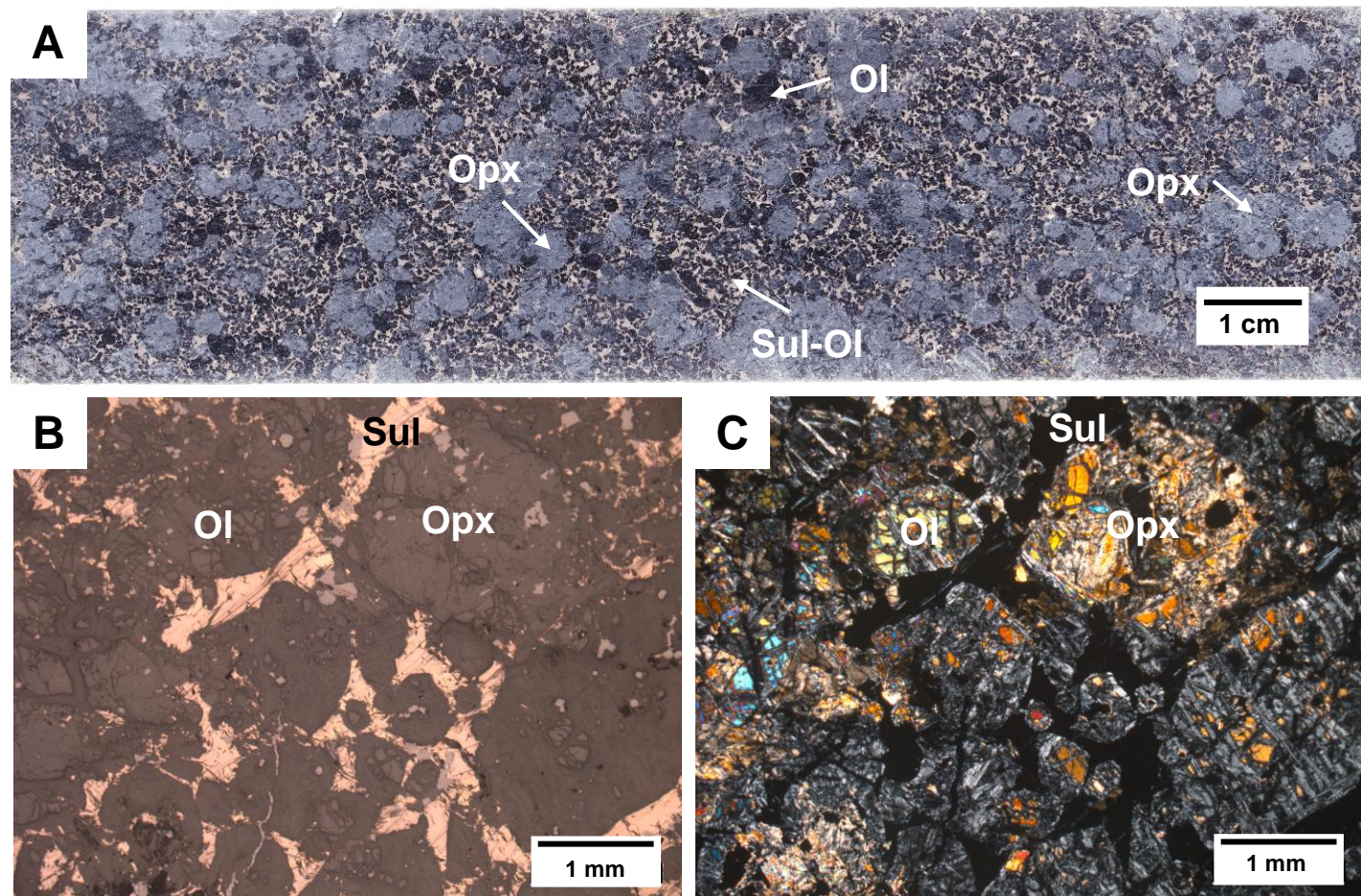


Figure 14.

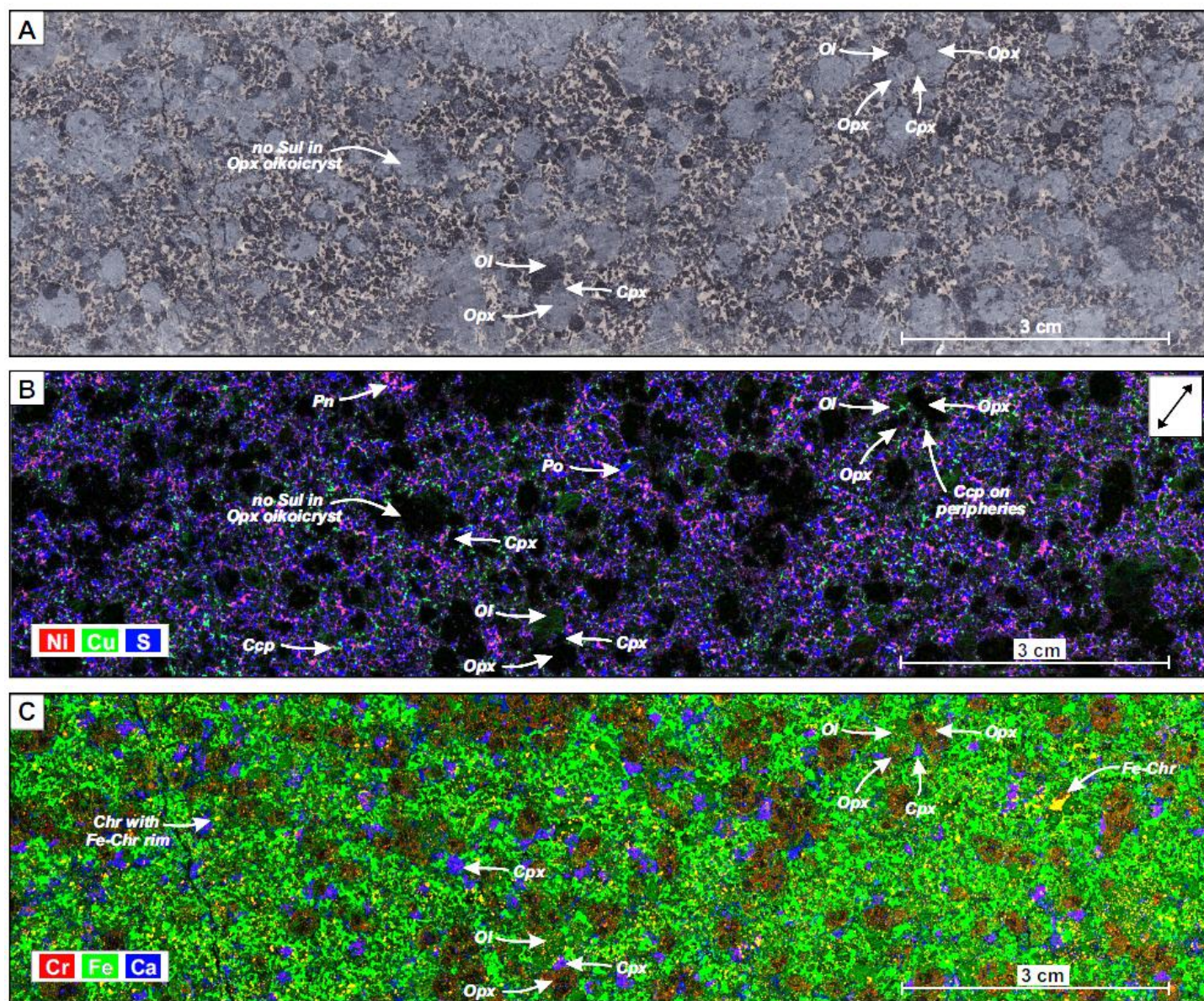
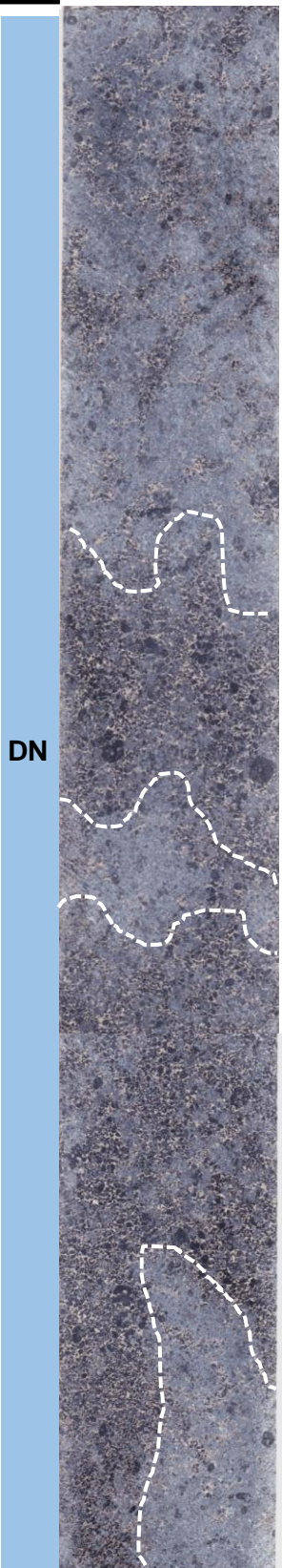
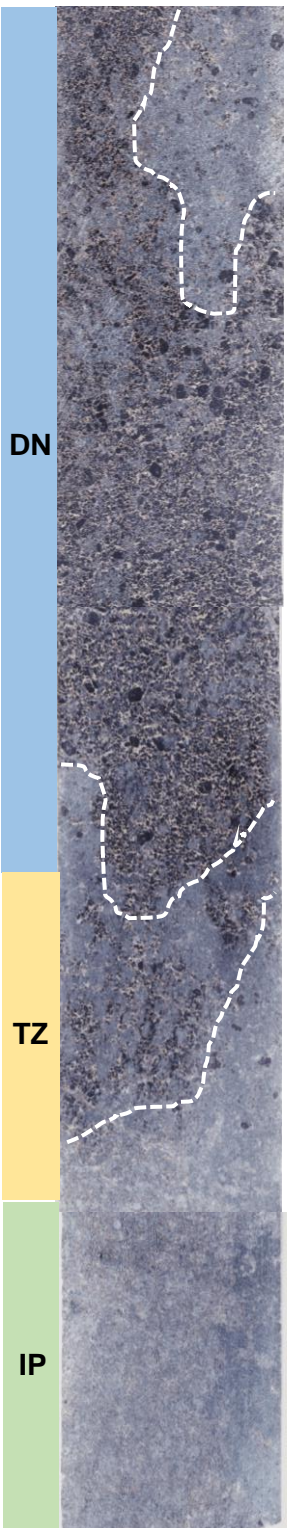


Figure 15.

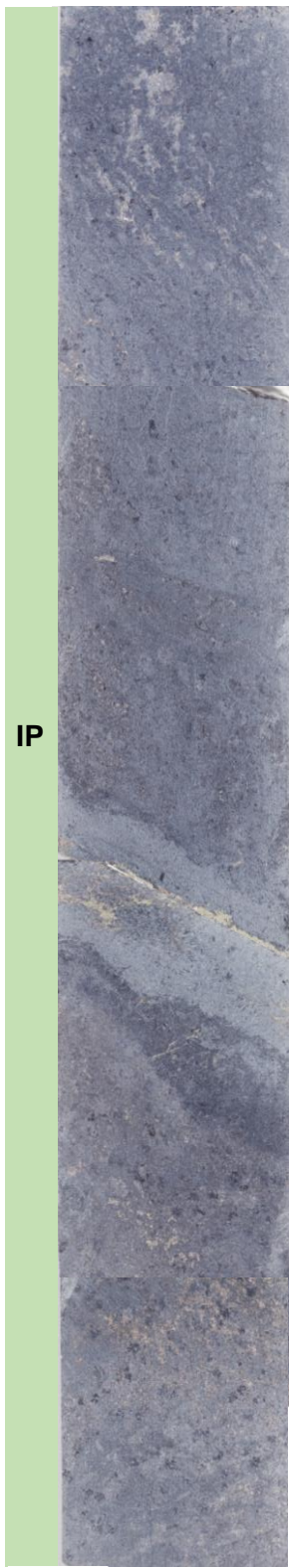
857.1 m



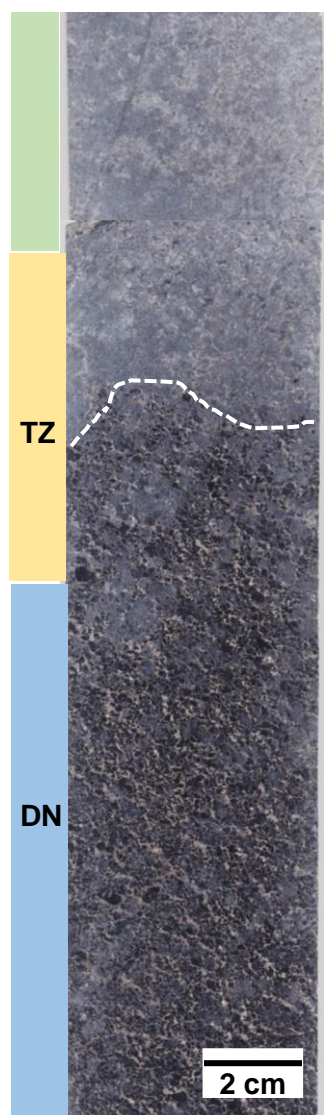
857.6 m



857.9 m



858.2 m



858.4 m

Figure 16.

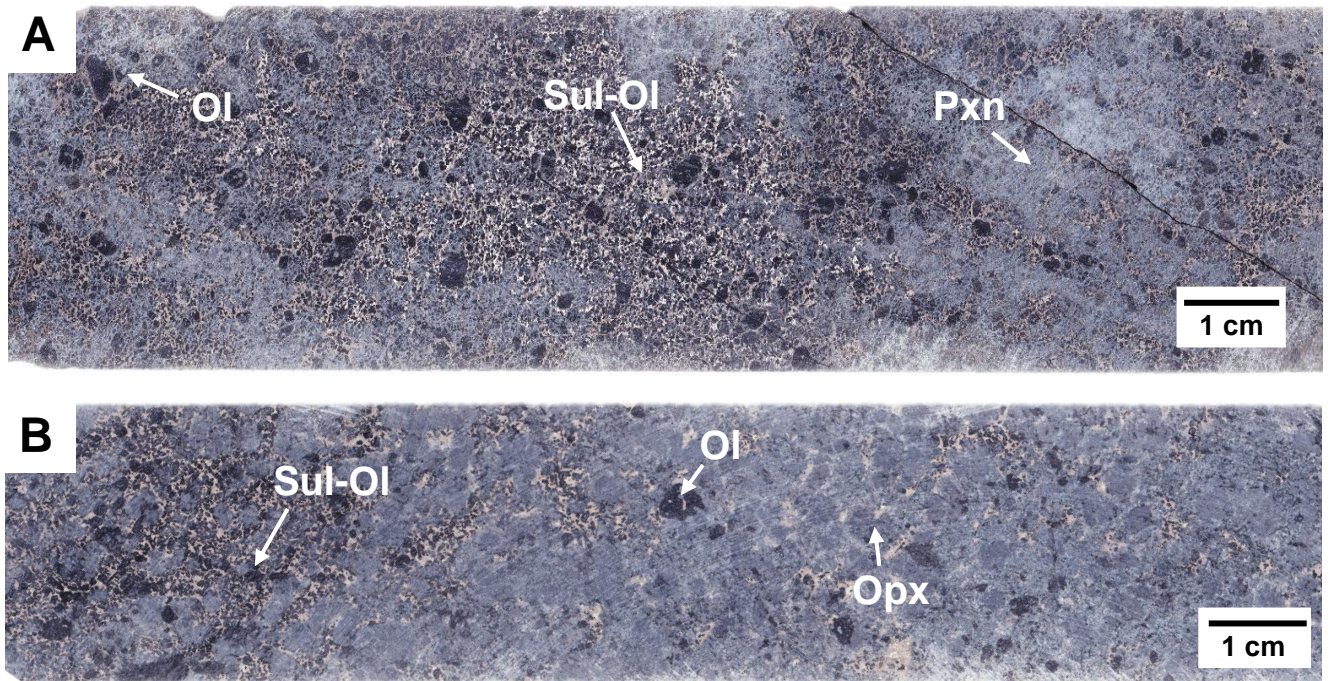


Figure 17.

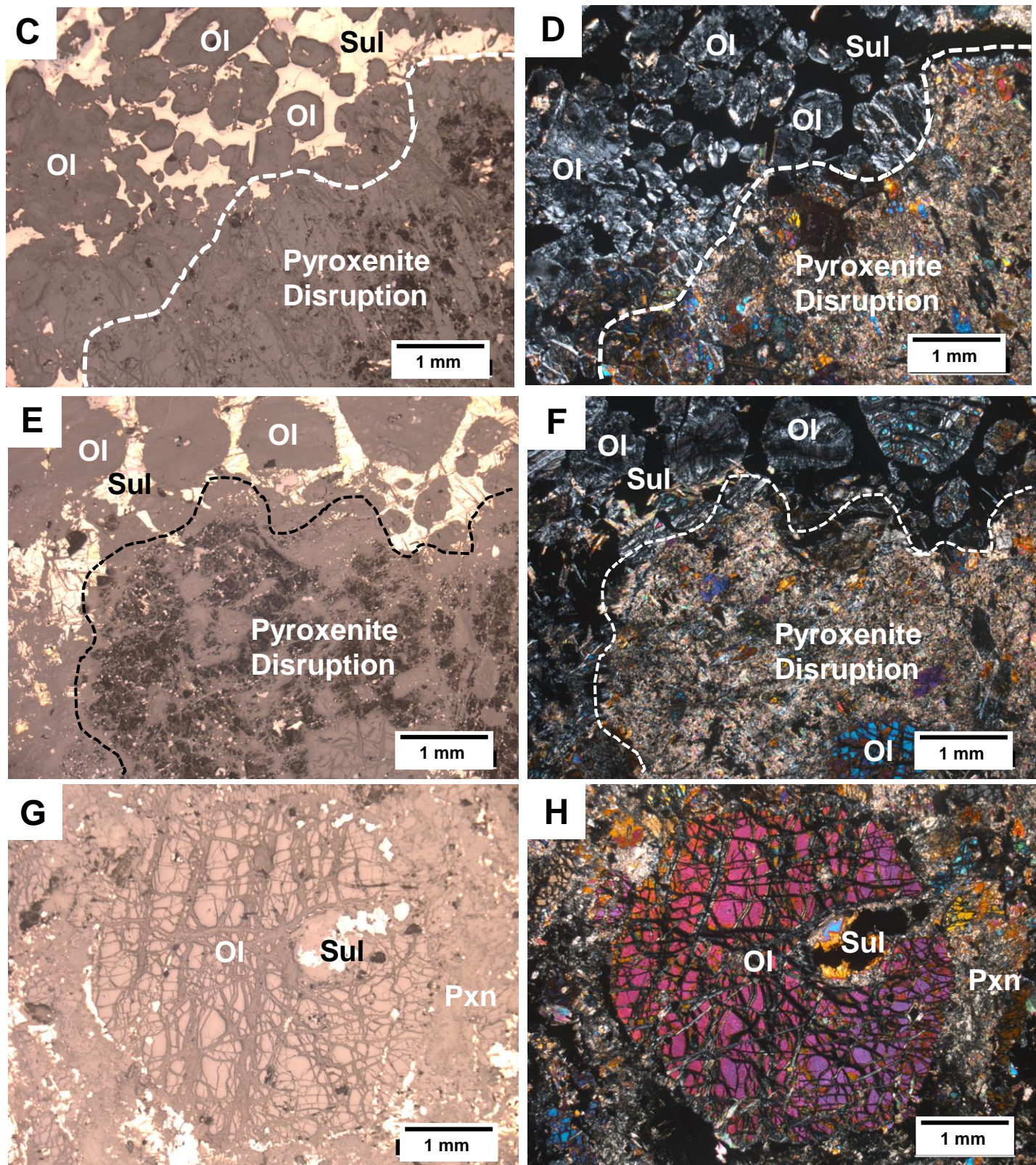


Figure 17 (cont).

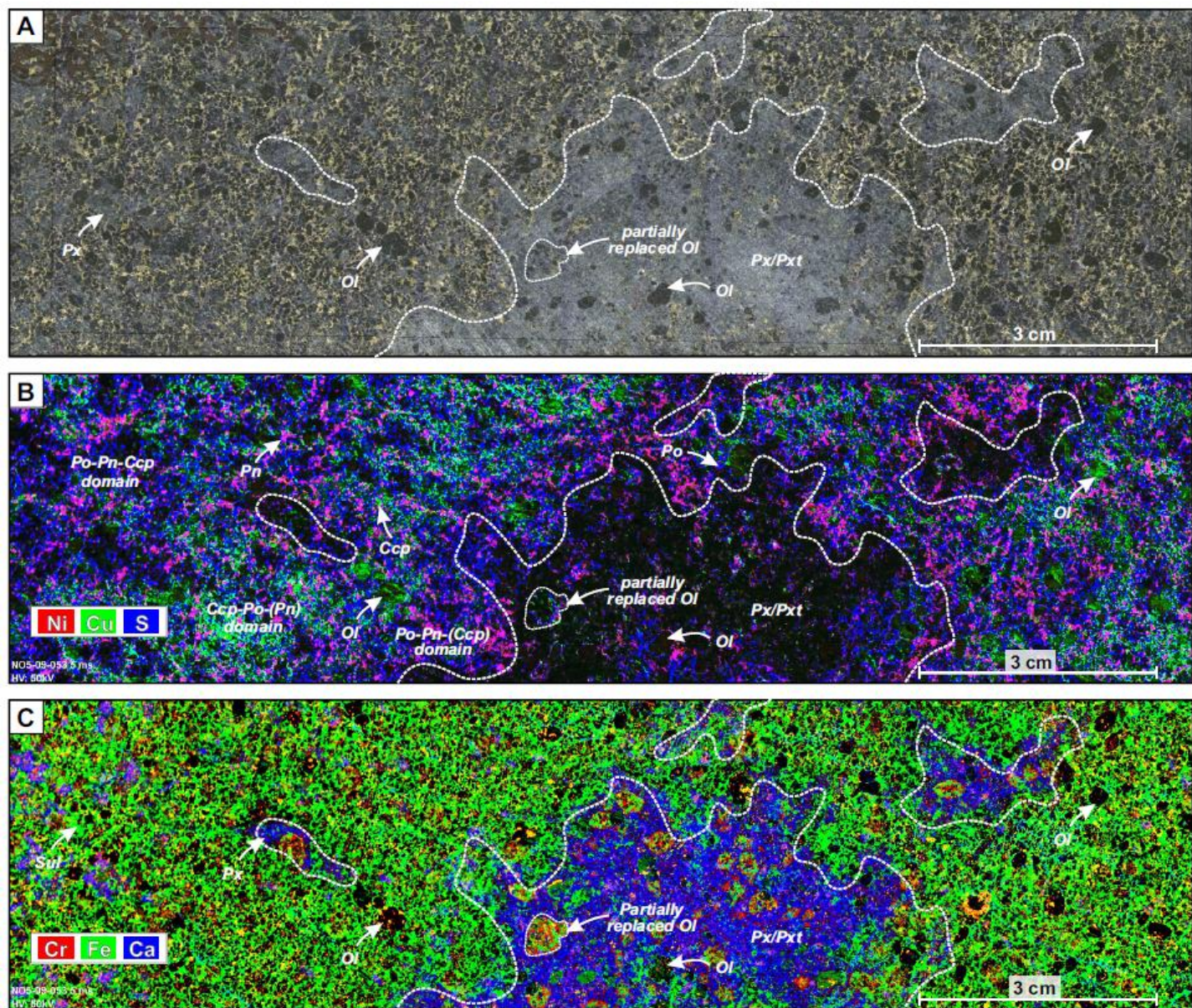


Figure 18.

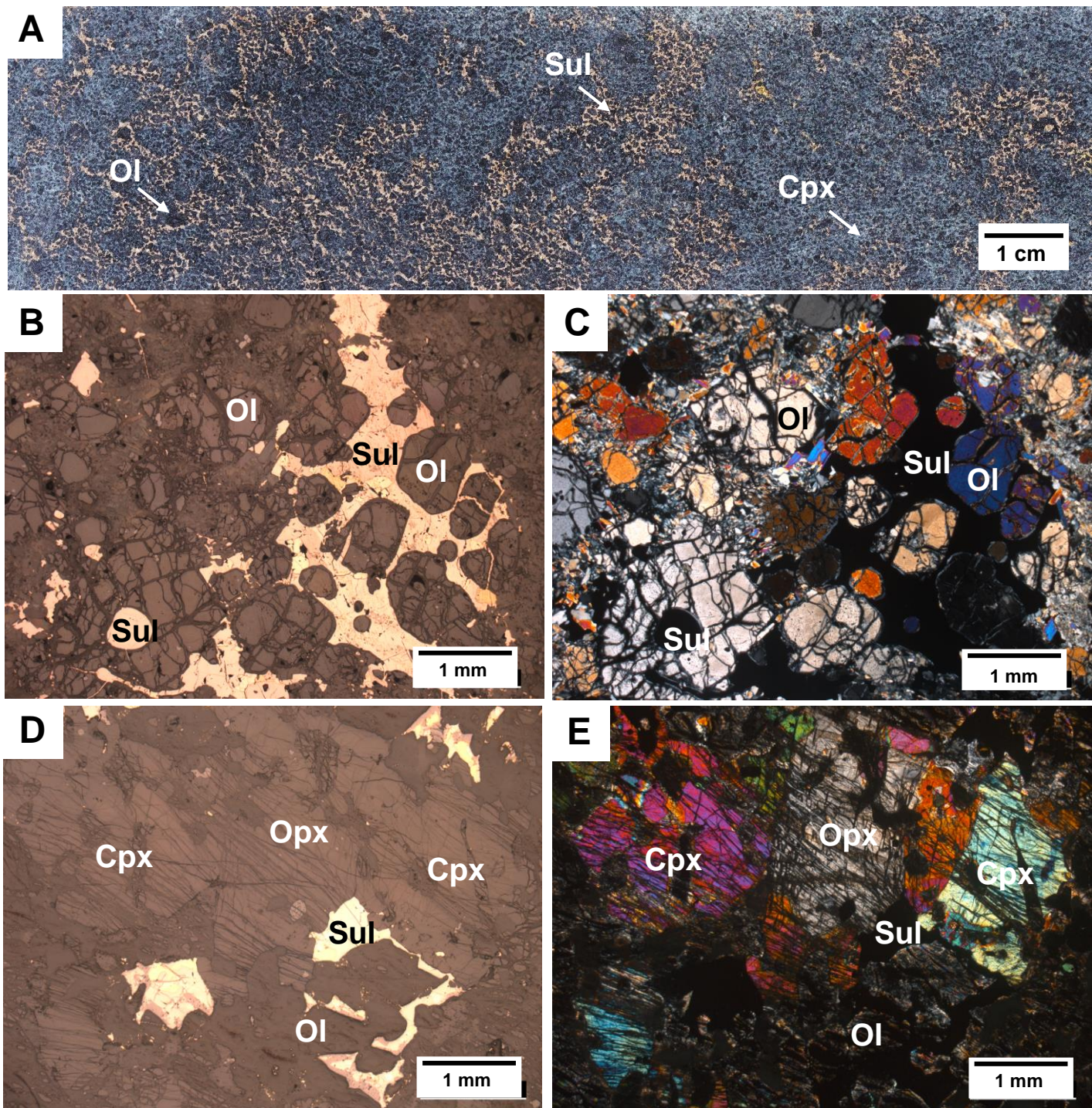


Figure 19.

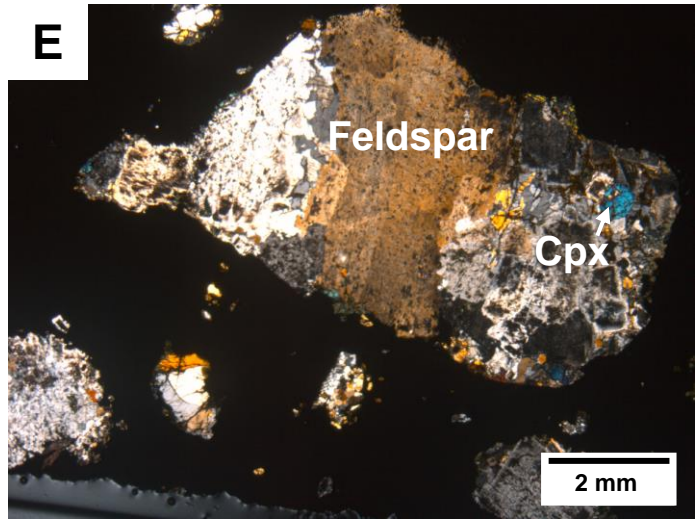
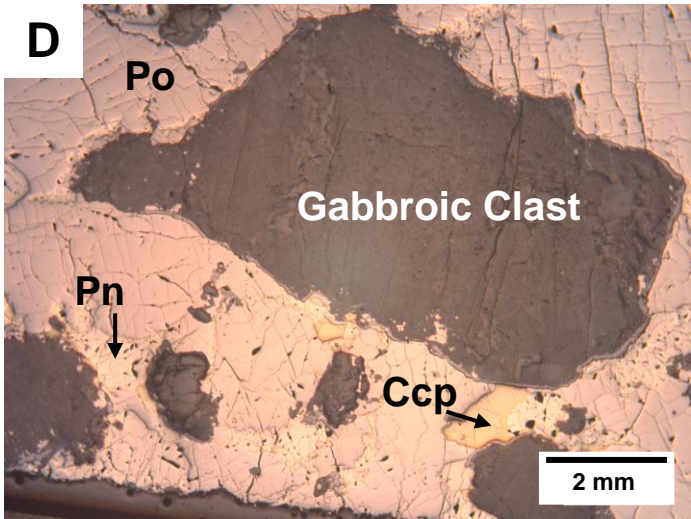
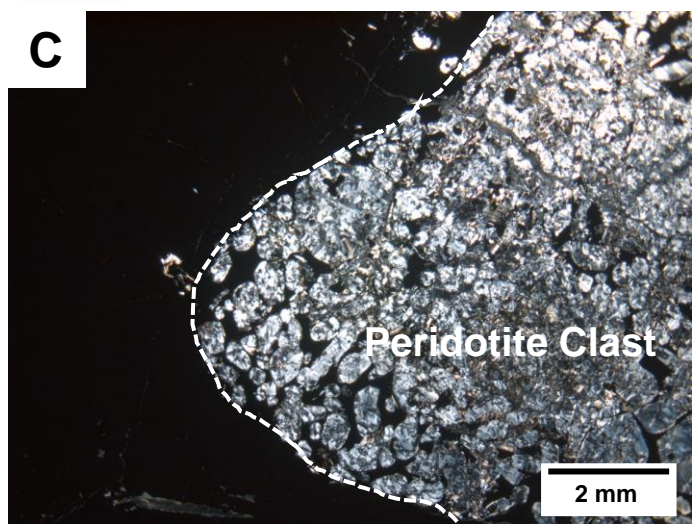
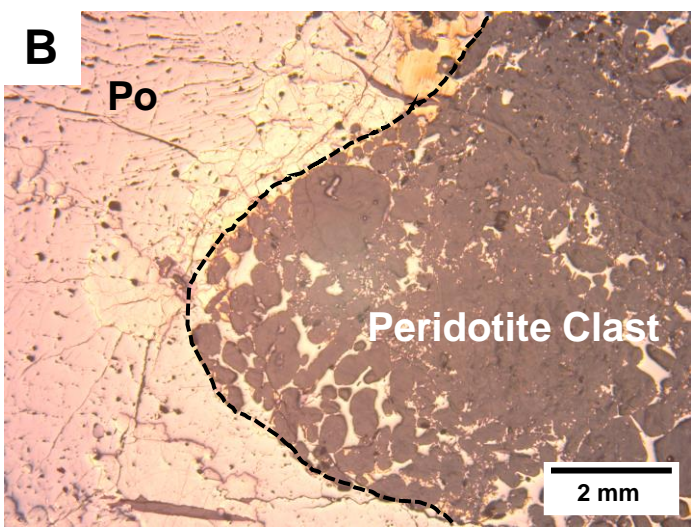
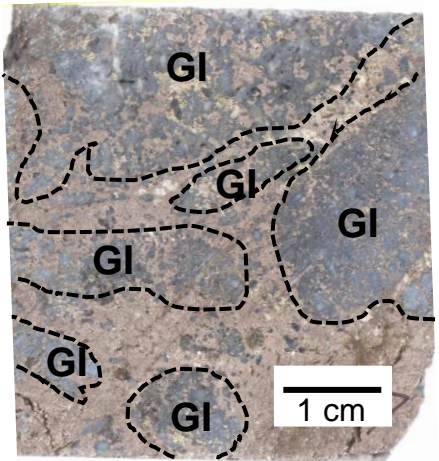
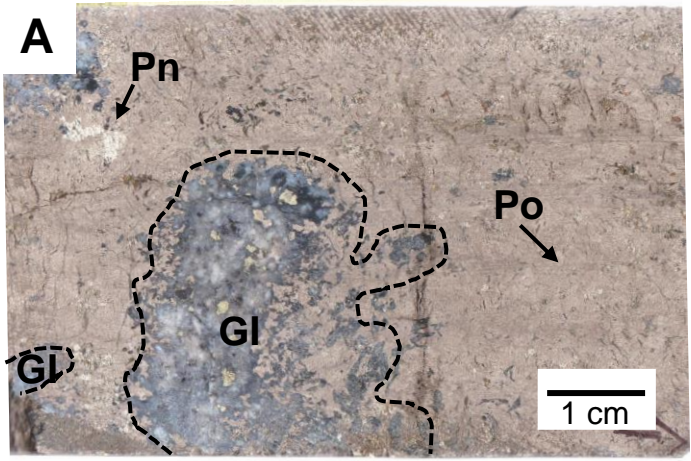


Figure 20.

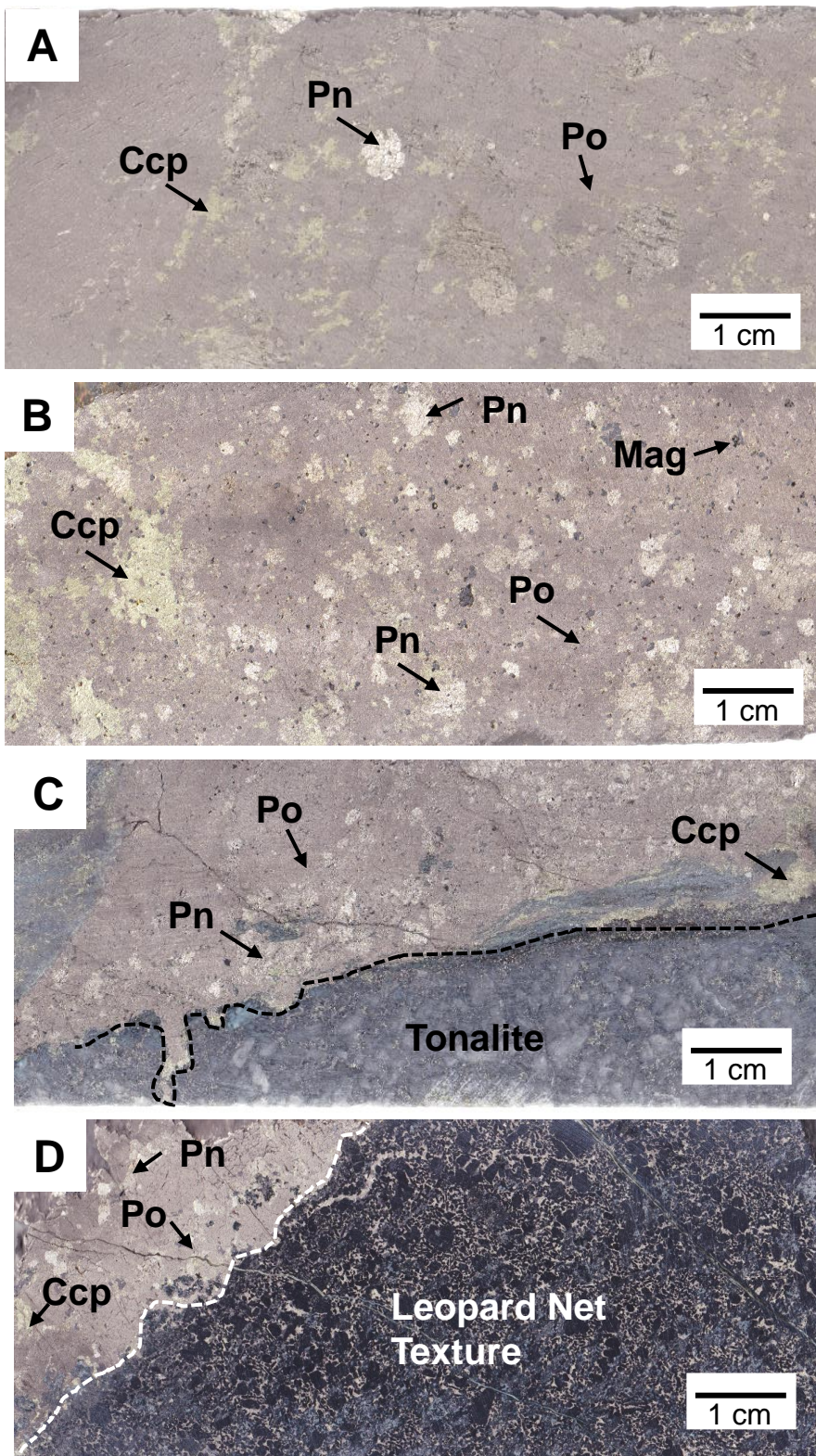


Figure 21.

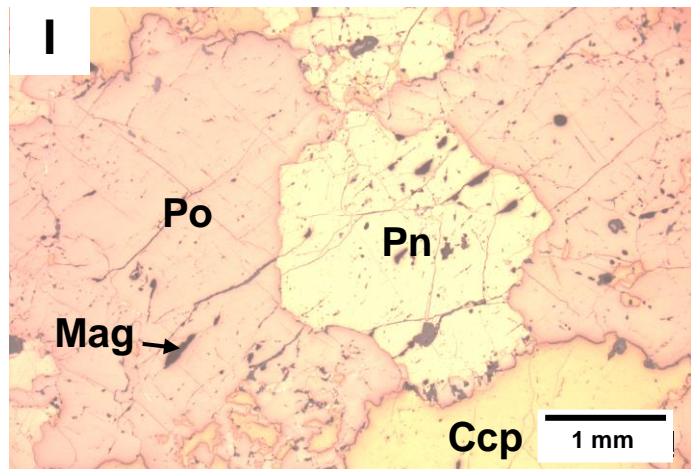
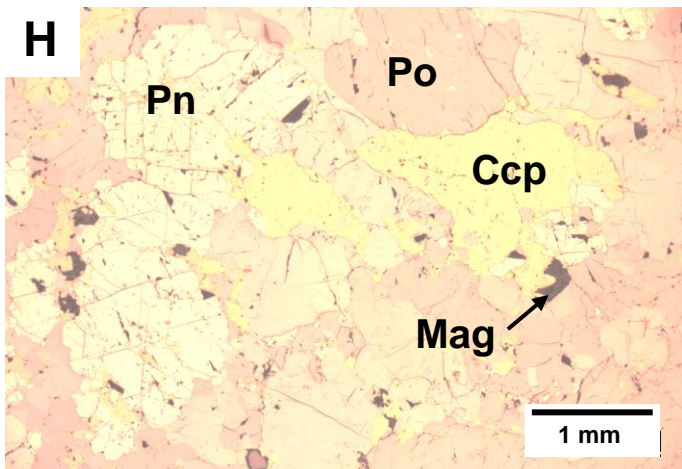
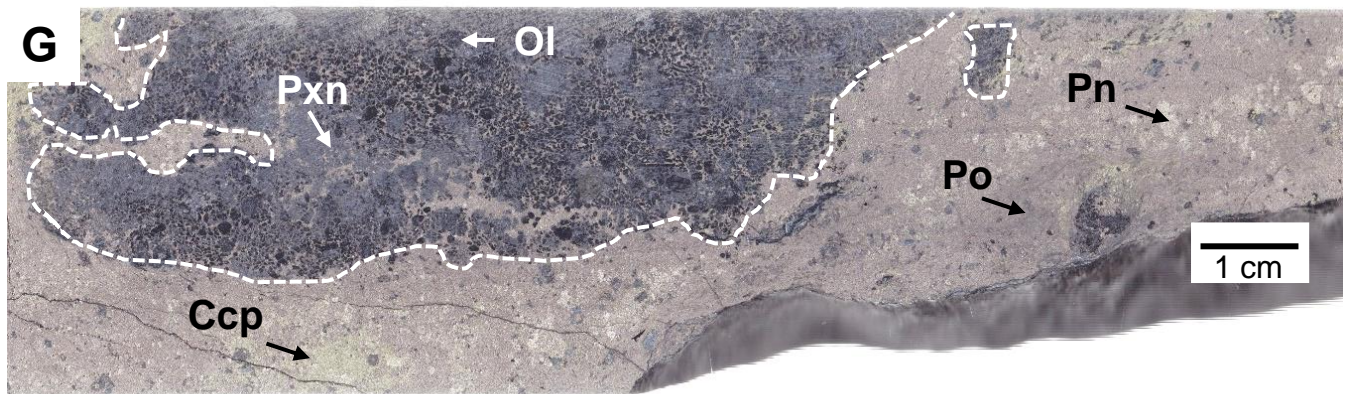
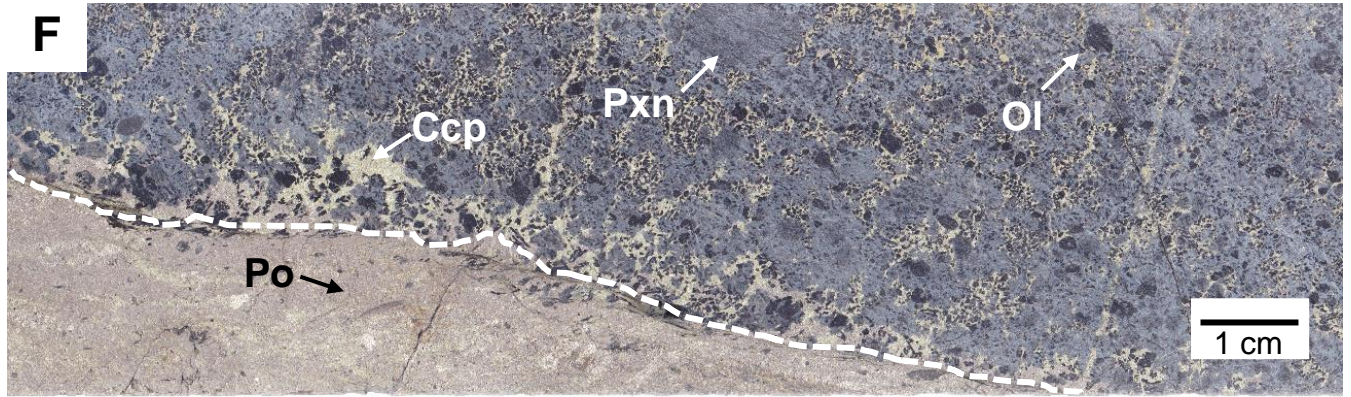
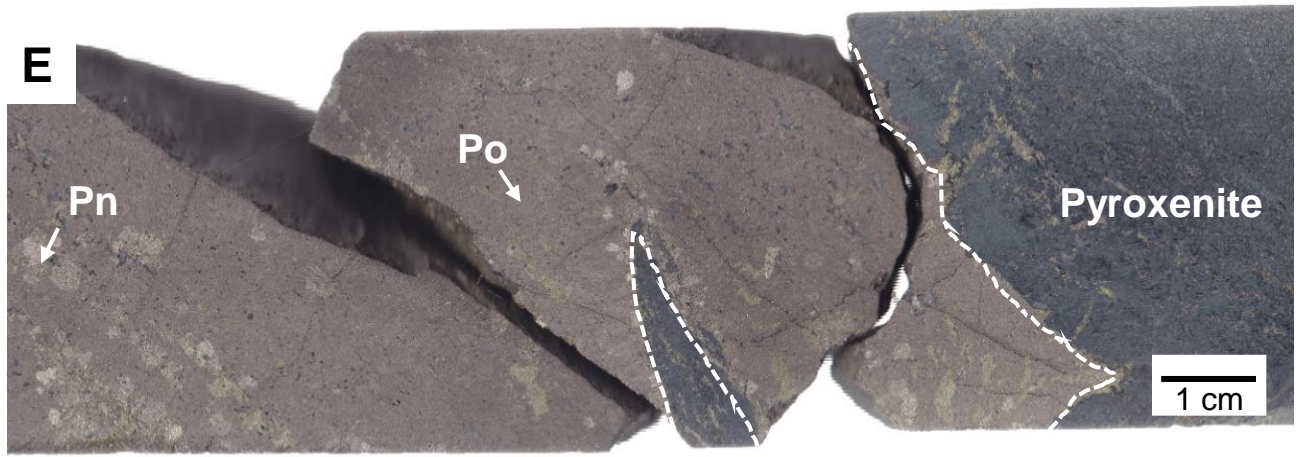


Figure 21 (cont).

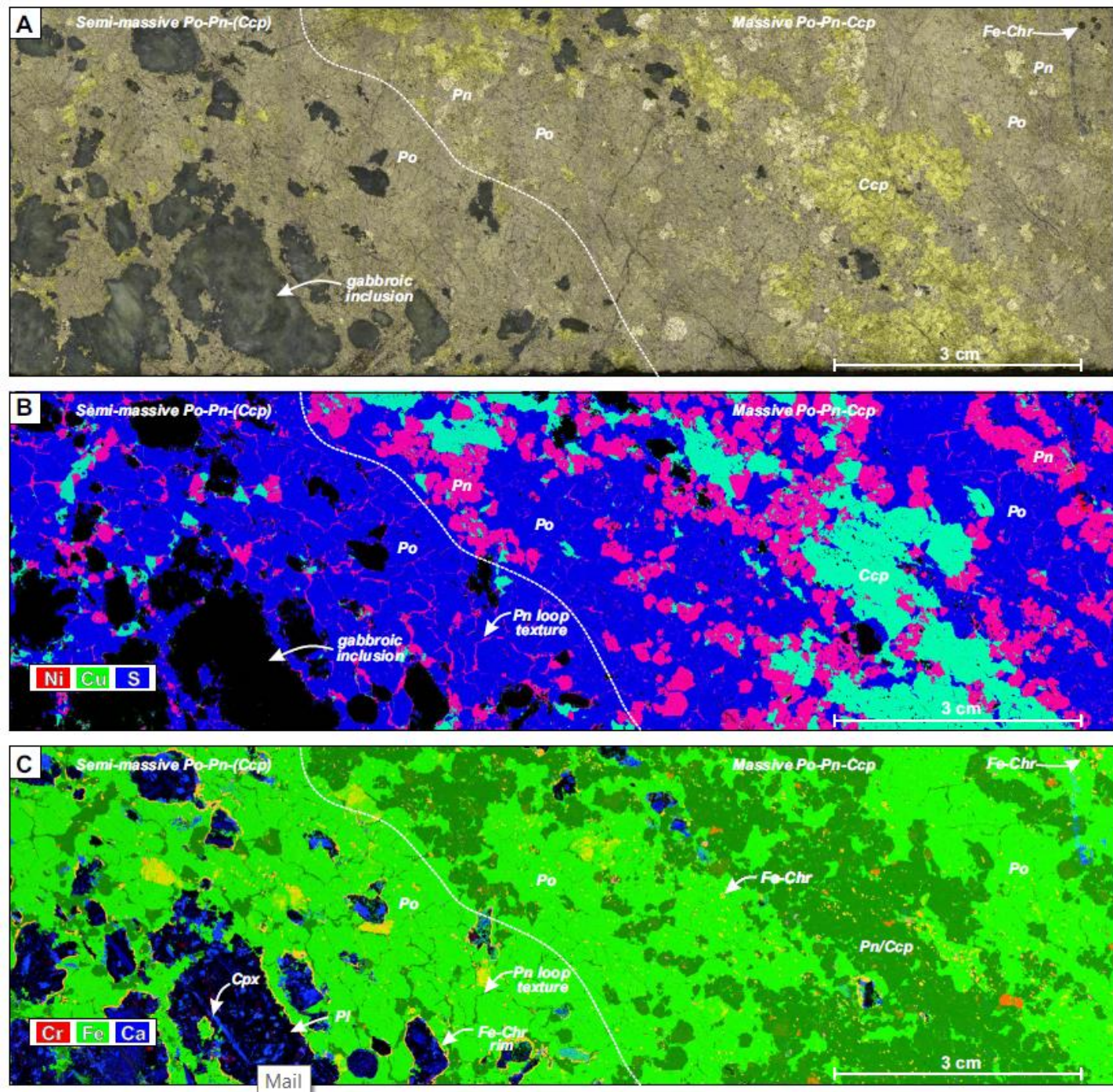


Figure 22.

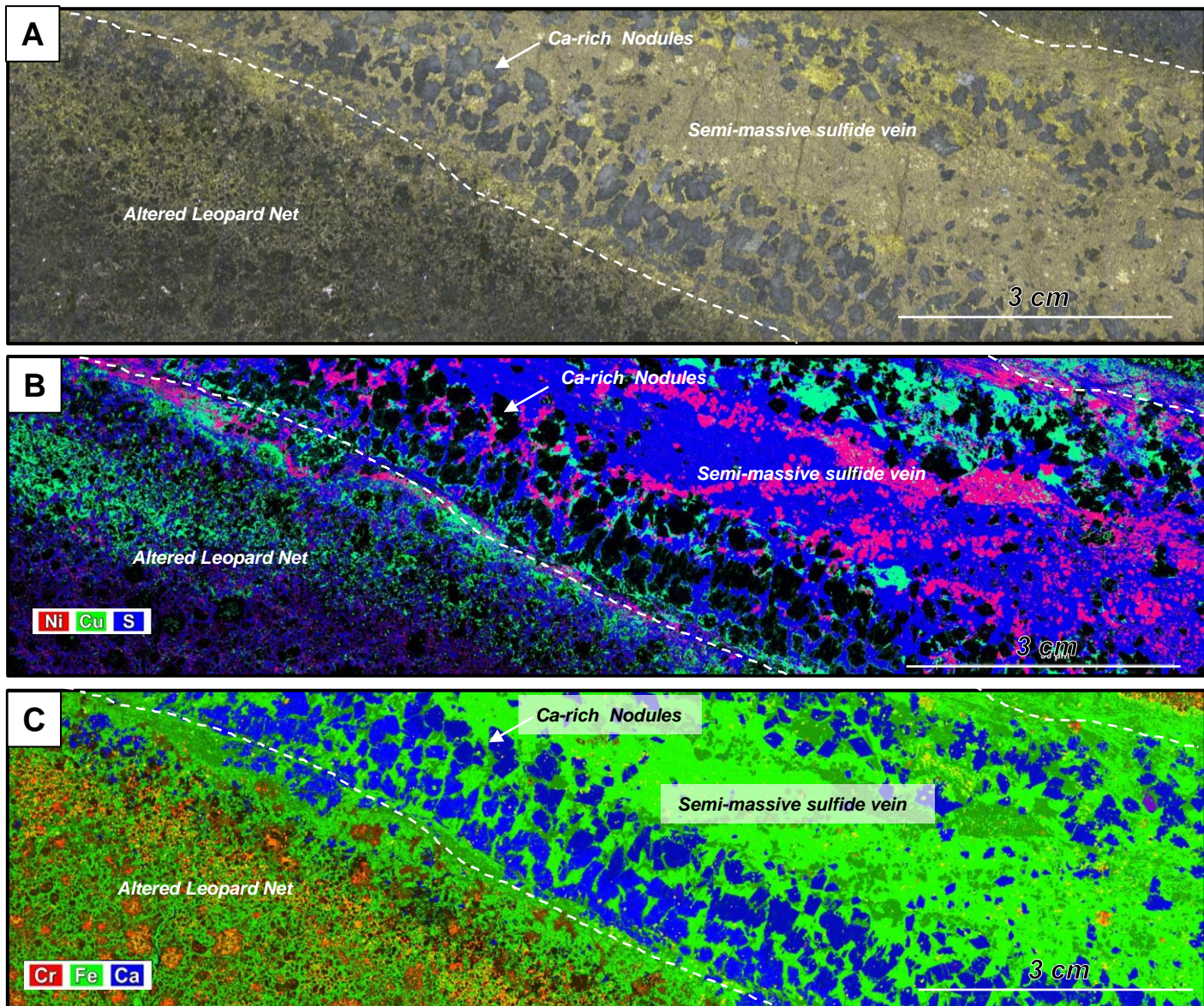


Figure 23.

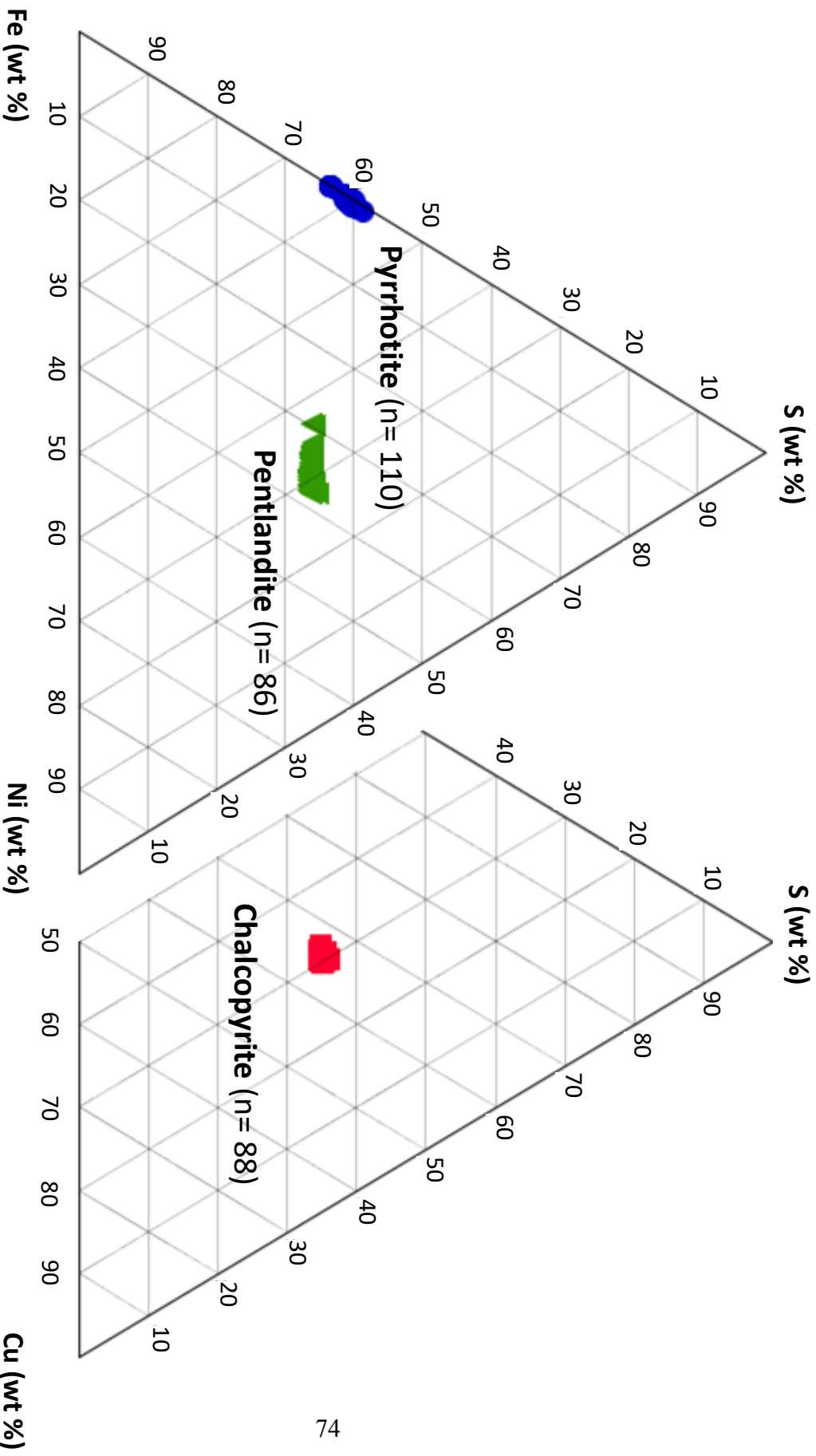


Figure 24.

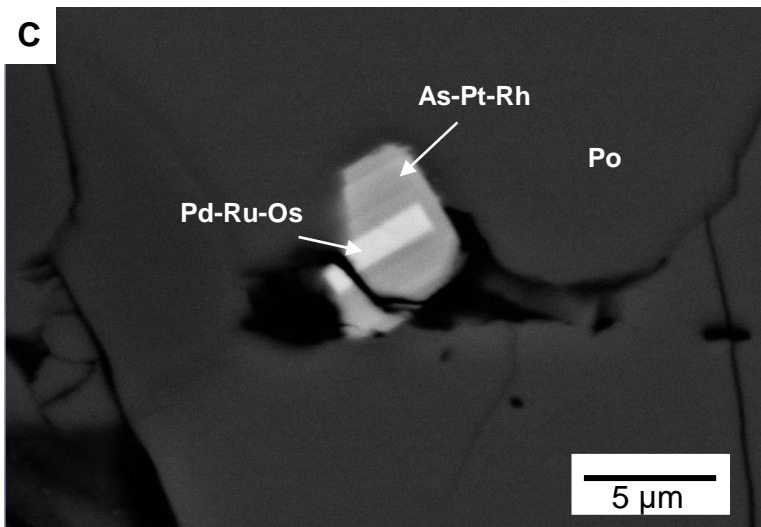
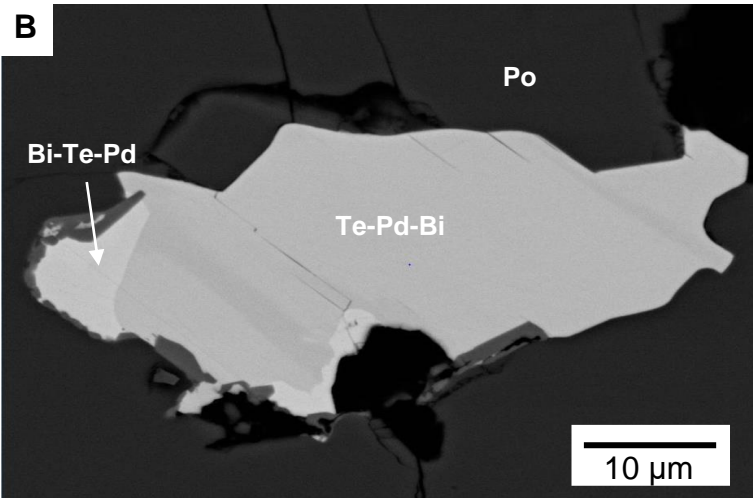
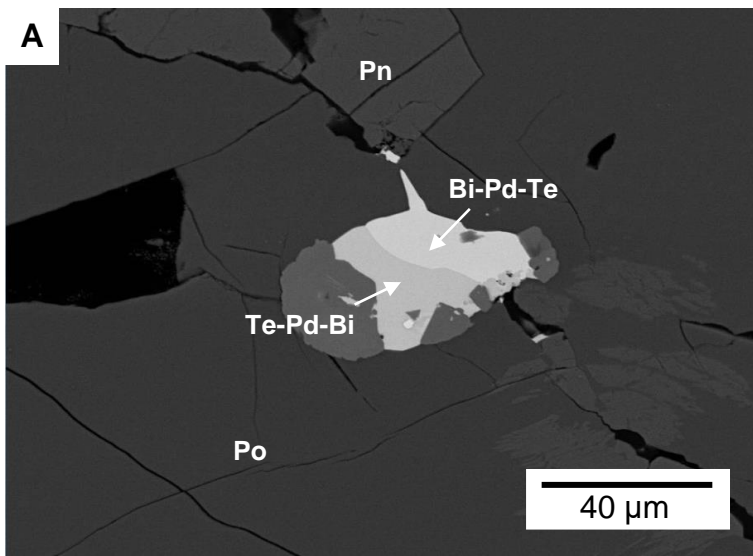


Figure 25.

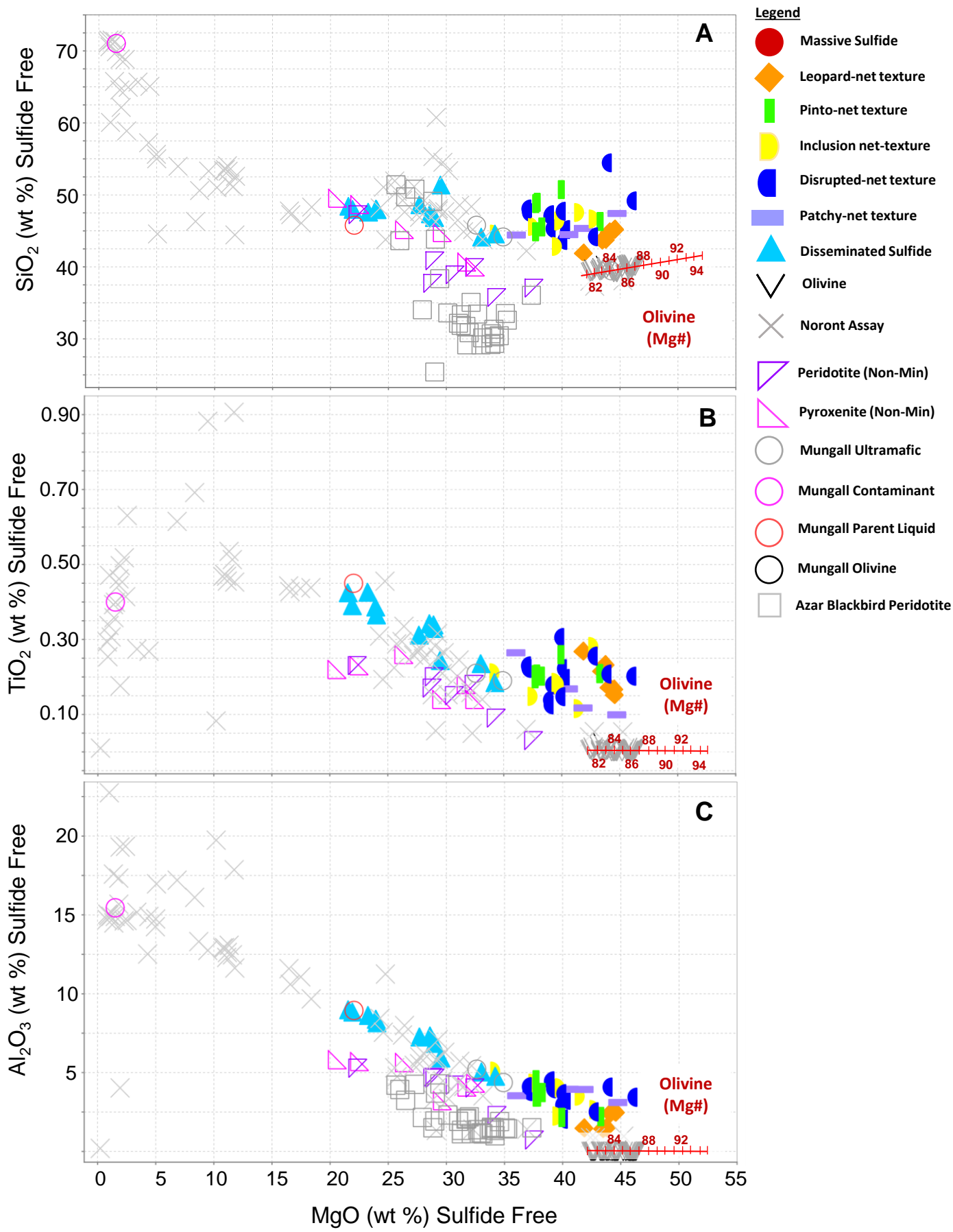


Figure 26.

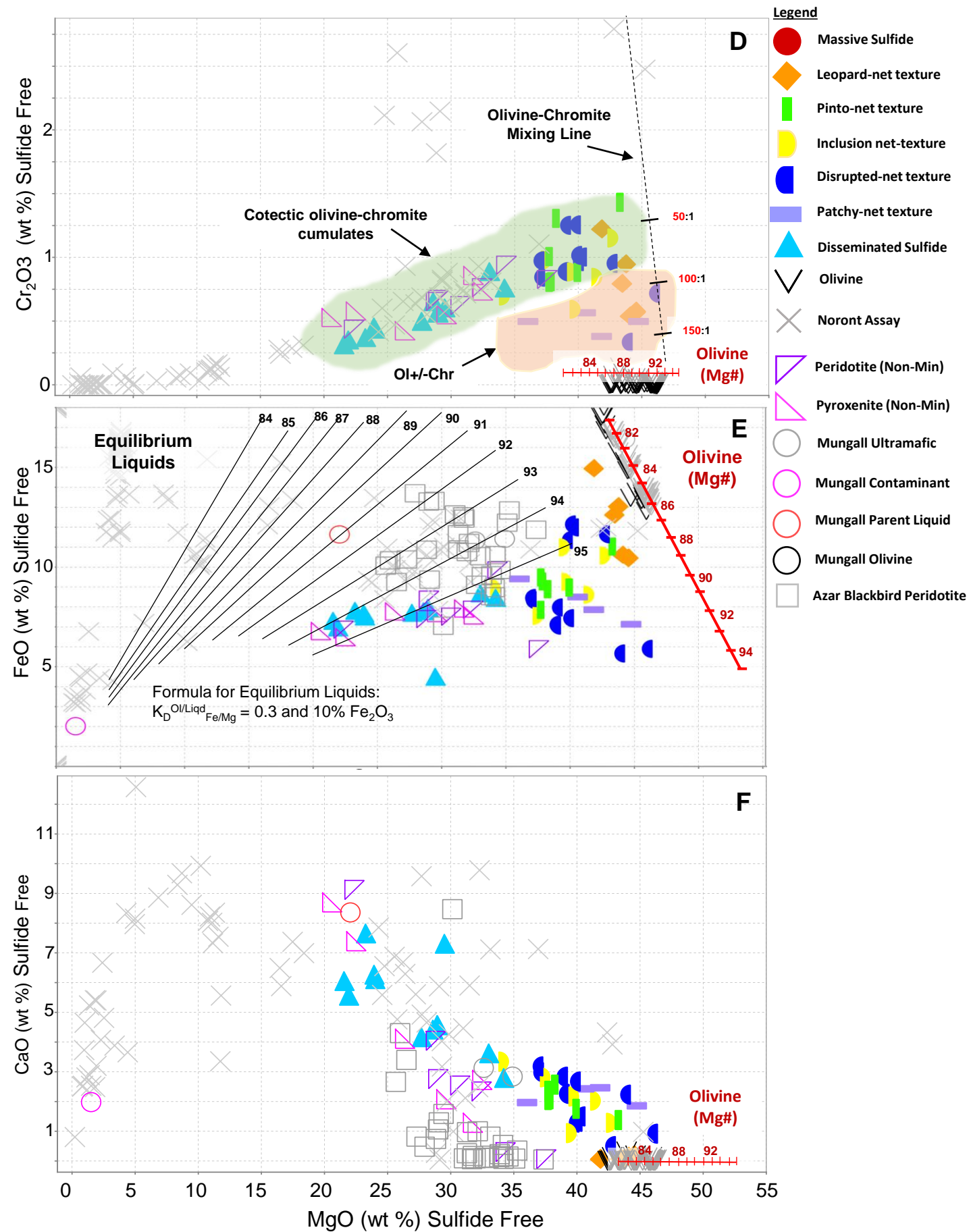


Figure 26 (cont).

Primitive Mantle Normalized Abundance
(Sun and McDonough, 1989)

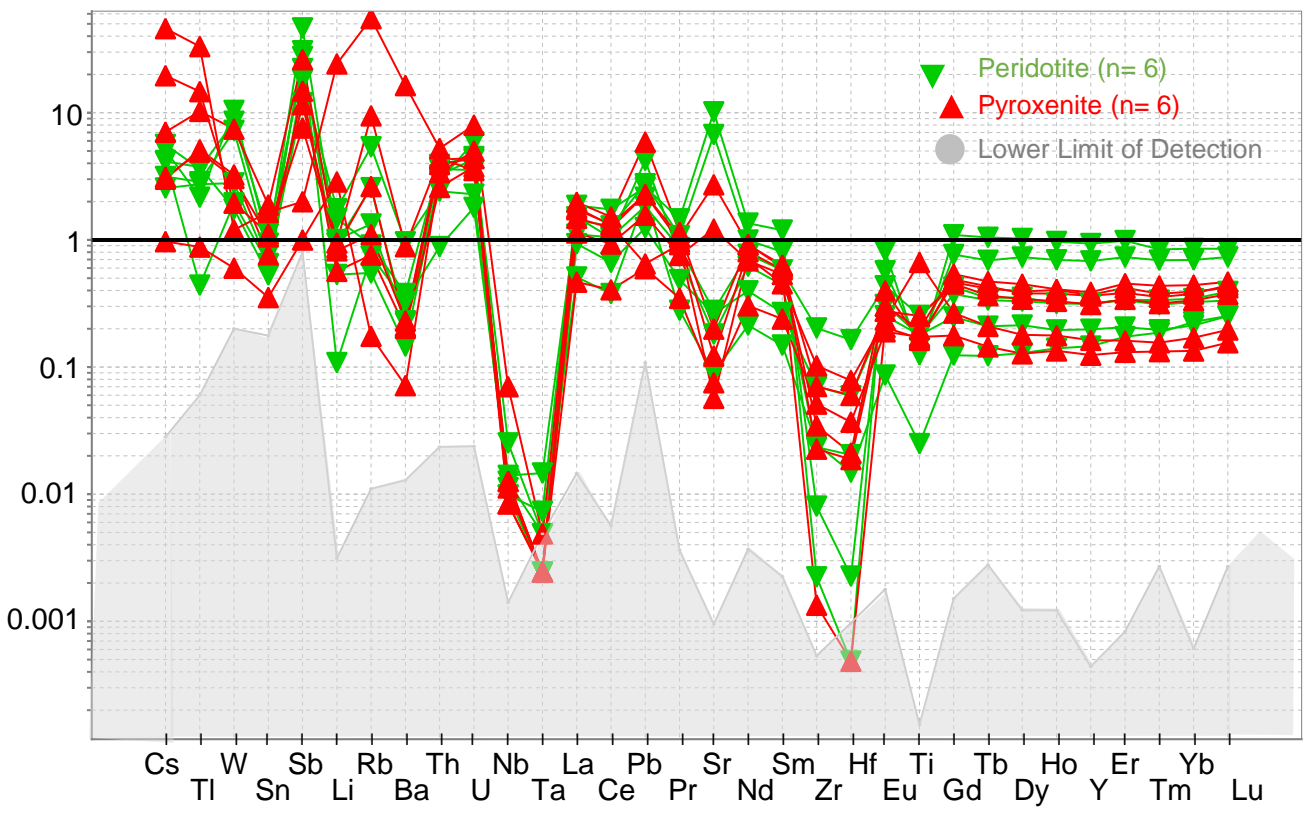


Figure 27.

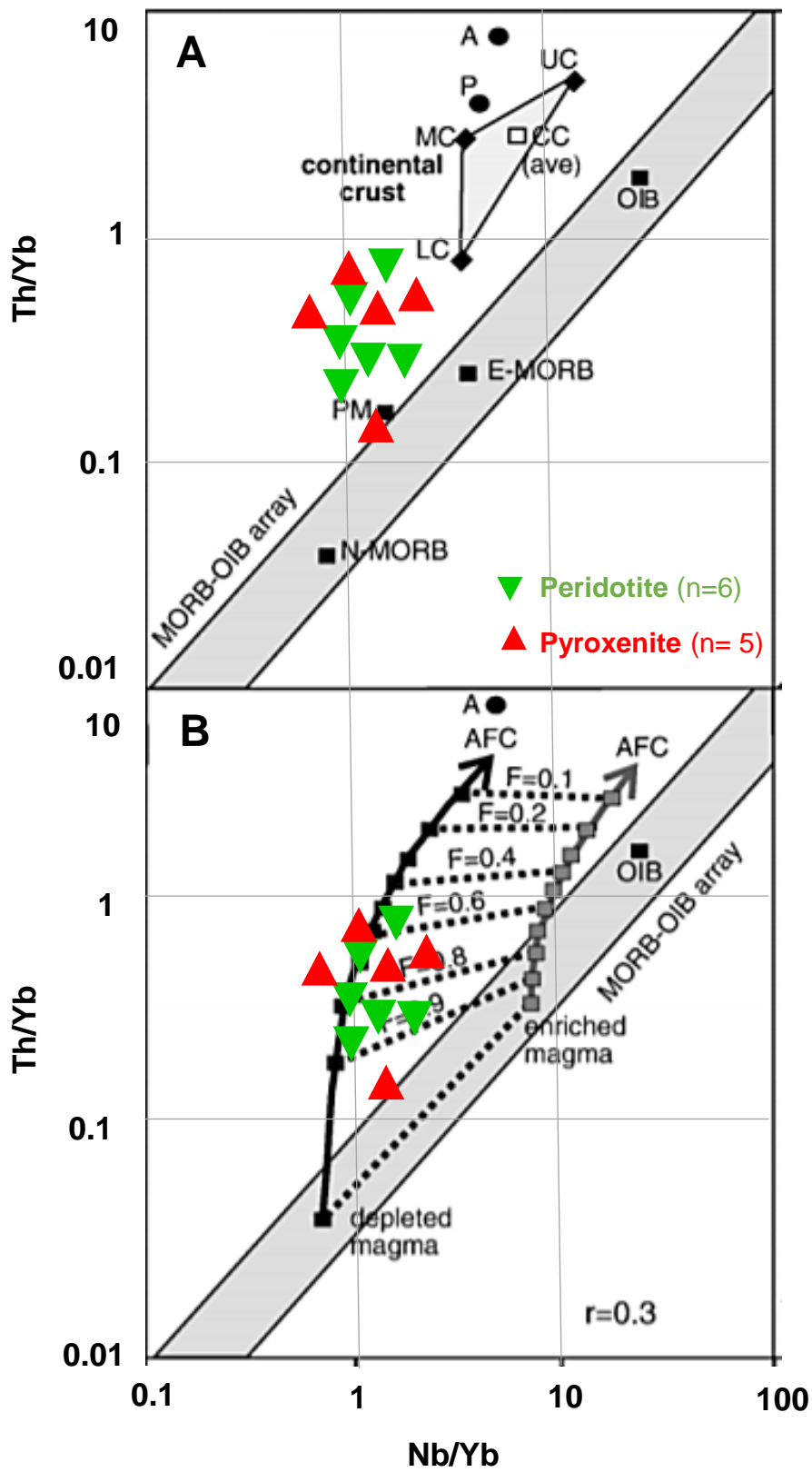


Figure 28.

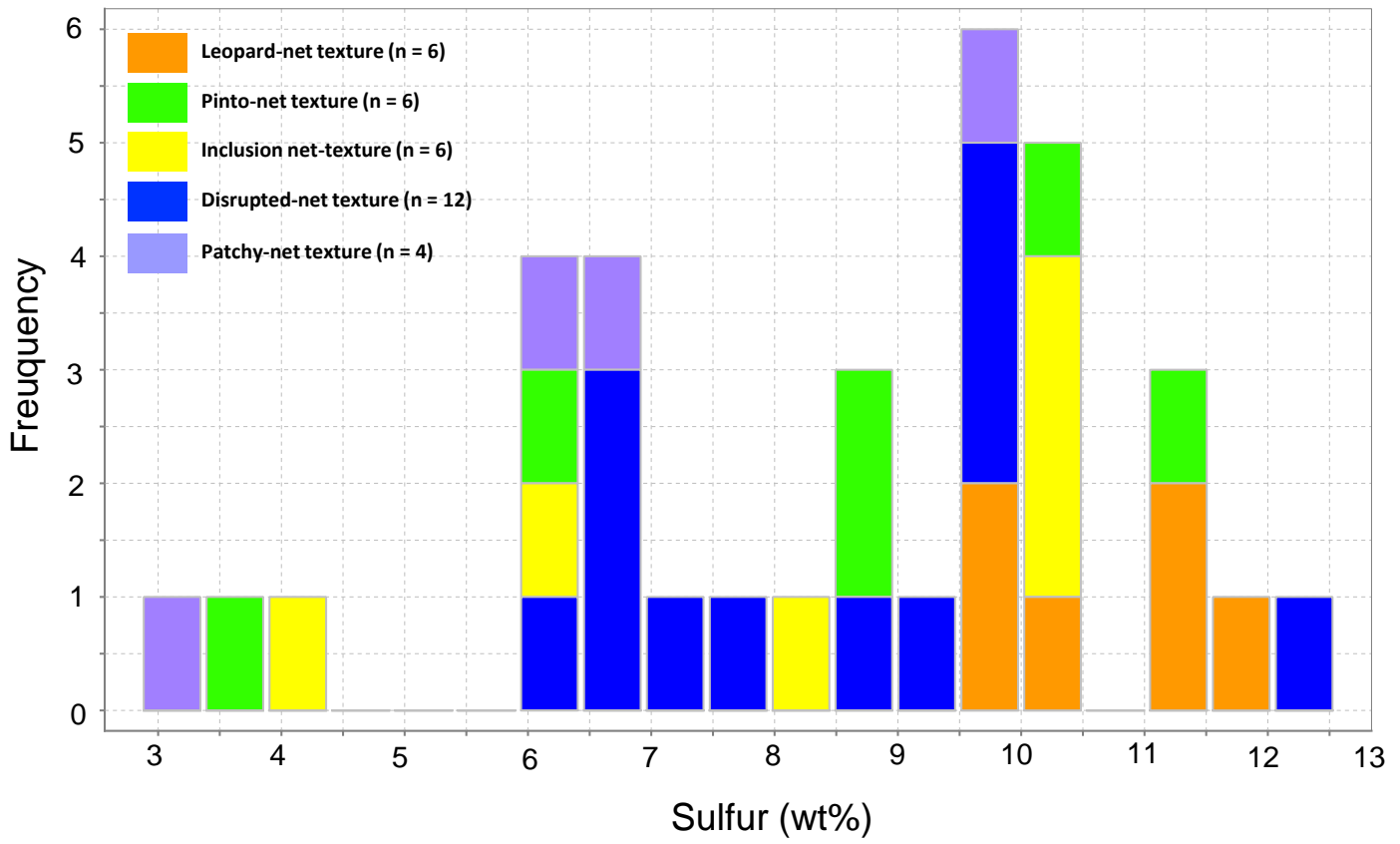


Figure 29.

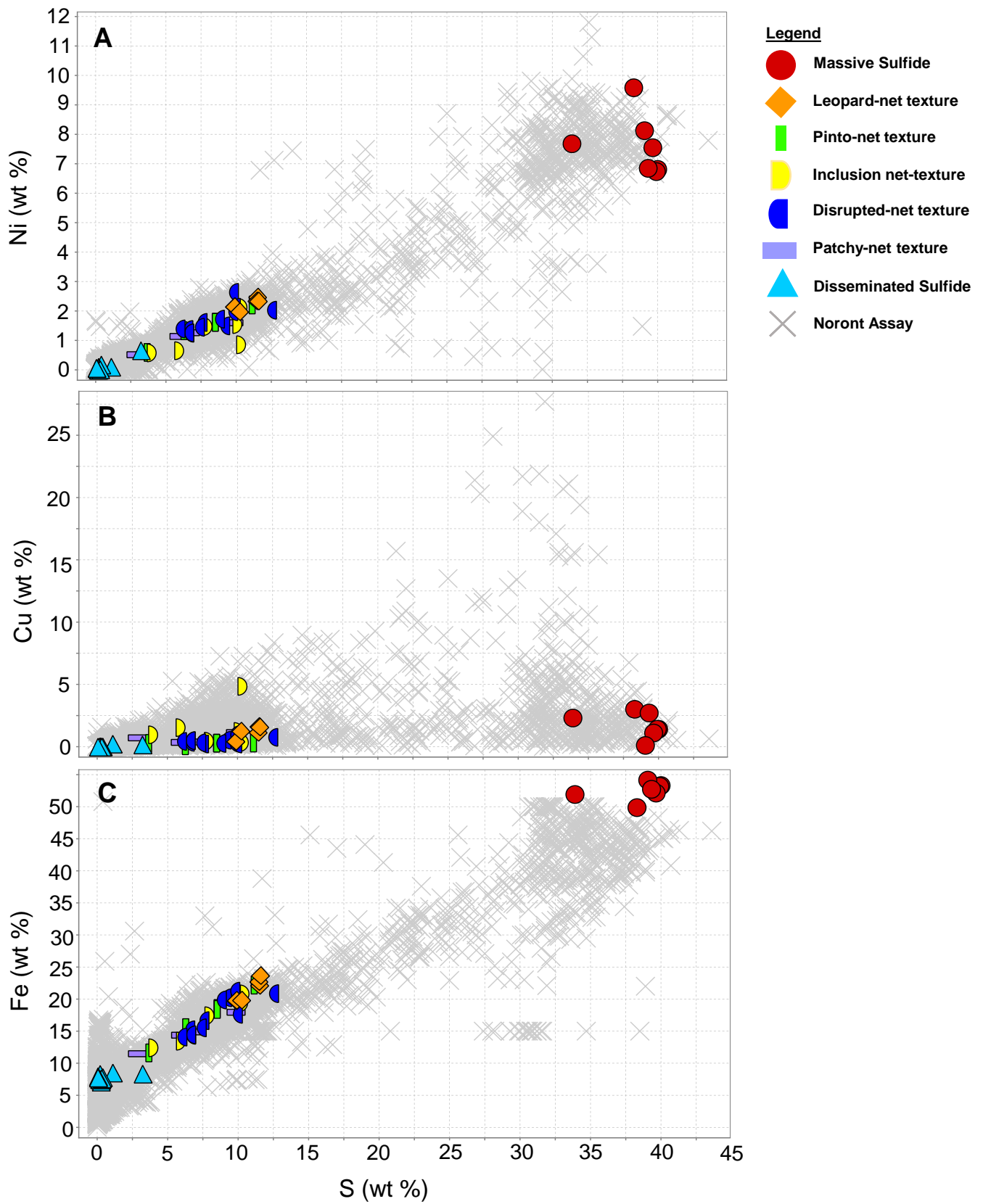


Figure 30.

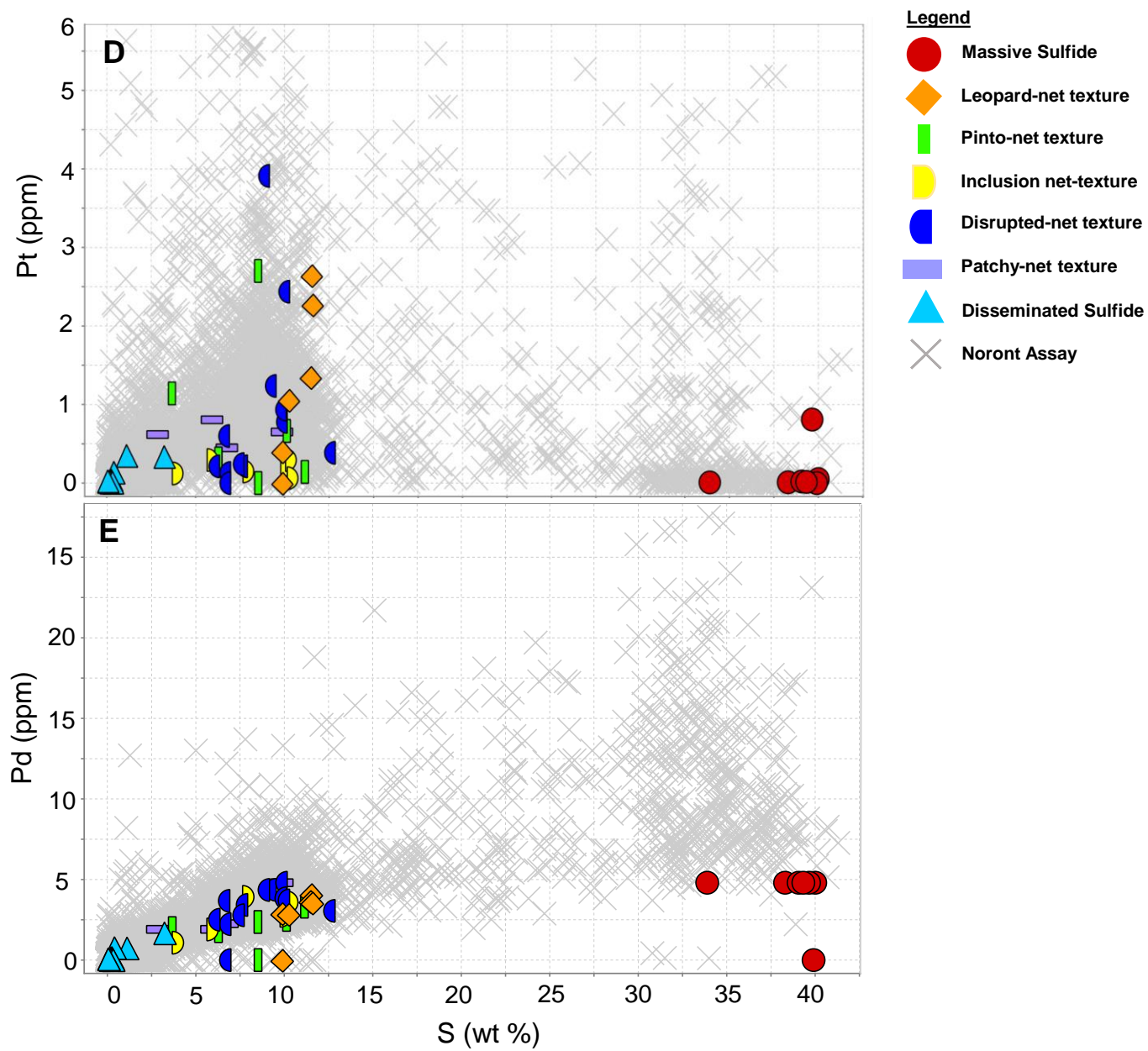


Figure 30 (cont).

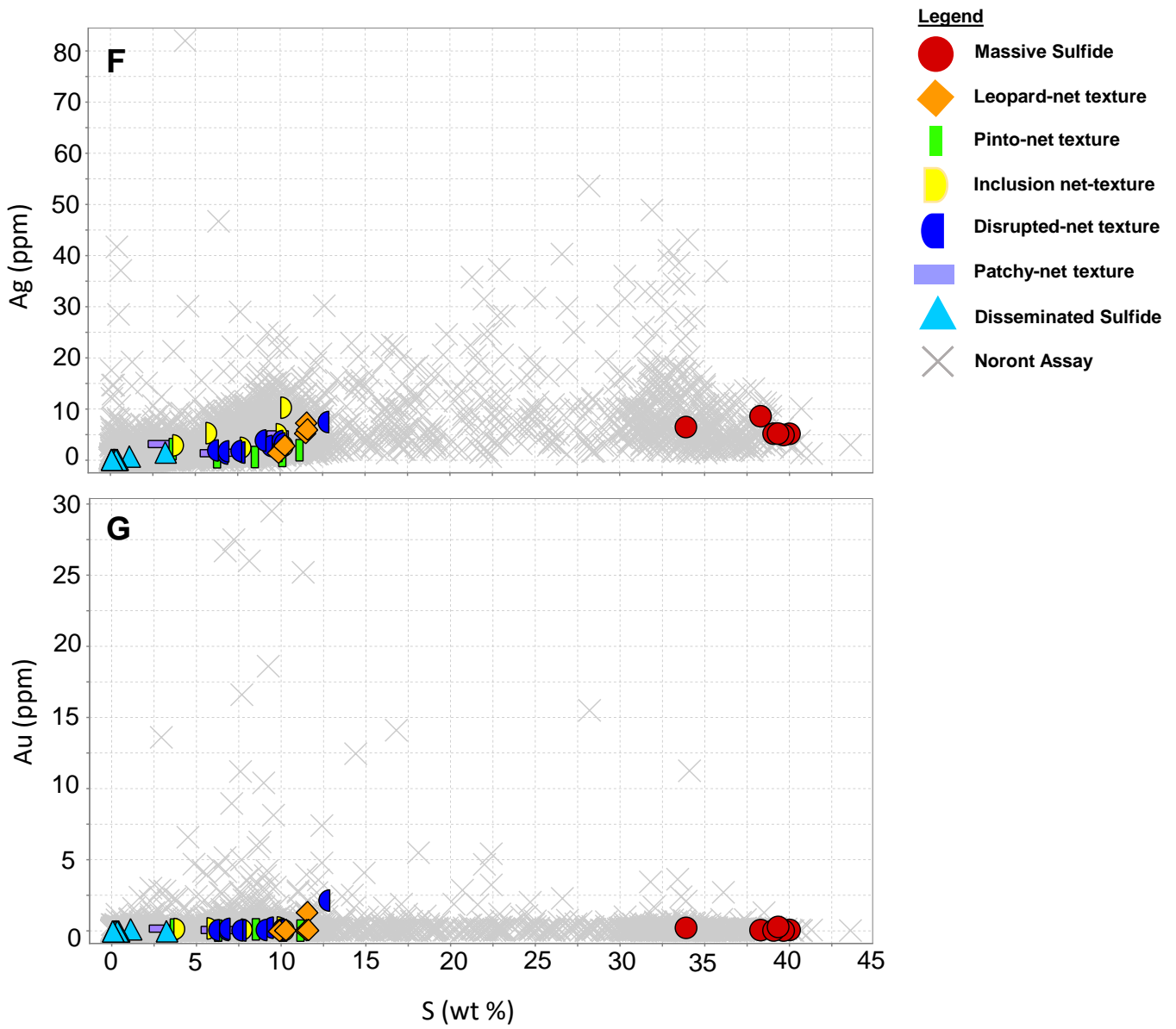


Figure 30 (cont).

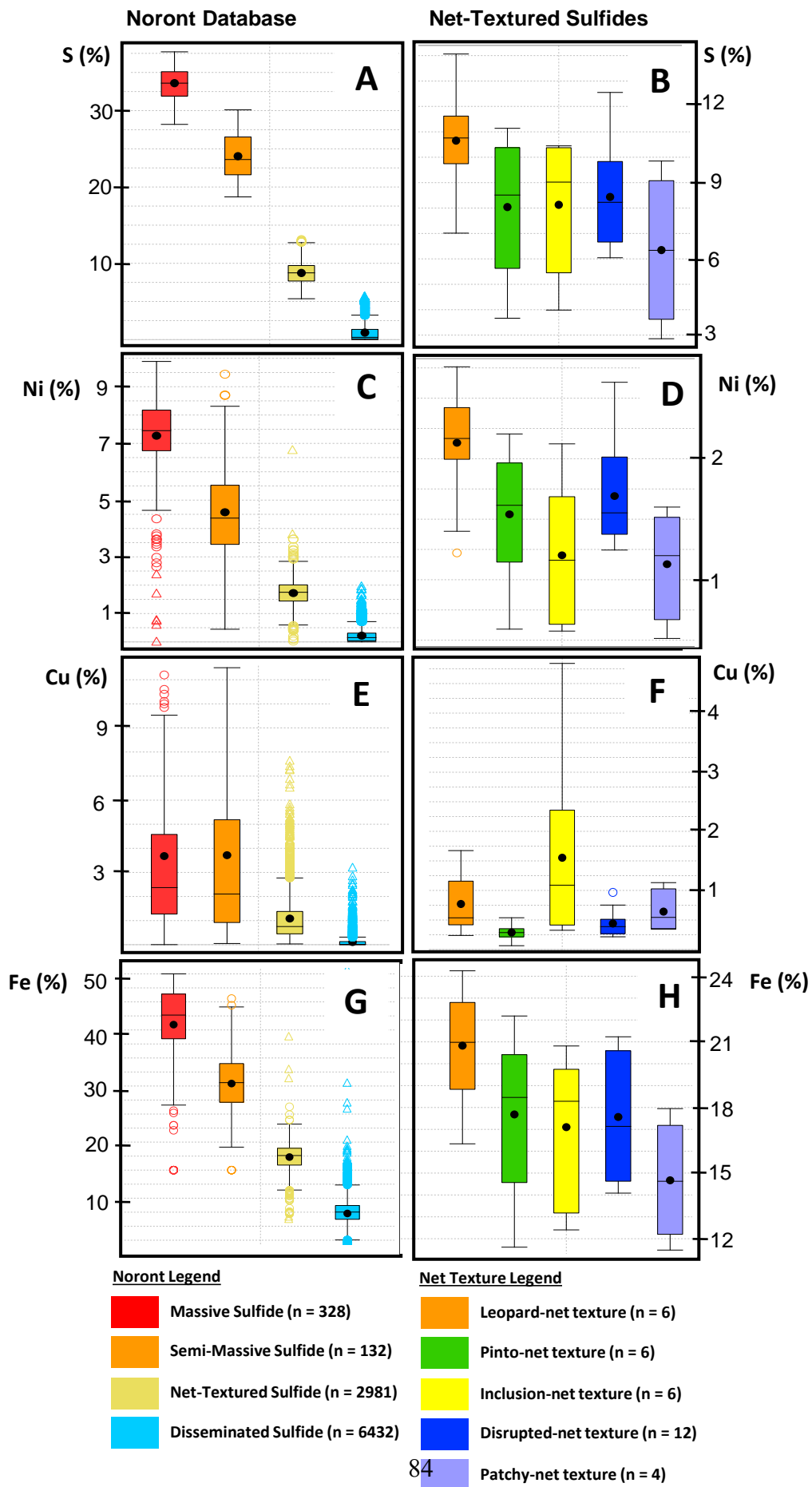


Figure 31.

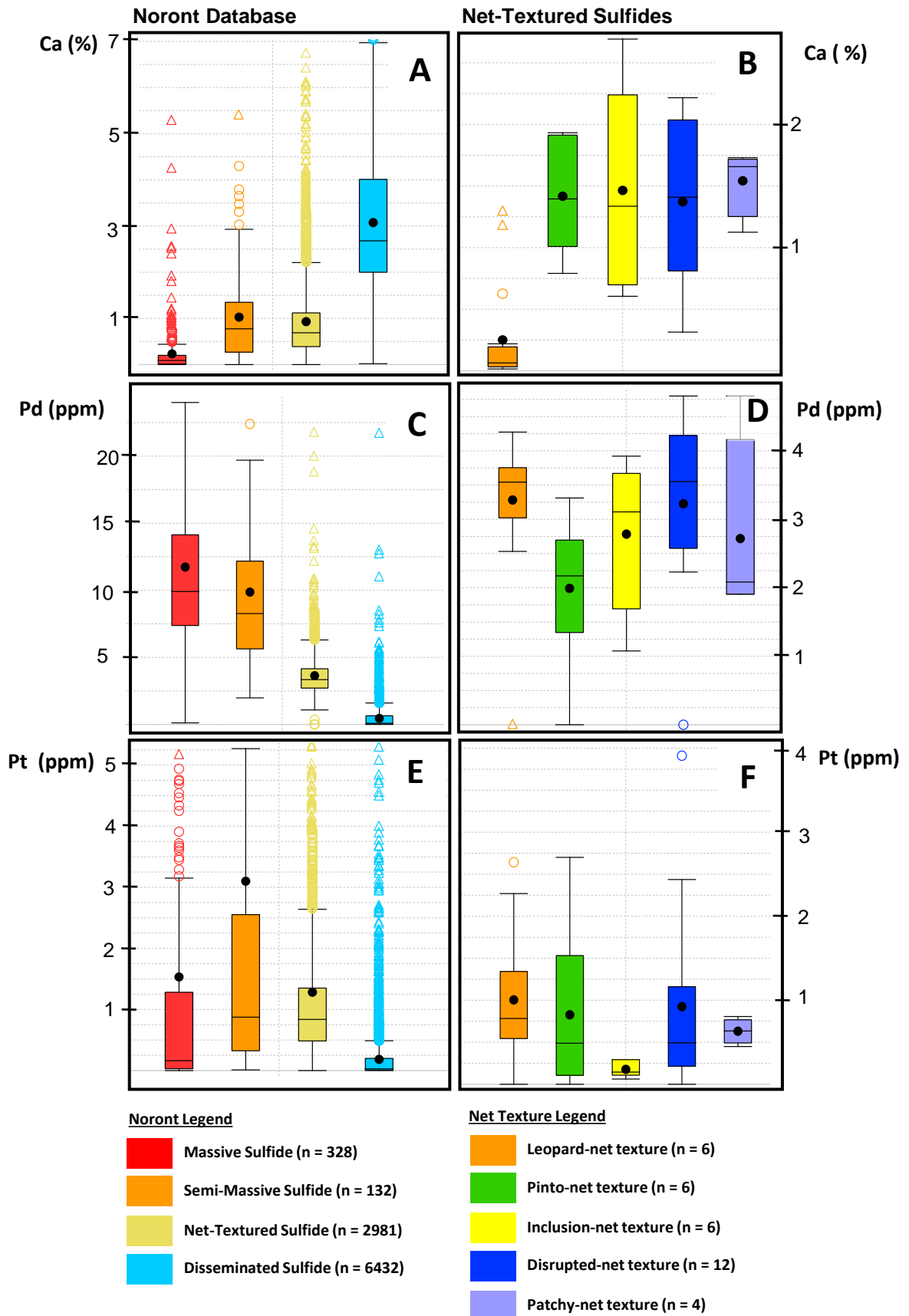


Figure 32.

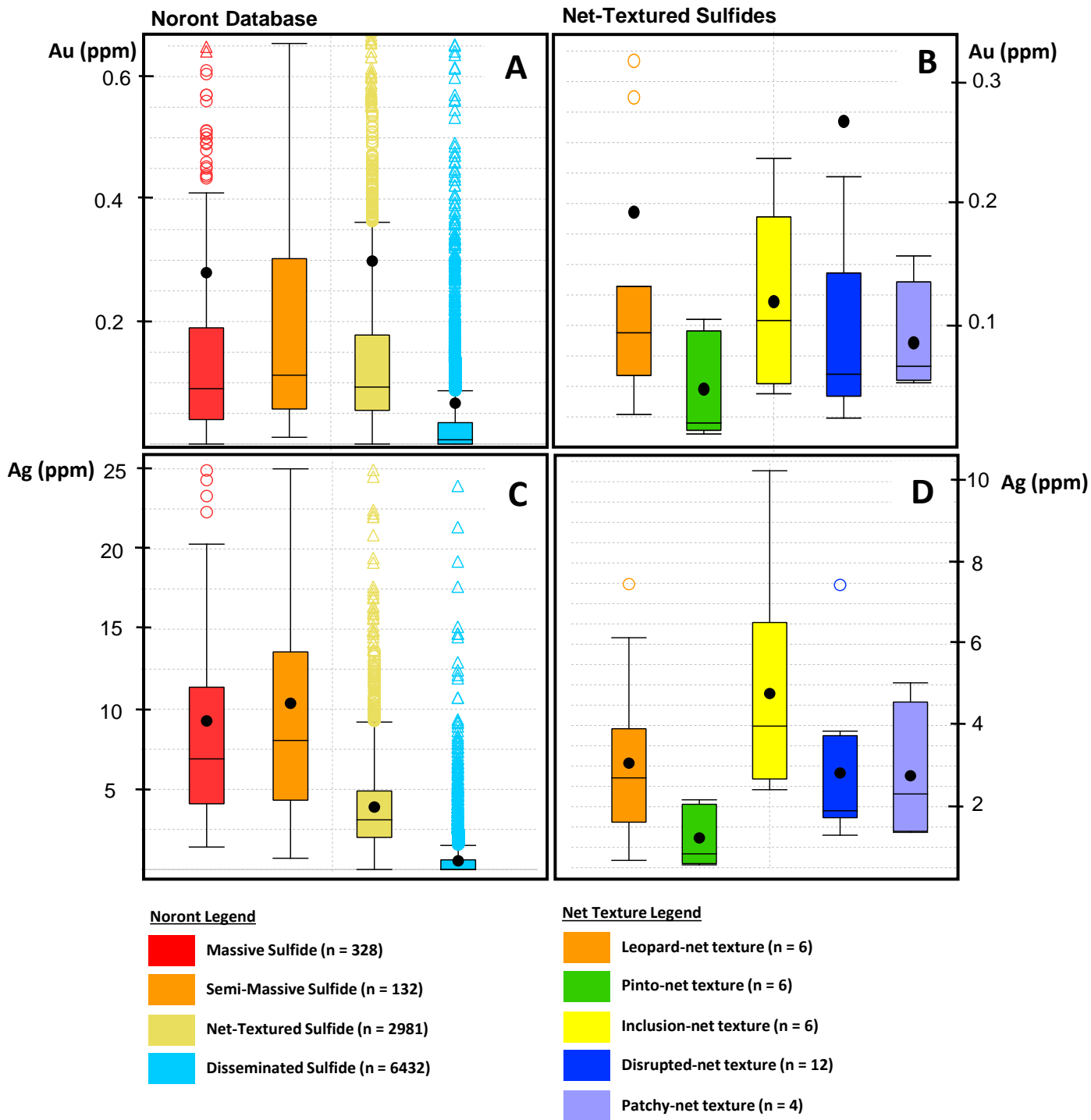


Figure 33.

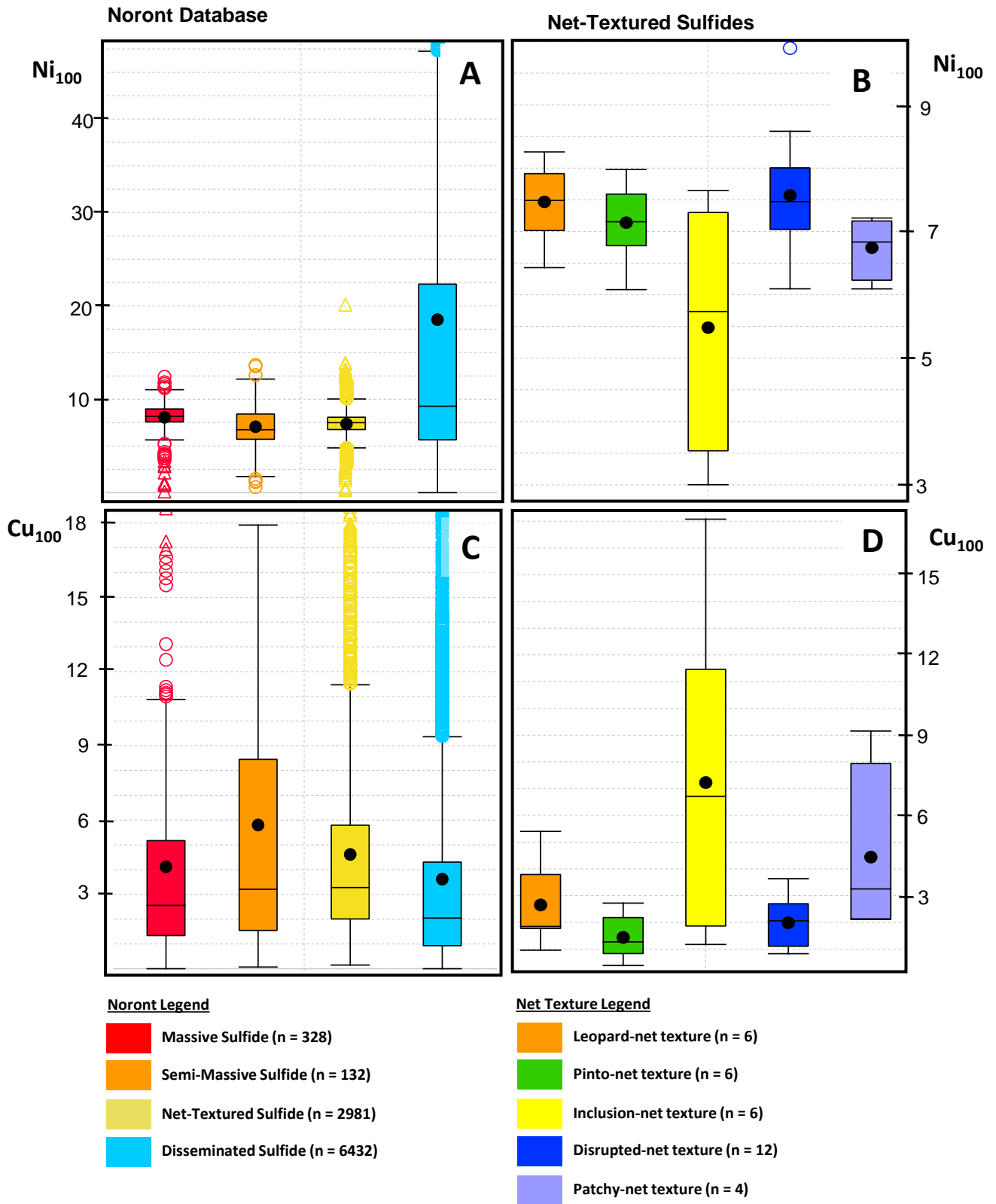


Figure 34.

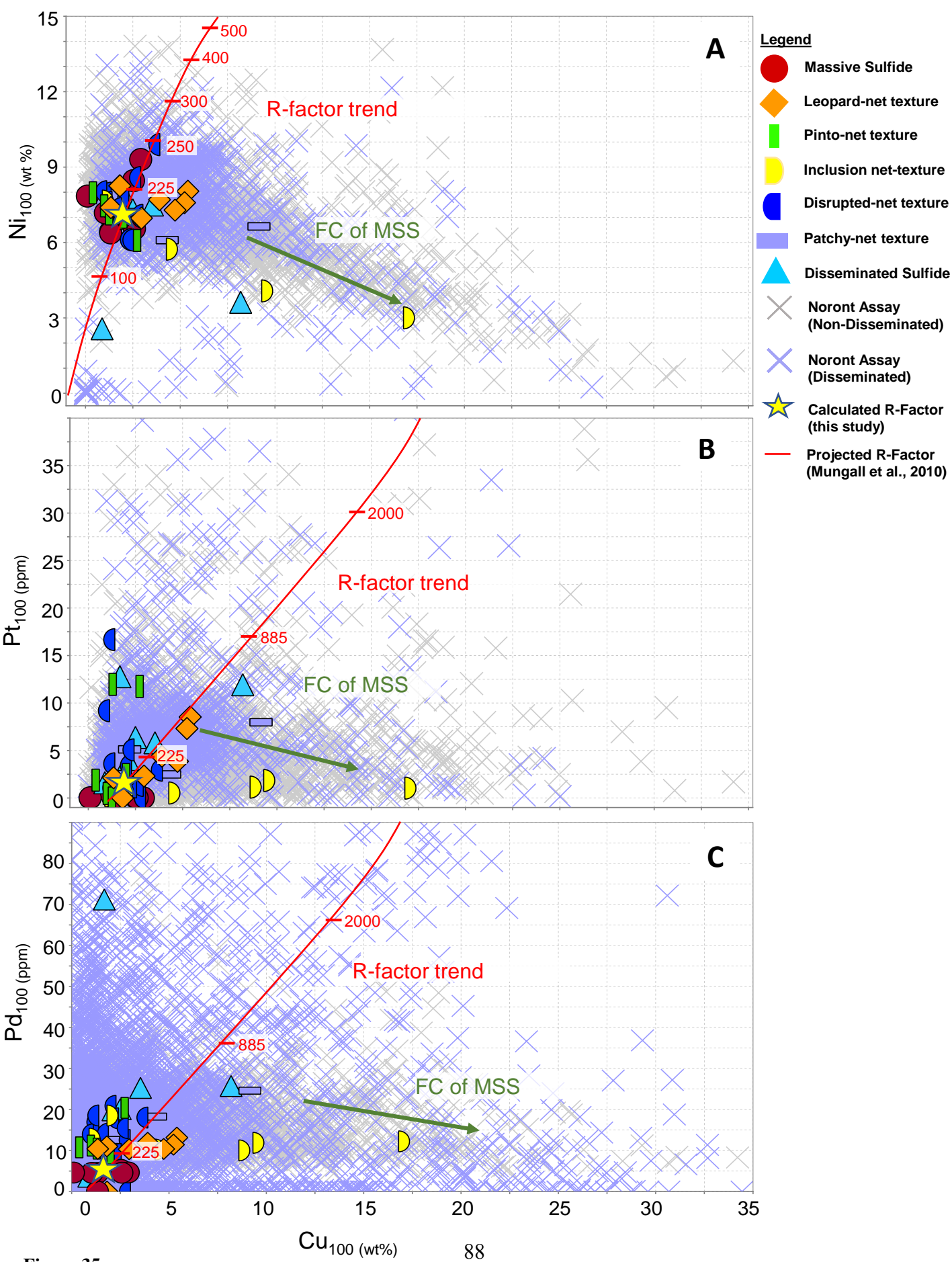


Figure 35.

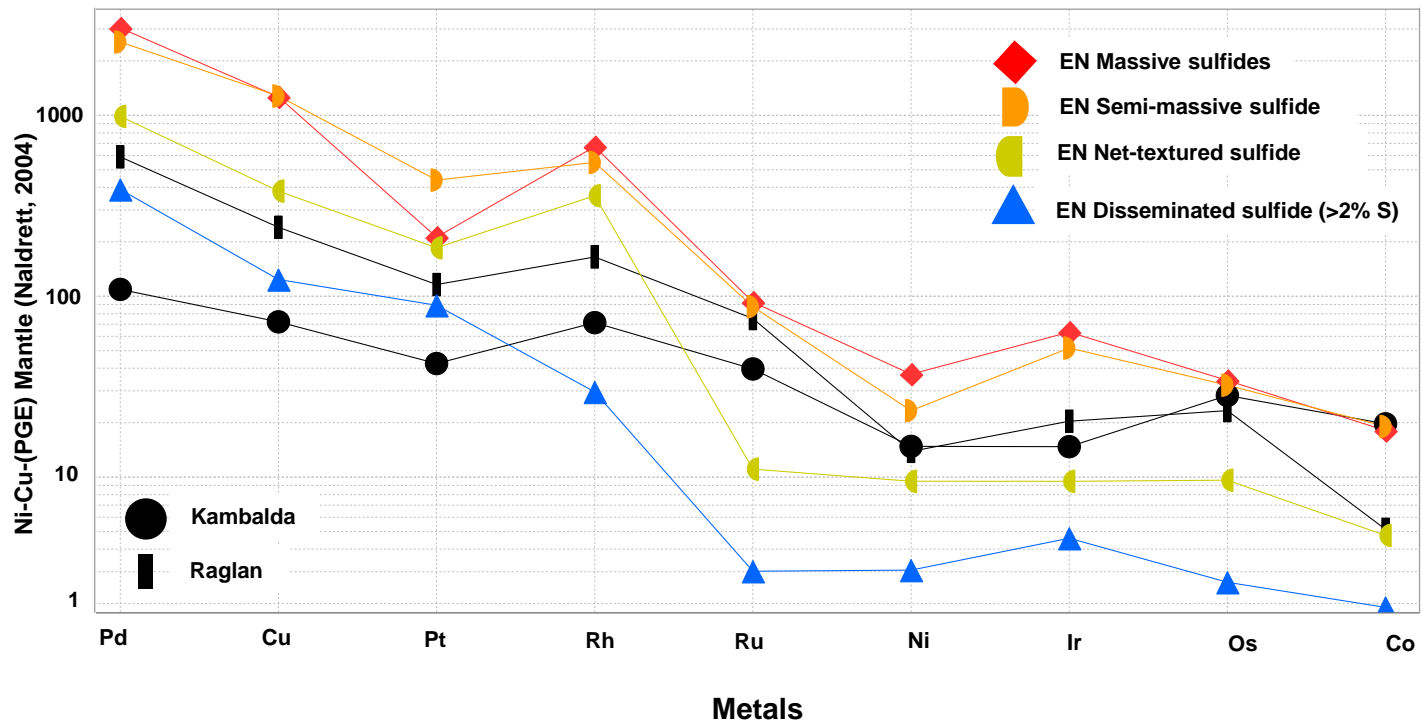


Figure 36.

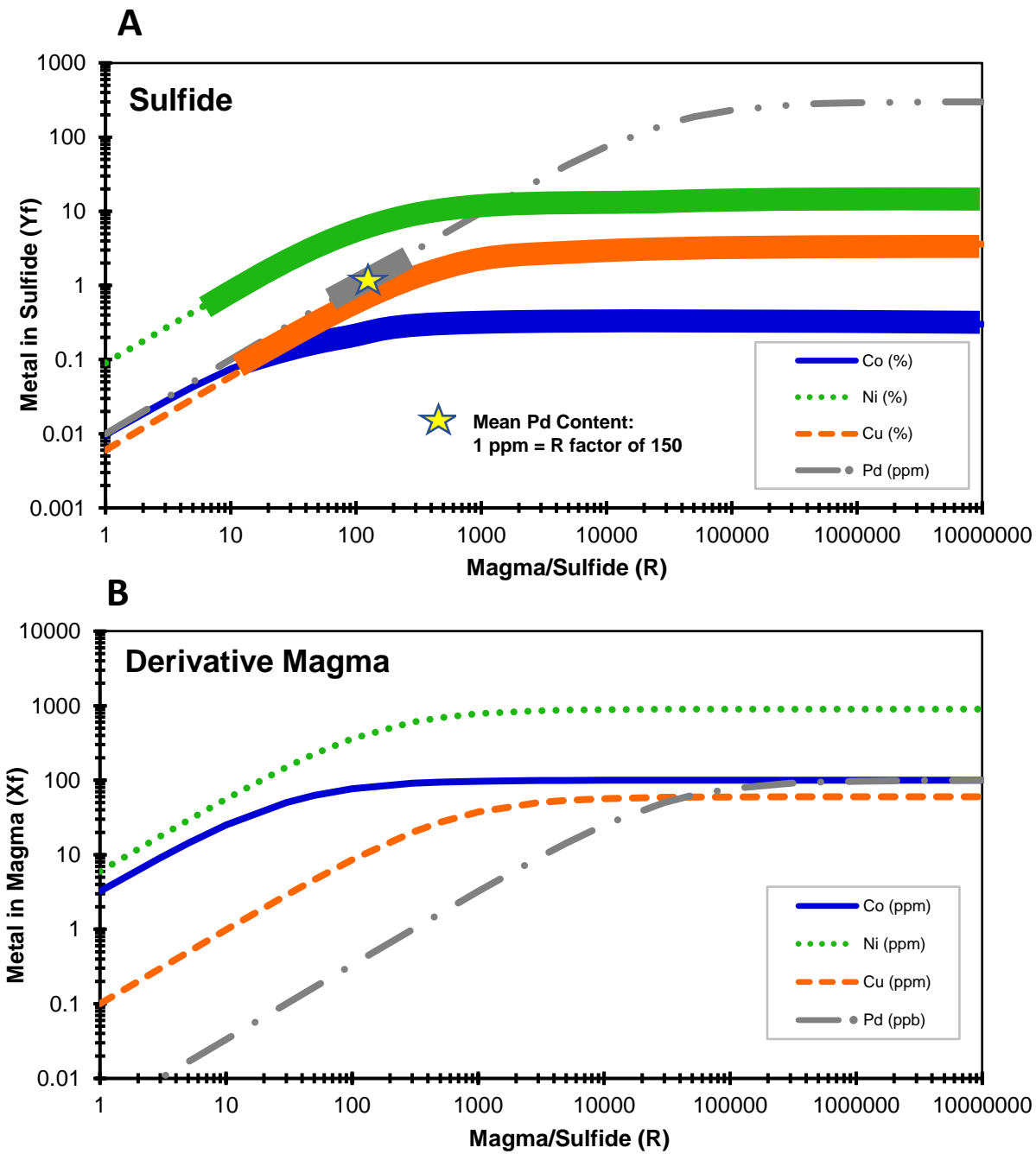


Figure 37.

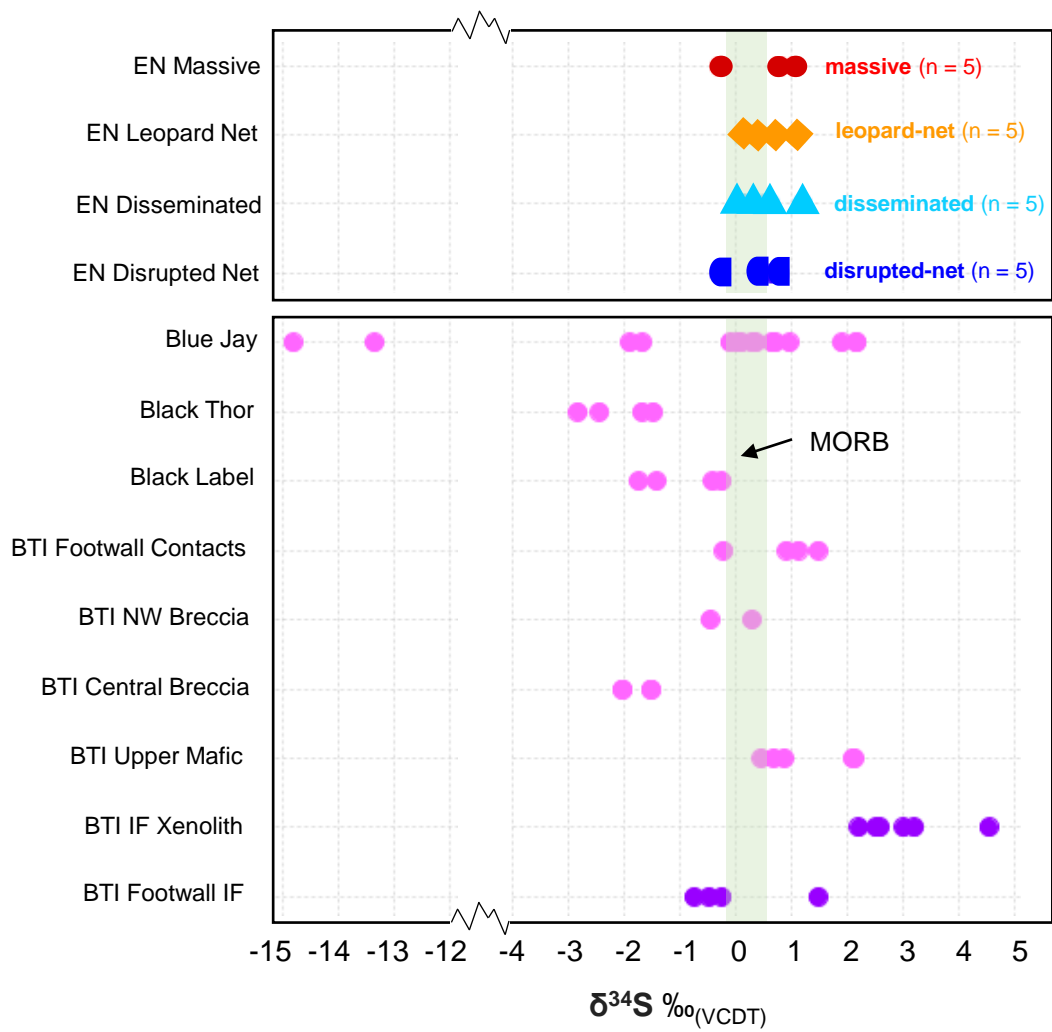


Figure 38.

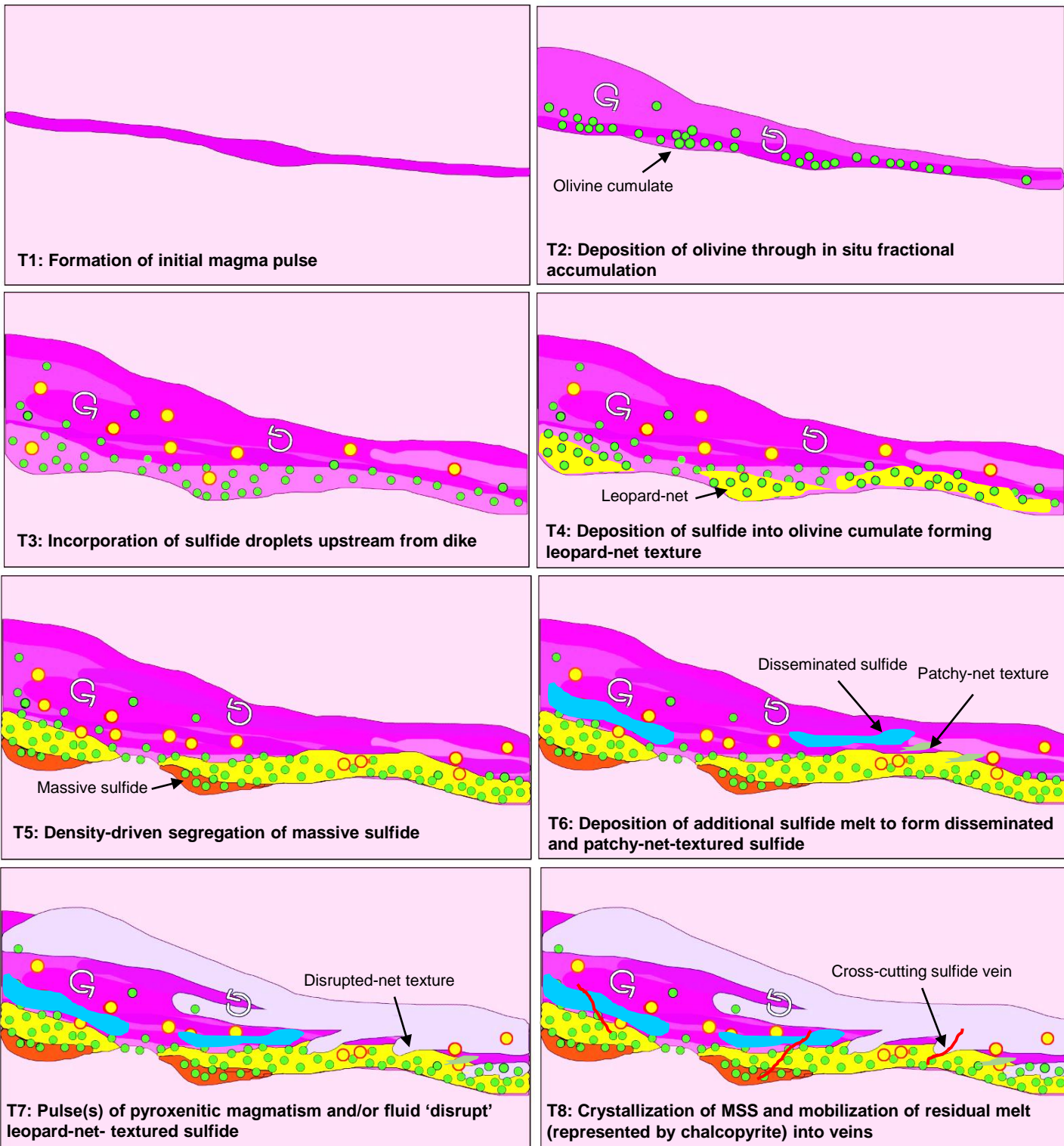
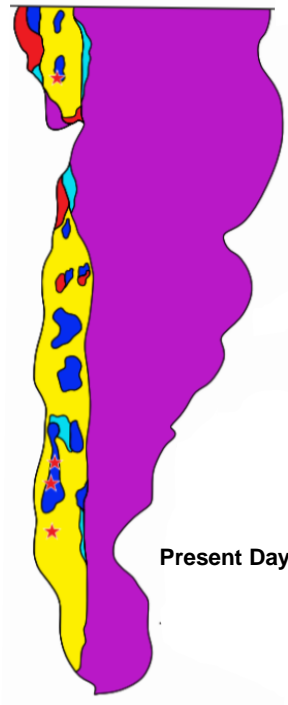
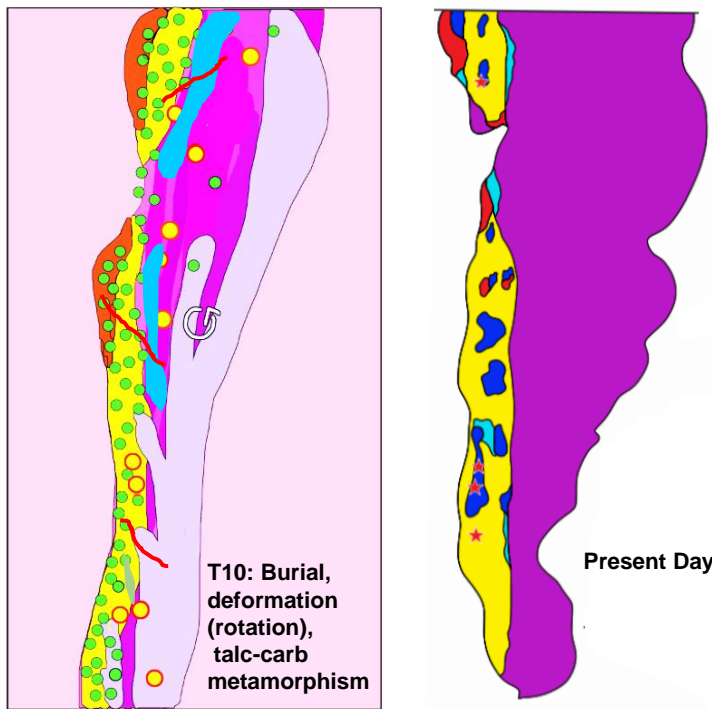
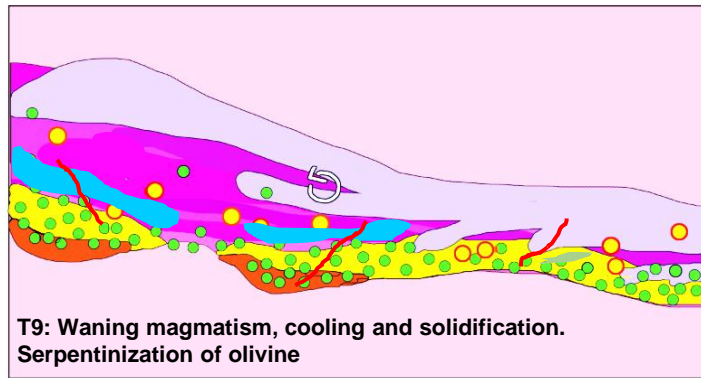


Figure 39.



250 m



15 Tables

Table 1. Sulfide textures in the Eagle's Nest deposit

Sulfide Textural Facies	Key Features	Nominal Sulfide Content (wt%)	Nominal Sulfur Content* (%)	Eagle's Nest Deposit			
				Sulfide Content (wt %)	Proportion of Mineralization (wt%)	Thickness (m)	Strike Length (m)
Disseminated*		<15	<5.9	<15	14	4-18	20-100
Light**	Fine-grained, wispy isolated sulfide	<5	<2.0	0.5-5	14		
Medium**	Fine-medium grained wispy sulfide	5-10	2.0-3.9	5-10	42		
Heavy**	Medium-coarse grained clustered sulfide	10-15	4.0-5.9	10-15	21		
Patchy**	Fine-medium grained sulfide with 1-10 cm zones of barren rock in between	<15	<5.9	8-10	9		
Blebbly**	Isolated individual round sulfide 'blebs' in otherwise barren host rock	<15	<5.9	2-5	14		
Net-Textured*		15-60	5.9-23.4	15-35	52	5-15	50-105
Leopard**	Bimodal cumulus olivine with continuous interstitial sulfide			15-35	52		
Disrupted**	Isolated patches of olivine-sulfide cumulate with cross cutting barren pyroxenite			18-25	28		
Patchy**	Isolate patches of olivine-sulfide cumulate in peridotite			15-25	14		
Pinto**	Weakly continuous olivine-sulfide cumulate with euhedral barren Opx oikocrysts			15-30	5		
Inclusion**	Clasts of barren peridotite			15-30	1		
Semi-Massive*	Massive sulfide w/fragments of silicate material	50-80	23.5-31.2	50-80	7	2-12	10-28
Massive*	Over 80% sulfide	>80	>31.2	>80	27		
*assuming 39% S in 100% sulfide for other deposits, **based on 200 representative samples in this study							

Table 2: Representative EMPA Data

Sample Label	Mineral	S (%)	Fe (%)	Co (%)	Ni (%)	Cu (%)	As (%)	Ag (%)	Total
Lower Limit of Detection (Pentlandite)		0.03	0.02	0.01	0.03	0.02	0.02	0.03	
Lower Limit of Detection (Chalcopyrite and Pyrrhotite)		0.03	0.02	0.01	0.01	0.03	0.02	0.03	
C107po_1	Pyrrhotite	38.7	60.9	0.01	0.12	0.01	0.01	0.01	99.7
C107poVn_2	Pyrrhotite	39.0	61.0	0.01	0.09	0.02	0.00	0.02	100.1
C107po_3	Pyrrhotite	38.5	61.3	0.00	0.14	0.00	0.00	0.02	100.0
C93po_4	Pyrrhotite	38.5	61.3	0.01	0.17	0.00	0.01	0.01	99.9
C59po_1	Pyrrhotite	39.3	60.2	0.00	0.64	0.00	0.01	0.03	100.1
C59po_2	Pyrrhotite	39.2	60.0	0.01	0.69	0.00	0.02	0.02	99.9
C59po_3	Pyrrhotite	39.2	60.3	0.01	0.60	0.00	0.02	0.00	100.2
AH40po_5	Pyrrhotite	36.4	63.2	0.01	0.01	0.02	0.00	0.00	99.6
C103po_1mass	Pyrrhotite	40.4	59.9	0.00	0.54	0.00	0.00	0.02	100.9
C103po_2mass	Pyrrhotite	39.9	59.6	0.01	0.90	0.00	0.00	0.02	100.5
C103po_3net	Pyrrhotite	40.1	59.8	0.01	0.70	0.04	0.00	0.03	100.6
C103po_5net	Pyrrhotite	39.9	59.6	0.01	0.79	0.00	0.01	0.03	100.4
C93ccp_1	Chalcopyrite	35.3	30.4	0.00	0.01	35.2	0.00	0.01	100.9
C93ccp_2	Chalcopyrite	34.9	30.3	0.01	0.00	34.9	0.01	0.01	100.1
C93ccp_3	Chalcopyrite	35.0	30.5	0.01	0.00	34.9	0.01	0.02	100.4
C59ccp_1	Chalcopyrite	35.1	30.4	0.00	0.02	34.4	0.01	0.00	99.9
C59ccp_2	Chalcopyrite	35.1	30.2	0.01	0.00	34.6	0.00	0.04	100.0
C59ccp_3	Chalcopyrite	35.2	30.2	0.00	0.00	34.9	0.01	0.02	100.2
C4ccp_4	Chalcopyrite	35.0	30.6	0.00	0.00	34.5	0.00	0.02	100.2
C103ccp_1mass	Chalcopyrite	35.2	30.3	0.00	0.01	34.0	0.00	0.02	99.5
C107pn_3	Pentlandite	33.6	33.2	1.08	32.2	0.00	0.00	0.01	100.1
C101pn_1	Pentlandite	33.3	29.1	0.90	37.1	0.00	0.00	0.00	100.4
C101pnINC_1	Pentlandite	33.8	28.8	0.94	36.1	0.00	0.00	0.03	99.7
C101pn_2	Pentlandite	33.6	28.7	0.82	37.3	0.00	0.01	0.01	100.4
C101pn_3	Pentlandite	33.7	28.4	0.63	37.9	0.00	0.02	0.01	100.6
C56pn_2	Pentlandite	33.2	30.7	1.10	35.4	0.00	0.00	0.02	100.4
C94pn_2	Pentlandite	33.1	29.3	1.06	36.7	0.00	0.02	0.00	100.1
C94pn_4	Pentlandite	33.2	28.9	1.01	36.8	0.00	0.00	0.01	99.9
13pn_1	Pentlandite	33.3	28.8	0.67	37.8	0.00	0.02	0.01	100.6
13pn_2	Pentlandite	33.5	28.9	0.74	37.4	0.00	0.00	0.01	100.5
13pn_3	Pentlandite	33.4	28.7	0.58	37.8	0.00	0.02	0.02	100.6
13pn_4	Pentlandite	33.4	28.7	0.83	37.4	0.00	0.01	0.02	100.4
C103pn_1mass	Pentlandite	34.6	27.7	0.28	37.1	0.00	0.02	0.02	99.7
C103pn_2mass	Pentlandite	33.6	28.6	0.39	37.8	0.00	0.01	0.02	100.4
C103pn_4net	Pentlandite	33.9	28.7	0.65	37.6	0.00	0.01	0.03	100.9
C103pn_5net	Pentlandite	34.2	28.5	0.31	37.5	0.02	0.02	0.00	100.6

Table 3: Representative Whole-Rock XRF Data (Mineralized Rocks)

Element Unit		S wt%	Al2O3 wt%	BaO wt%	CaO wt%	Cr2O3 wt%	Fe2O3 wt%	K2O wt%	MgO wt%	MnO wt%	Na2O wt%	P2O5 wt%	SiO2 wt%	TiO2 wt%	V2O5 wt%	105 LOI wt%	LOI wt%	Sum wt%
Lower Limit of Detection		0.03	0.04	0.008	0.015	0.004	0.02	0.02	0.01	0.004	0.04	0.004	0.08	0.02	0.005	0.05	0.05	
Upper Reporting Limit	Litho		100	1	100	5	100	20	50	5	15	40	100	8	2	100	100	
NOT-09-053/847.71	disseminated	1.11	6.64	<0.008	4.00	0.59	12.2	0.04	25.8	0.10	0.33	0.03	42.8	0.31	0.02	0.14	5.80	98.6
NOT-09-053/857.26 FG	disseminated	3.23	5.11	<0.008	6.30	0.52	12.0	0.05	25.3	0.15	0.23	0.02	44.1	0.21	0.01	0.08	5.60	99.5
NOT-09-068-W1/861.65	disseminated	0.13	8.03	<0.008	6.00	0.44	10.8	0.66	22.8	0.24	0.45	0.04	45.9	0.37	0.02	0.15	4.30	99.9
NOT-09-068-W1/871	disseminated	0.28	8.68	0.03	5.80	0.31	10.6	2.75	20.7	0.17	0.63	0.05	46.7	0.41	0.03	0.16	2.60	99.5
NOT-10-077/289.52	disseminated	0.40	8.10	<0.008	7.20	0.35	11.2	0.08	21.7	0.23	0.39	0.04	44.6	0.40	0.03	0.17	4.80	99.1
NOT-10-092/702	disseminated	0.04	10.99	0.02	7.90	0.22	10.7	0.74	14.2	0.17	2.33	0.05	49.8	0.52	0.03	0.18	2.50	100.1
NOT-10-092/709.36	disseminated	0.26	8.61	0.04	5.40	0.35	10.2	4.18	21.2	0.15	0.37	0.05	46.6	0.38	0.03	0.17	2.40	99.9
NOT-07-017/173.4	massive	33.9	<0.04	<0.008	<0.015	<0.004	74.1	0.03	0.06	0.01	1.11	<0.004	0.42	0.08	0.00	<0.05	13.0	88.8
NOT-07-028/217.65	massive	38.3	<0.04	<0.008	<0.015	<0.004	71.2	0.04	0.12	0.01	1.42	<0.004	0.33	0.08	0.00	<0.05	13.2	86.4
NOT-09-059/512	massive	40.0	<0.04	<0.008	0.09	0.06	76.1	0.05	0.06	0.01	0.98	<0.004	0.64	0.10	0.00	0.08	13.0	91.2
NOT-09-064/1105	massive	39.1	0.05	<0.008	<0.015	0.03	77.4	0.04	0.27	0.01	1.25	<0.004	0.37	0.12	0.00	<0.05	11.7	91.2
NOT-10-076-W1/533.7	massive	39.3	<0.04	<0.008	<0.015	0.05	75.3	0.04	0.02	0.01	0.96	<0.004	<0.08	0.10	0.00	<0.05	13.3	89.7
NOT-07-028/72.33	disrupted-net	6.60	2.73	<0.008	2.10	0.61	21.7	0.04	26.5	0.13	0.41	0.02	34.1	0.16	0.01	0.44	8.70	97.4
NOT-09-053/857.26 A	disrupted-net	7.61	2.86	<0.008	2.20	0.68	23.8	<0.02	25.7	0.15	0.32	0.02	33.5	0.16	0.01	0.24	8.00	97.4
NOT-09-053/857.26 K	disrupted-net	9.22	1.83	<0.008	0.80	0.78	28.9	0.03	24.8	0.14	0.23	0.02	28.9	0.19	0.02	0.31	9.40	96.0
NOT-09-053/861.65	disrupted-net	6.66	3.20	<0.008	2.03	0.63	20.5	0.03	27.8	0.16	0.28	0.02	33.8	0.09	0.01	0.27	9.10	97.6
NOT-09-053/872.36	disrupted-net	6.04	2.89	<0.008	1.64	0.91	20.1	0.09	28.3	0.13	0.38	0.02	32.9	0.13	0.01	0.34	9.80	97.4
NOT-09-053-W6/782.6	disrupted-net	9.84	1.29	<0.008	0.83	0.61	29.6	0.05	25.2	0.12	0.37	0.01	27.5	0.14	0.01	0.35	10.3	96.0
NOT-09-056/540.43	disrupted-net	9.80	1.99	<0.008	0.92	0.61	30.3	0.04	24.6	0.15	0.32	0.02	27.7	0.12	0.01	0.40	10.5	97.3
NOT-10-085-W2/1345.9	disrupted-net	9.98	2.04	<0.008	0.55	0.43	25.2	0.04	27.3	0.10	0.40	0.02	29.2	0.12	0.01	0.41	11.2	96.6
NOT10-085-W2/1349.12	disrupted-net	8.85	1.57	<0.008	0.31	0.60	28.4	0.06	26.7	0.11	0.27	0.01	27.6	0.16	0.01	0.37	10.9	96.7
NOT-07-028/206.75	inclusion-net	3.99	4.10	<0.008	2.69	0.56	17.7	0.19	27.5	0.22	0.44	0.02	35.9	0.17	0.01	0.56	8.50	98.0
NOT-07-028/208.37	inclusion-net	10.1	2.12	<0.008	1.23	0.51	27.4	0.06	25.1	0.21	0.32	0.01	28.8	0.07	0.01	0.50	10.7	96.5
NOT-07-028/208.97	inclusion-net	5.94	3.21	<0.008	2.09	0.73	19.2	0.11	27.8	0.26	0.43	0.02	33.9	0.11	0.01	0.44	9.20	97.0
NOT-09-056/535.4	inclusion-net	10.4	1.45	<0.008	0.61	0.57	27.7	0.04	25.6	0.18	<0.04	0.01	27.7	0.12	0.01	0.38	11.1	95.1
NOT-09-064/1120.1	inclusion-net	10.5	1.51	<0.008	0.73	0.66	29.7	0.03	24.3	0.14	0.31	0.01	26.5	0.16	0.01	0.35	10.5	94.6
NOT-09-064/1121.13	inclusion-net	7.96	2.69	<0.008	1.45	0.40	24.9	0.03	26.5	0.15	0.25	0.01	30.9	0.12	0.01	0.27	10.1	97.4
NOT-07-017/142.5	leopard-net	11.5	0.82	<0.008	0.06	0.44	31.8	0.03	23.9	0.10	0.31	0.01	24.1	0.12	0.01	0.50	11.3	92.9
NOT-07-017/143.68	leopard-net	11.4	0.86	<0.008	0.06	0.53	32.6	0.03	24.2	0.12	0.34	0.00	24.3	0.13	0.01	0.50	11.2	94.4
NOT-07-017/148.5	leopard-net	11.5	0.85	<0.008	0.05	0.68	34.0	0.03	23.2	0.13	0.28	0.01	23.3	0.15	0.01	0.50	11.0	93.6
NOT-07-029/48.3	leopard-net	9.84	1.47	<0.008	0.12	0.34	28.3	0.04	25.9	0.12	0.31	<0.004	26.4	0.09	0.01	0.42	11.5	94.6
NOT-07-029/61.85	leopard-net	10.2	1.42	<0.008	0.09	0.31	28.5	0.08	25.3	0.12	0.25	0.00	25.8	0.10	0.01	0.45	11.6	93.4
NOT-09-071/739.57	leopard-net	12.5	1.10	<0.008	0.02	1.38	31.8	0.03	23.5	0.14	0.28	<0.004	23.7	0.14	0.02	0.49	11.7	93.8
NOT-09-053/884.25	pinto-net	3.67	3.72	<0.008	1.93	0.82	16.6	0.17	30.9	0.13	0.28	0.02	36.7	0.16	0.02	0.37	7.00	98.4
NOT-09-071/719.65	pinto-net	6.28	2.77	<0.008	1.91	0.97	22.2	0.04	28.4	0.20	0.37	0.01	33.8	0.15	0.01	0.28	7.20	98.0
NOT-09-071/720.78	pinto-net	11.1	1.27	<0.008	0.79	0.82	31.7	0.05	24.9	0.16	0.37	<0.004	26.6	0.12	0.01	0.36	10.4	97.1
NOT-10-076-W1/556.11	pinto-net	8.51	2.34	<0.008	1.39	0.55	26.5	0.07	25.6	0.16	0.35	0.02	33.1	0.14	0.01	0.32	8.20	98.4
NOT-10-076-W1/557.11	pinto-net	10.1	1.33	<0.008	1.08	0.54	28.3	0.07	24.6	0.14	0.35	0.01	31.3	0.16	0.01	0.34	8.30	96.2
NOT-08-030/47.4	patchy-net	2.86	2.94	0.01	1.64	0.41	16.4	0.26	30.0	0.12	0.39	0.03	37.0	0.22	0.01	0.92	8.30	97.7
NOT-09-053-W6/750	patchy-net	9.85	1.88	<0.008	1.13	0.30	25.6	0.03	27.1	0.14	0.22	0.01	28.7	0.06	<0.005	0.39	10.5	95.8
NOT-09-056/560	patchy-net	5.92	2.81	<0.008	1.73	0.40	20.5	0.03	28.9	0.15	0.12	0.01	31.7	0.12	0.01	0.43	10.5	97.0
NOT-09-056/566	patchy-net	6.76	2.68	<0.008	1.68	0.26	21.3	0.02	28.5	0.12	0.15	0.01	30.9	0.08	0.01	0.52	11.0	96.7

Table 4: Representative Whole-Rock ICP-MS Data (Minor Elements and PGEs) Mineralized

Sample		Pt	Pd	Au	Ag	As	Bi	Cd	Mo	Sb	Te	Tl	Se	Sn
Unit		ppm	ppm	ppm	ppm	ppm	ppm	ppm	ppm	ppm	ppm	ppm	ppm	ppm
Lower Limit of Detection	LITH	0.01	0.02	0.00	0.20	0.10	0.02	0.02	0.06	0.01	0.02	0.001	0.20	0.10
NOT-10-GT04/582.3	disseminated	0.02	0.10	0.01	0.20	9.50	0.14	0.02	0.62	0.25	0.03	0.00	0.20	0.10
NOT-10-GT04/605	disseminated	0.03	0.09	0.01	0.20	21.70	0.06	0.02	0.41	0.36	0.02	0.00	0.20	0.10
NOT-09-068-W1/861.65	disseminated	0.02	0.05	0.00	0.20	0.80	0.05	0.03	0.46	0.04	0.09	0.25	0.30	0.10
NOT-10-GT04/386.2	disseminated	0.02	0.04	0.01	0.20	0.30	0.12	0.02	0.68	0.04	0.11	0.45	0.20	0.20
NOT-10-GT04/342.3	disseminated	0.04	0.15	0.00	0.20	0.80	0.27	0.05	0.34	0.05	0.15	0.04	0.70	0.10
NOT-10-092/709.36	disseminated	0.04	0.17	0.01	0.20	0.70	0.11	0.03	0.70	0.09	0.18	1.21	1.00	0.20
NOT-09-068-W1/871	disseminated	0.05	0.15	0.01	0.20	0.40	0.08	0.03	10.02	0.08	0.14	0.88	0.80	0.20
NOT-10-GT04/419.9	disseminated	0.01	0.03	0.00	0.20	0.40	0.07	0.02	0.32	0.06	0.12	0.04	0.20	0.20
NOT-10-077/289.52	disseminated	0.14	0.79	0.01	0.20	0.80	0.66	0.08	1.71	0.45	0.86	0.28	1.90	0.10
NOT-09-053/847.71	disseminated	0.35	0.76	0.15	0.84	1.40	0.67	0.38	0.48	0.24	1.18	0.04	4.00	0.20
NOT-09-053/857.26	disseminated	0.34	1.70	0.01	1.62	1.40	0.82	0.19	0.69	0.04	1.30	0.04	6.70	0.10
NOT-09-057/584.02	massive	0.79	3.89	0.06	2.86	3.10	2.30	0.33	0.63	0.09	3.33	0.11	22.80	0.40
NOT-07-017/173.4	massive	0.01	4.80	0.21	6.49	2.20	6.15	1.37	0.91	0.02	10.45	4.10	86.60	1.30
NOT-07-028/217.65	massive	0.01	4.80	0.05	8.60	7.00	3.47	3.56	1.26	0.03	8.95	1.26	82.20	2.70
NOT-09-064/1105	massive	0.02	4.80	0.03	5.19	48.40	5.46	0.04	0.99	0.04	7.91	0.16	59.60	0.10
NOT-10-076-W1/533.7	massive	0.01	4.80	0.28	5.21	0.30	1.31	0.84	0.84	0.01	3.02	0.17	52.70	0.70
NOT-09-059/513.9	massive	0.81	4.80	0.02	4.93	5.40	6.33	1.68	1.45	0.32	3.80	3.35	54.90	0.40
NOT-09-059/512	massive	0.05	4.80	0.07	5.17	7.70	6.59	0.73	1.34	0.28	3.57	3.94	54.40	0.20
NOT-09-053/872.36	disrupted-net	0.21	2.51	0.04	1.90	1.10	0.75	0.62	0.38	0.03	1.60	0.05	7.10	0.30
NOT-07-023/72.33	disrupted-net	0.60	3.68	0.06	1.30	1.70	2.17	0.56	0.52	0.09	3.91	0.18	12.40	0.50
NOT-09-053/861.65	disrupted-net	0.13	2.23	0.14	1.73	1.30	1.08	0.75	0.46	0.04	1.33	0.02	9.00	0.30
NOT-10-GT03A/642.65	disrupted-net	0.24	2.79	0.03	1.80	0.50	1.46	0.44	0.38	0.07	2.64	0.05	14.20	0.80
NOT-09-053/857.26 A	disrupted-net	0.21	3.43	0.02	1.50	2.10	1.40	0.13	1.01	0.08	2.27	0.05	11.30	0.20
NOT-10-085-W2/1349.12	disrupted-net	3.91	4.35	0.06	3.86	1.90	2.78	0.39	0.53	0.07	4.74	0.12	22.90	0.70
NOT-09-053/857.26 K	disrupted-net	1.24	4.36	0.22	2.77	1.90	1.75	1.07	1.30	0.09	3.11	0.04	15.80	0.50
NOT-09-056/540.43	disrupted-net	0.94	3.84	0.04	1.80	1.30	1.63	0.50	0.44	0.08	3.44	1.43	20.40	0.40
NOT-09-053-W6/782.6	disrupted-net	0.78	4.80	0.13	3.75	2.10	1.98	1.46	0.45	0.10	4.68	0.09	17.80	0.80
NOT-10-085-W2/1345.9	disrupted-net	2.44	3.70	0.06	3.28	1.70	1.86	0.36	0.42	0.06	3.20	0.10	16.50	0.70
NOT-10-GT03A/650.62	disrupted-net	0.39	3.05	2.13	7.46	0.70	1.47	0.82	0.56	0.06	3.31	0.04	20.10	0.30
NOT-07-028/206.75	inclusion-net	0.12	1.08	0.13	2.90	0.20	0.68	1.45	0.66	0.03	0.94	0.66	6.80	0.60
NOT-07-028/208.97	inclusion-net	0.29	1.90	0.17	5.29	0.20	0.99	5.36	0.48	0.05	2.04	1.06	12.10	1.20
NOT-09-064/1121.13	inclusion-net	0.15	3.92	0.08	2.42	0.70	2.41	0.62	0.52	0.09	4.51	0.23	18.50	1.70
NOT-07-028/208.37	inclusion-net	0.14	2.75	0.24	5.07	0.20	1.69	5.73	0.45	0.05	2.97	1.17	18.50	1.20
NOT-09-056/535.4	inclusion-net	0.29	3.47	0.06	10.27	0.80	1.57	9.00	0.47	0.09	4.77	1.90	20.30	4.50
NOT-09-064/1120.1	inclusion-net	0.06	3.59	0.04	2.77	0.30	2.75	0.49	0.65	0.05	3.63	0.16	21.00	0.70
NOT-07-029/48.3	leopard-net	0.40	2.89	0.04	1.59	0.20	1.03	0.44	0.54	0.02	2.48	0.31	18.60	0.70
NOT-07-029/61.85	leopard-net	1.06	2.85	0.10	3.01	0.40	1.41	1.00	0.42	0.03	2.77	0.36	19.50	1.00
NOT-07-017/143.68	leopard-net	1.35	3.65	0.10	5.46	0.50	2.82	2.27	1.19	0.04	5.81	0.35	31.30	1.70
NOT-07-017/142.5	leopard-net	2.64	4.08	1.36	7.48	0.40	4.24	4.52	0.77	0.03	10.57	0.32	36.20	1.50
NOT-07-017/148.5	leopard-net	2.27	3.55	0.11	6.16	0.90	2.58	6.00	1.08	0.05	5.88	0.47	35.20	1.60
NOT-09-071/739.57	leopard-net	0.77	3.43	0.03	3.92	3.10	2.29	0.71	0.60	0.07	3.27	0.05	21.10	0.70
NOT-09-053/884.25	pinto-net	1.14	1.98	0.09	2.17	0.60	0.96	0.55	0.90	0.05	1.88	0.12	8.10	0.30
NOT-09-071/719.65	pinto-net	0.31	1.80	0.01	0.57	3.00	0.76	0.04	0.36	0.08	1.74	0.02	9.50	0.30
NOT-10-076-W1/556.11	pinto-net	2.70	2.36	0.11	0.63	1.50	0.69	0.27	0.47	0.04	2.19	0.20	13.50	0.30
NOT-10-076-W1/557.11	pinto-net	0.66	2.49	0.02	0.84	1.50	0.65	0.24	0.65	0.04	2.34	0.02	12.90	0.30
NOT-09-071/720.78	pinto-net	0.14	3.31	0.02	1.95	3.10	1.56	0.30	0.59	0.10	3.48	0.05	15.90	0.30
NOT-08-030/47.4	patchy-net	0.62	1.91	0.16	3.16	0.50	1.08	1.17	0.75	0.04	2.17	0.18	7.10	0.60
NOT-09-056/560	patchy-net	0.81	1.91	0.06	1.37	2.80	1.20	0.28	0.37	0.10	2.26	0.21	12.80	1.20
NOT-09-056/566	patchy-net	0.45	2.26	0.05	1.47	1.70	1.49	0.43	0.40	0.10	2.50	0.29	15.80	1.20
NOT-09-053-W6/750	patchy-net	0.65	4.80	0.07	5.05	1.20	2.44	1.64	0.38	0.04	6.26	0.04	21.70	1.60
NOT-09-049/316	patchy-net	0.71	3.18	0.07	1.44	3.60	2.61	0.29	0.97	0.17	3.22	1.46	17.60	0.40

Table 5: Sulfur Isotope Data

Sample ID	$\delta^{34}\text{S}_{\text{VCDT}}$	Sulfide Texture
NOT-07-017-138.09	1.1	Leopard Net
NOT-07-029-63	0.7	Leopard Net
NOT-07-029-68.33	0.8	Massive
NOT-07-029-72	0.4	Disrupted Net
NOT-07-18-210	0.0	Semi-Massive
NOT-08-030-974	0.5	Disrupted Net
NOT-08-044-304.25	1.1	Massive
NOT-08-30-104.11	1.2	Disseminated
NOT-09-053-857.28	-0.3	Disrupted Net
NOT-09-053-863.19	0.7	Leopard Net
NOT-09-053-W3/827.74	0.4	Disseminated
NOT-09-053-W5-1014	0.5	Semi-Massive
NOT-09-056-592	0.8	Semi-Massive
NOT-09-057-584.82	0.4	Leopard Net
NOT-09-059-508.12	0.8	Massive
NOT-09-062-608.13	0.6	Disseminated
NOT-09-064-1115.7	-0.3	Massive
NOT-09-068-W1/765.6	0.8	Semi-Massive
NOT-09-071-737.14	0.1	Leopard Net
NOT-10-056-540.85	0.8	Disrupted Net
NOT-10-076-W1/552	0.1	Disseminated
NOT-10-085-W2/1352	0.5	Disseminated
NOT-10-085-W2/1345.9	0.7	Disrupted Net
NOT-10-087-608.86	1.1	Massive

16 Appendices

Electronic Appendix A: Electron probe microanalyses of olivine, pentlandite, chalcopyrite, and pyrrhotite)

Electronic Appendix B: Whole-rock geochemical data

Electronic Appendix C: Drill core logs (this study)